CNWRA *A center of excellence in earth sciences and engineering*

A Division of Southwest Research Institute®
6220 Culebra Road • San Antonio, Texas, U.S.A. 78228-5166
(210) 522-5160 • Fax (210) 522-5155

March 12, 2004
Contract No. NRC-02-02-012
Account No. 20.06002.01.051

U.S. Nuclear Regulatory Commission
ATTN: Dr. John S. Trapp
Office of Nuclear Material Safety and Safeguards
Two White Flint North, Mail Stop 7 D13
Washington, DC 20555-0001

Subject: **Final Revised Intermediate Milestone—Examination of Effects of Geologic Features on Thermally Induced Stress at Yucca Mountain, Nevada (IM 06002.01.051.470)**

Dear Dr. Trapp:

Enclosed is the final revised version of Intermediate Milestone 06002.01.051.470 entitled "Examination of Effects of Geologic Features on Thermally Induced Stress at Yucca Mountain, Nevada," which incorporates your email comments and corrections. This report reassesses the alteration of the *in-situ* stresses at the potential high-level waste repository at Yucca Mountain due to the thermal effects of waste emplacement. In addition, aspects of geology that have not been fully explored in previous DOE work are discussed and the potential effects of these aspects are assessed using simple first-order calculations. The report concludes that the thermally induced stresses would be much smaller than suggested by DOE analyses, and there is a reduced potential for wide-spread reorientation of principal stresses. As such, igneous dike propagation is unlikely to be affected by thermally induced, repository scale stress state modifications.

If you have any further questions about this deliverable please contact Dr. Kevin Smart at (210) 522-5859 or me at (210) 522-5183.

Sincerely,

H. Lawrence McKague
Element Manager

/slo
Enclosures
cc: B. Meehan, W. Reamer, J. Schlueter, J. Greeves, A. Campbell, K. Stablein, L. Campbell, L. Kokajko, M. Leach, D. DeMarco, E. Whitt, B. Leslie, P. Justus, J. Rubenstone, M. Nataraja, W. Patrick, CNWRA Dirs/EMs (letter only), K. Smart, L. Gutierrez, Record Copy B, IQS

Washington Office • Twinbrook Metro Plaza #210
12300 Twinbrook Parkway • Rockville, Maryland 20852-1606

EXAMINATION OF EFFECTS OF GEOLOGIC FEATURES ON THERMALLY INDUCED STRESS AT YUCCA MOUNTAIN, NEVADA

Prepared for

U.S. Nuclear Regulatory Commission
Contract NRC–02–02–012

Prepared by

Kevin J. Smart

Center for Nuclear Waste Regulatory Analyses
San Antonio, Texas

February 2004

ABSTRACT

Previous U.S. Department of Energy (DOE)-sponsored research suggests significant and widespread alteration of the *in-situ* stress state at Yucca Mountain will occur from heating because of high-level waste emplacement. The potential stress-state alteration, which would take place over a significant region (tens of square kilometers), reflects significant increase in horizontal stress components that causes the vertical stress to switch from the maximum to the minimum principal stress. DOE subsequently used the high horizontal-to-vertical stress ratio to argue that an igneous dike propagating toward the repository from a deeper crustal level will be converted into a sub-horizontal sill as it encounters the altered stress state surrounding the potential repository. The dike-to-sill conversion is postulated by DOE to take place several hundred meters below the repository because the stress alteration effects are widespread. If correct, this mechanism could protect the potential repository against igneous intrusion, because dikes would be deflected into sills.

This report summarizes the assumptions and results of previous DOE thermal stress studies. In addition, aspects of geology that have not been fully explored in the previous DOE work are discussed, and the potential effects of these aspects on the thermal stress distribution are addressed. This examination calls into question the conclusion that a mountain-scale stress state alteration should be expected. Simple, first-order calculations are used to demonstrate a large fraction of thermal-expansion strain from waste-generated heat can be accommodated through fracture closure. Thermally induced stress, therefore, would be much smaller than suggested by DOE, reducing the likelihood for large-scale reorientation of the principal stresses.

CONTENTS

FIGURES

TABLES

ACKNOWLEDGMENTS

This report was prepared to document work performed by the Center for Nuclear Waste Regulatory Analyses™ (CNWRA™) for the U.S. Nuclear Regulatory Commission (NRC) under Contract No. NRC–02–02–012. The activities reported here were performed on behalf of the NRC Office of Nuclear Material Safety and Safeguards, Division of Waste Management. The report is an independent product of the CNWRA and does not necessarily reflect the views or regulatory position of the NRC.

The author thanks G. Ofoegbu, H.L. McKague, and W. Patrick for their reviews of this report. The author also thanks B. Hill and D. Ferrill for their thoughtful discussions during the course of this work. The author is grateful to S. Odam for assisting with the word processing and preparation of the final report and to C. Cudd and B. Long for editorial reviews.

QUALITY OF DATA, ANALYSES, AND CODE DEVELOPMENT

DATA: All CNWRA-original data contained in this report were collected and analyzed to meet quality assurance requirements as described in the CNWRA Quality Assurance Manual and documented in Scientific Notebook 606E. Sources for all other data should be consulted to determine the level of quality for these data.

ANALYSES AND CODES: Although no CNWRA-developed codes were used to analyze data for this report, the commercially available spreadsheet software Microsoft® Excel 2002 was employed. Generation of figures was aided by use of RockWare StereoStat® Version 1.2 (commercially available stereonet plotting program), Adobe® Illustrator® Version 10 (commercially available drawing software), and 3DStress™ (CNWRA-developed software).

1 INTRODUCTION

Yucca Mountain in southwestern Nevada is the site of the United State's potential high-level waste repository. One concern with regard to the repository is the potential consequences of an igneous event such as the intrusion of an igneous dike, a volcanic eruption, or both. Assessing the likely consequences of an igneous event on the potential repository is difficult because geologic processes are inherently variable and a function of multiple interdependent variables (e.g., stress, temperature, fluid, and materials). This report discusses only the potential for stress-state modification resulting from heat generated by emplacement of the high-level waste packages.

Although it is generally agreed among researchers that some localized modification of the *in-situ* stress state is likely in response to the thermal load from radioactive decay, the temporal and spatial extents of this alteration are unclear. Part of the uncertainty can be traced to differences in necessary simplifying assumptions. This report begins by reviewing the existing body of research with particular emphasis on the choices of assumptions and their potential effects on analyses results.

1.1 Motivation for Investigation

The investigation was prompted by a need to understand: (i) what effect (if any) the heat from emplaced waste will have on the repository-scale state of stress (absolute and relative magnitudes and directions of principal stresses) around the potential repository (i.e., spatial scale of tens of square kilometers), and (ii) what effect the stress-state alteration will have on a propagating igneous dike as it approaches the repository. These questions are important because preliminary performance assessments indicate disruption of the potential repository by extrusive igneous events may be the greatest contributor to overall risk (NRC, 2002).

1.2 Statement of Problem

The *in-situ* stress state at Yucca Mountain (Stock and Healy, 1988) is characterized by a vertical maximum principal stress ($\sigma_1 = \sigma_v$). Estimates of vertical stress magnitude at depths of 295 and 418 m [968 ft and 1,371 ft] are 6.1 and 8.4 MPa [885 and 1,218 psi] (Stock and Healy, 1988) and are in general agreement with overburden calculations assuming an average rock density of 2,100 kg/m^3 [0.760 lbs/in^3]. The minimum horizontal stress ($\sigma_h = \sigma_3$) based on hydraulic fracturing stress measurements is oriented 120° ± 10° with an average magnitude of 0.5 σ_v (± 0.1). The estimated average magnitude of the maximum horizontal stress ($\sigma_H = \sigma_2$) is 0.7 σ_v (± 0.1). Importantly, the majority of stress measurements were made at depths of 1,000 to 1,500 m [3,281 to 4,922 ft] (Stock and Healy, 1988).

Two general alternatives have been suggested for stress-state modification.

(1) The change in stress state because of thermal loading from waste package emplacement will be relatively minor, localized, or relatively homogeneous (Barr, 2000; Detournay, et al., 2003).

(2) The thermal load will increase temperatures that are likely to induce significant stress changes across the entire repository area, and these strongly inhomogeneous and

anisotropic stresses will induce a widespread change in the repository-scale stress field such that the minimum principal stress is rotated from horizontal to vertical (Barr, 2000; Detournay, et al., 2003).

These analyses, however, may oversimplify the potential thermal stress distribution in that analyses are typically based on two assumptions: the geologic medium is mechanically homogeneous and stratigraphic interfaces and the ground surface are planar and horizontal.

If the first alternative is correct, it is unlikely a propagating dike will be influenced as it approaches the repository. The second scenario, however, would suggest thermal effects of the repository will play an active role in the trajectory of dike propagation because dike orientation is strongly controlled by the orientation of the minimum principal stress (i.e., dike will propagate along the σ_1-σ_2 plane).

Barr (2000) suggests significant alteration of the repository-scale stress state is a likely consequence of waste emplacement (alternative 2). This stress-state modification reorients the principal stress axes such that the minimum principal stress becomes vertical (i.e., $\sigma_3 = \sigma_v$). Barr uses this conclusion to argue that an approaching dike, which is propagating in the σ_1-σ_2 plane (i.e., opening in the σ_3 direction), will shift to a horizontal sill at some depth (on the order of hundreds of meters) below the repository when it encounters the thermally altered stress field. Consequently, the intrusion would be turned away from the repository, negating any repository-dike interaction.

Before analyzing dike-drift interaction scenarios, it is important to reassess the thermal modification of the *in-situ* stress state. Of critical importance are potential changes in both magnitude (absolute and relative) and orientation of the stress state as represented by the principal stresses. This issue is complicated with numerous, mutually dependent variables to consider. The following two questions are posed as a guide to this analysis:

(1) Is it geologically realistic to conclude the stress state will be significantly changed across Yucca Mountain in response to heating from emplacement of high-level waste?

(2) What aspects of the geologic framework have been neglected by previous analyses, and what are the likely effects of these features on the thermal stress distribution?

Within this framework, some aspects of the geology that have been underemphasized in the earlier work are addressed. Then, the previous analyses that led to the proposal of alternative (2) are summarized, including the assumptions and simplifications employed. Finally, a simple, but geologically realistic analysis is developed that considers the potential thermal effect of waste canister heat on the *in-situ* stress state if the natural fractures in the repository host rocks are explicitly considered. The goal is not to completely answer all questions regarding thermal effects on stress state, but rather to demonstrate that one or more aspects of the geology not represented in the previous analyses are sufficiently important to require a reevaluation of current U.S. Department of Energy (DOE) conclusions.

2 ADDITIONAL CONSIDERATIONS

Numerous additional considerations are either not addressed or addressed incompletely in the previous analyses of the thermal effects of waste emplacement. These considerations are discussed in the following sections.

2.1 Realistic Geologic Framework Model

No analyses to date have used a physically realistic geologic framework model. Although it is understandable that few, if any, three-dimensional simulations have been developed that employ a realistic subsurface geometry, it is less clear why features such as stratigraphic variability and major faults are almost completely absent from existing analyses.

Even an accurate and realistic topographic profile has been omitted. The potential repository location is at a maximum depth of ~350 m [1,148 ft] below the surface; however, depth is not constant (Figure 2-1). The repository host horizon is within <300 m [984 ft] of the surface along the eastern boundary. The western margin along Solitario Canyon shows a greater difference with the drift to surface distance at ~180 m [~590 ft]. This lateral variability, which provides a nearly 50-percent difference in overburden load, could significantly alter analysis results (Swolfs and Savage, 1985; Liu and Zoback, 1992; Pan, et al., 1995; Tan, et al., 2004) and should be evaluated.

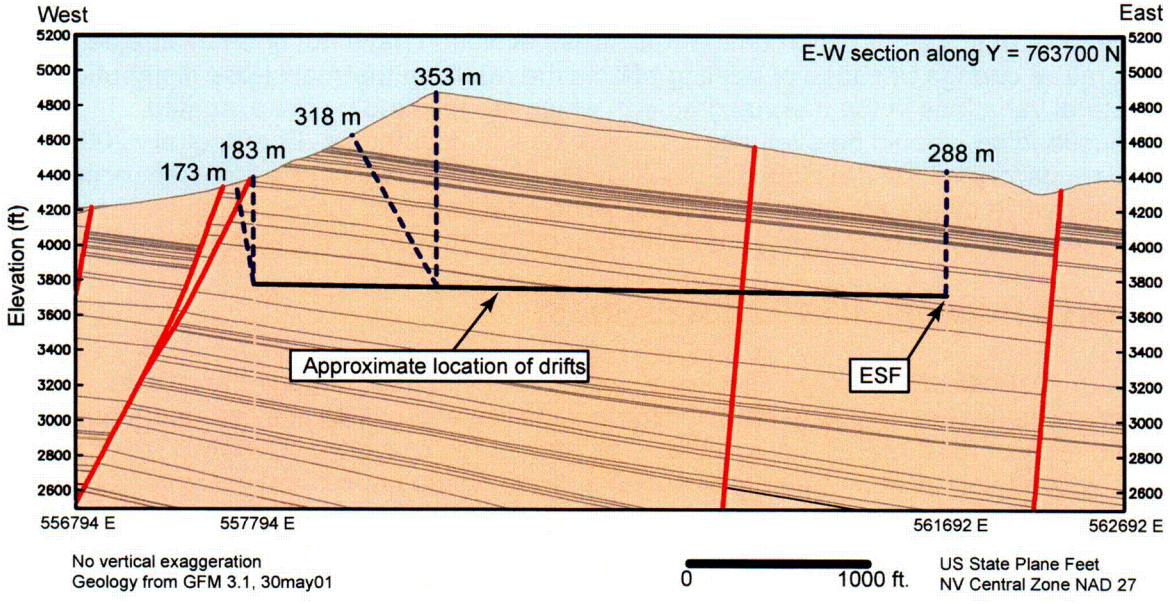

Figure 2-1. Simplified east-west geologic cross section of Yucca Mountain region showing location of potential repository with respect to topographic surface (modified from Hill, 2003, personal communication). Geologic information was extracted from the Geologic Framework Model, Version 3.1 on May 30, 2001. Blue dashed lines show distance from potential repository horizon to ground surface along either vertical line or normal to ground surface. The approximate location of the drifts and the Exploratory Studies Facility (ESF) is also shown for reference.

C01

2.2 Repository Geometry and Waste Emplacement Changes

Nearly all previous analyses are based partly or completely on repository geometries no longer being considered. A vertical waste emplacement configuration dominates the early (pre-1999) analyses, while current designs use horizontal in-drift emplacement. The current waste package configuration along with the absence of backfill in the drifts and the current expectation of preclosure ventilation suggests heat output will be substantially lower than that used in most early analyses (CRWMS M&O, 2000a; DOE, 2002). Despite this significant change in the initial loading condition, the analyses that lead to the conclusions of stress-state alteration have not been reevaluated.

Initial repository layout (MacDougall, et al., 1987) employed emplacement drifts that would be parallel to the *in-situ* maximum principal stress (030°), and this configuration dominates most analyses. The current repository layout uses emplacement along tunnels at ~072° such that neither horizontal stress is aligned with the drifts (Board, et al., 2002; DOE, 2002). Again, this aspect should be evaluated for its effect on the overall stress.

The current design specifies a drift spacing of 81 m [266 ft]. The few analyses that have employed this geometry (e.g., Ofoegbu, 2001, 2000; Ofoegbu, et al., 2001) demonstrate the thermal effect of individual drifts only partially extends to adjacent drifts. This means the repository is not really represented by a rectangular heat source, but rather as a series of subparallel linear heat sources. Generally, it has been assumed the entire repository is loaded instantaneously (i.e., time of complete emplacement of all waste is much less than analysis time). The effects of this assumption on thermal stress evolution have not been evaluated. Total temperature change because of heating affects the resulting thermal stress distribution, however, lateral variations in the thermal gradient, which are masked by the assumed instantaneous loading, should be evaluated. Current design documents (Board, et al., 2002) suggest the repository will be developed as individual panels with waste emplacement occurring in some panels while others are being excavated. The heat load will, therefore, be temporally and spatially variable; neither of these effects have been addressed by the previous analyses.

2.3 Material Heterogeneity and Anisotropy

Previous thermal stress analyses typically have used a simple elastic behavior and have assumed the rocks (in the repository host horizon and above and below) are homogeneous and isotropic with respect to all material properties. The stratigraphic layering (CRWMS M&O, 2000b) with welded versus nonwelded tuffs and lithophysal versus nonlithophysal intervals leads to large vertical variations in some material properties such as density, thermal conductivity, and coefficient of thermal expansion (CRWMS M&O, 2000b). These variations contribute to an anisotropy that will affect all but the smallest-scale analyses, and the effects of this anisotropy have not been assessed. In addition, the fracture characterization of the repository host horizon interval demonstrates the distribution of rock discontinuities is both heterogeneous and anisotropic (e.g., Mongano, et al., 1999; Nieder-Westermann, 2000; Board, 2003). Although some rock mass material properties (e.g., Young's Modulus) have been reduced to account for the increased compliance of rock masses compared with small test samples, no attempt has been made to capture the heterogeneity or anisotropy.

2.4 Stress Increase Versus Rock Strength

In previous analyses, the general approach has been to employ a single thermal analysis step to determine a temperature distribution that is then used as input for a subsequent stress analysis step. Resulting stress increases are sometimes physically unrealistic considering that such analyses indicate that rock strength would be exceeded at several locations within the rock mass (cf. Ofoegbu, 2001). The physically unrealistic stresses result because incremental temperature changes are not coupled to incremental stress changes.

Rock response to thermal loading is generally assessed by only one or two potential strain mechanisms (e.g., closure or sliding of existing joints) rather than for other potential mechanisms (e.g., formation of new fractures). Rock deformation often includes nonlinear and nonrecoverable processes where path dependence cannot be neglected (Elliott, 1972; Groshong, 1988; Twiss and Moores, 1992). Assuming stresses or strains from an initial elastic step are appropriate inputs for subsequent inelastic analyses does not reflect accurately the physics of the process, and, therefore, the conclusion concerning deformation evolution may be incorrect. Interestingly, Hardy and Bauer (1991, p. 5-6) note this but then neglect to incorporate it into their final analysis even though they clearly demonstrate this type of behavior.

3 PREVIOUS THERMAL-MECHANICAL MODELING ANALYSES

This chapter briefly summarizes the previous research conducted on the effects of thermal processes on the *in-situ* stress state around the potential repository. For simplicity, the material is presented chronologically.

3.1 Summary of Mack, et al. (1989)

Mack, et al. (1989) summarize the results of two-dimensional numerical analyses using boundary element and distinct element methods that estimate the extent of rock stress modification caused by heat generation from high-level waste emplaced in a hypothetical repository. Rock mass modification is assessed as changes in joint deformation for simulated rock containing only vertical joints. Both the thermoelastic boundary element code HEFF and the distinct element code UDEC were used by Mack, et al.

Mack, et al. (1989) employ two simple relationships to determine joint aperture change and joint slip. The relationship of Barton, et al. (1985) is used for joint aperture change (ΔV_j):

$$\Delta V_j = \frac{a\sigma_N}{1 + b\sigma_N} \tag{3-1}$$

where σ_N is the normal stress on the joint, and a and b are characteristic parameters. Mack, et al. (1989) use values of a = 0.016 mm·MPa^{-1} [4.34 × 10^{-6} in·psi^{-1}], and b = 0.909 MPa^{-1} [6.27 × 10^{-3} psi^{-1}] for their analyses. Joint slip is determined from a standard Mohr-Coulomb criterion where the shear stress (τ) necessary for slip is given by

$$\tau = c_o + \sigma_N \tan\phi \tag{3-2}$$

where c_o is the joint cohesion and ϕ is the friction angle. Mack, et al. (1989) use values of c_o = 0.1 MPa [14.5 psi], and ϕ = 28° for the welded tuff. For the interaction between the tuff and adjacent units, they use c_o = 0, and ϕ = 10 or 28° for clay-filled or rough joints. For the HEFF models, Mack, et al. treat the rock as isotropic and homogeneous with properties meant to simulate the nonlithophysal Topopah Spring member.

With regard to heat generation from waste canisters, initial power values [$P(t)$ for t = 0] of 3.2 and 0.42 kW [3.03 and 0.40 BTU/sec] are chosen for the spent nuclear fuel and defense high-level waste containers. Initial power values are based on the thermal decay characteristics for waste 10 years out of the reactor, as given by Peters (1983).

Room geometries for both vertical and horizontal waste emplacement in pillars are analyzed, and Mack, et al. (1989) note the initial thermal loading for their conditions is approximately 80 kW/acre [48,527 BTU/sec·mi^2] rather than the more often quoted value of 57 kW/acre [34,576 BTU/sec·mi^2]. Two *in-situ* stress states are investigated: (i) $\sigma_{xx} = \sigma_H$ = 1.5 MPa [218 psi], $\sigma_{yy} = \sigma_v$ = 5 MPa [725 psi]; and (ii) $\sigma_{xx} = \sigma_H$ = 3 MPa [435 psi], $\sigma_{yy} = \sigma_v$ = 5 MPa [725 psi]. For purposes of the simulation, Mack, et al. (1989) consider all joints to be vertical.

HEFF results for the room-scale analyses show excavation of the tunnel induces small regions where *in-situ* stresses change by >10 percent (positive versus negative change is unspecified). Joint aperture reduction of more than a factor of two takes place in a small area under the tunnel, and joint slip is restricted to a region less than two room diameters wide. The effects of waste emplacement are presented as predicted temperature distributions after 100 years {maximum temperature of 160 °C [320 °F] in the vicinity of vertically emplaced waste} along with the effects on joint aperture and joint slip. The regions of joint aperture reduction by >2 are widely distributed for vertical and horizontal emplacements at t = 100 years. For all cases, joint slip is localized to regions approximately 0.5–1 room diameter around the tunnels. Mack, et al. (1989) do not show explicitly the effects of waste emplacement on the stress state (i.e., a modified stress plot), but rather focus their analyses on the aperture change and joint slip that result. It can be inferred, however, that the thermally induced stress increases will not be as great as they would be for a horizontally constrained material because the closure, slip, or both will partially relieve the thermal stresses.

HEFF results for the repository-scale analyses are presented only for the case of vertical emplacement within a single drift and show that a zone of aperture decrease forms around the tunnel and grows throughout the analysis period (t_{max} = 500 years). Zones of aperture increase are predicted above and below the repository horizon, reaching a maximum after 100 years and virtually disappearing by 500 years. Regions of slip on the vertical joints also develop, although primarily these are above the repository horizon. In general, the regions of modification are larger for simulations where the initial stress ratio is low {σ_{xx}/σ_{yy} = 1.5/5.0 MPa [218/725 psi]}.

For the UDEC models, Mack, et al. (1989) treat the rock as isotropic and homogeneous with the addition of explicit vertical joints spaced 100 m [328 ft] apart above and below the repository horizon and 200 m [656 ft] apart beyond the edge. Rock-mass properties are used between the joints, but unlike the HEFF models, the UDEC models use a linear joint behavior:

$$\Delta V_j = \frac{1}{K_j}\sigma_N \tag{3-3}$$

where K_j is the initial joint stiffness {3.5×10^5 MPa/m [1.55×10^7 psi/ft]}. The stiffness in the linear joint model is higher than the nonlinear model at low normal stresses but lower than the nonlinear model at higher normal stresses. The initial horizontal and vertical stresses were varied linearly with depth from zero at the ground surface to values of approximately 2 and 7 MPa [290 and 1,015 psi] at the repository horizon.

UDEC results for the repository-scale analyses are presented as predicted temperature {T = 0 °C [32 °F] at t = 0} contours up to t = 500 years (Figure 3-1). Maximum temperatures immediately adjacent to the repository of 100–110 °C [212 to 230 °F] are reached within 50–100 years. By 500 years, the maximum temperature is only approximately 70 °C [158°F]. As Figure 3-1 demonstrates, Mack, et al., (1989) found that temperature changes of >50 °C [120 °F] are restricted to distances of << 100 m [328 ft] above and below the drifts. The results show a region nearly 100 m [328 ft] wide above and below the repository will undergo joint aperture closure of as much as 0.05 mm [1.97×10^{-3} in], and that the region will increase with time. Beyond the regions of joint closure are regions where slight joint opening {<0.01 mm [3.94×10^{-4} in]} is predicted. Similar to the HEFF models, the UDEC models predict small localized regions of joint slip primarily above the repository horizon.

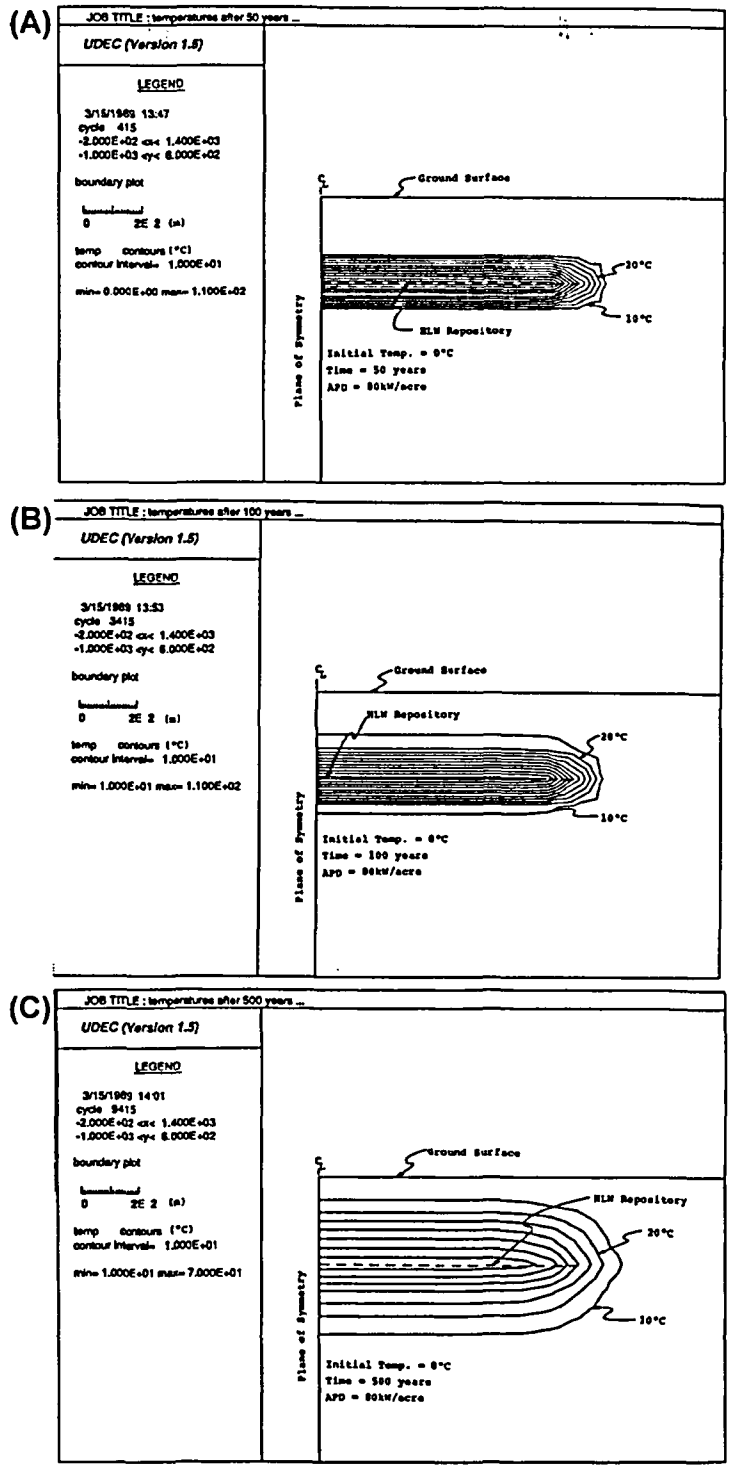

Figure 3-1. Contours of rock temperature change (°C) for repository-scale thermal modeling (from Mack, et al., 1989). Temperature changes are shown for (A) 50 years, (B) 100 years, and (C) 500 years following waste emplacement. NOTE: Information is provided in °C, for conversion, use 1.8 × °C + 32 = °F.

In summary, Mack, et al. (1989) show tunnel excavation induces stress magnitude changes of >10 percent close to the repository, and these stress changes may induce localized joint closure, slip, or both. Room-scale analysis results from a thermoelastic boundary element model using HEFF suggest a modification zone—where modification is marked by either joint slip or opening—extends to approximately two room diameters. Repository-scale analysis results from HEFF and the distinct element code UDEC suggest a zone of rock mass modification will develop ~100 m [~330 ft] above and below the repository, with thicknesses of 200 and 150 m [656 and 492 ft], above and below. Mack, et al. also demonstrate joint aperture closure and slip should occur in response to heat released from waste canisters for both the room-scale and the repository-scale analyses. The report, however, does not explicitly document the changes in stress magnitude or direction caused by thermal effects.

3.2 Summary of Hardy and Bauer (1991)

Hardy and Bauer (1991) consider the effects of superposition of thermal, seismic, or both stresses on the *in-situ* stress state around the potential waste emplacement drift. The *in-situ* stress state for this analysis is $\sigma_1 = \sigma_v = 7.0$ MPa [1,015 psi], $\sigma_2 = \sigma_H = 4.2$ MPa [609 psi] @ ~030°, $\sigma_3 = \sigma_h = 3.5$ MPa [508 psi] @ ~120°. The repository layout at the time the analyses were performed had the tuff main access and emplacement-drift axes parallel to σ_H, and the midpanel access drifts parallel to σ_h (Hardy and Bauer, 1991, Figure 5-4). Thermal stress effects for the waste emplacement drifts are calculated via a transient heat flow analysis that simulates a period from waste emplacement to 100 years after waste emplacement. Calculated temperature changes are fed to a coupled, thermomechanical analysis with thermal stress changes produced by the resulting temperature-induced thermal expansion of the rock mass. This step is summarized by Hardy and Bauer (1991), however, the report does not include a detailed description of the procedure. Thermal stresses for the midpanel and tuff main access drifts were derived from three-dimensional thermomechanical simulations of the repository. The simulations produce estimates of the stress state at the centerline of the drift, and these are imposed as boundary conditions on the finite-element meshes for the midpanel and tuff main access drifts.

Hardy and Bauer (1991) do not present thermal stress results for the emplacement drift calculations. Results for the midpanel and main access drifts are given based on an elastic analysis of a homogeneous host rock with an elastic modulus of 15.2 GPa [2.2×10^6 psi]. Results for the midpanel drift only are then converted to thermal stress values for each of five rock mass quality categories. Thermal stress values are highest for category 5 (i.e., best rock). Maximum horizontal thermal stress values (σ_{xx}) range from 2.6 to 21.8 MPa [377 to 3,162 psi] (positive in compression). Minimum horizontal thermal stress values (σ_{yy}) range from 1.7 to 14.4 MPa [247 to 2,088 psi]. Vertical thermal stress values (σ_{zz}) range from -0.6 to -5.0 MPa [-87 to -725 psi]. Results of superimposing the thermal and *in-situ* stress states for 100 years are shown in Table 3-1 (Hardy and Bauer, 1991). The analyses suggest minimum principal stress is vertical ($\sigma_v = \sigma_3$) after 100 years for all but the category 1 rock.

Overall results are presented for JAC (a Sandia laboratory finite-element code) simulations of the tuff main access, midpanel access, and emplacement drifts using elastic-plastic (Mohr-Coulomb) and compliant-joint constitutive relationships. For all configurations, results are given for the *in-situ* + thermal + seismic and the *in-situ* + seismic cases. Hardy and Bauer (1991) also provide results for the *in-situ* + thermal case for the emplacement drift configuration.

Table 3-1. Stress State in MPa after 100 Years Resulting from Superposition of *In-Situ* and Thermal Stresses for Each Rock Mass Quality Category (Modified from Hardy and Bauer*). The Minimum Principal Stress (σ_3) Is Highlighted for Each Category.			
Rock Mass Quality†	σ_{xx}	σ_{yy}	σ_{zz}
1	6.8 [986 psi]	5.2 [754 psi]	6.4 [928 psi]
2	8.8 [1,276 psi]	7.5 [1,088 psi]	6.0 [870 psi]
3	13.8 [2,002 psi]	9.8 [1,421 psi]	4.8 [696 psi]
4	25.8 [3,742 psi]	17.8 [2,582 psi]	2.0 [290 psi]
5	26.0 [3,771 psi]	17.9 [2,596 psi]	2.0 [290 psi]

*Hardy, M.P. and S.J. Bauer. "Drift Design Methodology and Preliminary Application for the Yucca Mountain Site Characterization Project." SAND89-0837. Albuquerque, New Mexico: Sandia National Laboratories. 1991. (Table 12-27).
†Note: Rock mass quality ranges from worst (1) to best (5).

Results are tabulated for the extent of yield zones determined from plastic yield, crushing strain, or extensional strain. In general, the yield zones are 0.5–2.0 m [1.64–6.56 ft] wide.

In summary, Hardy and Bauer (1991) suggest the stress state around the potential repository will be altered (mildly to variable extents) by heat flow from the waste canisters. It is difficult to judge the adequacy of their analyses because: (i) a clear description of the model details is not provided in the report (e.g., geometry and boundary conditions); (ii) thermal stresses are calculated from an elastic analysis and later fed into inelastic analyses, but this approach is not described clearly enough to determine if it is justified; and (iii) only distilled summaries of the stress results at 100 years are provided rather than the detailed change.

3.3 Summary of Hardy and Bauer (1992)

This short report presents selected results from and reaffirms the main conclusions of Hardy and Bauer (1991). The key graphs used in this report (Hardy and Bauer, 1992, Figure 3), however, do not appear in the earlier report, nor can the raw data used to generate the graphs be located in the earlier report. Because the figure is given widespread use by DOE as support for an interpretation of the temporal evolution of principal stress magnitudes (e.g., Barr, 2000, Figures 2 and 3, p. 49), independent substantiation is needed to confirm the data and interpretation.

3.4 Summary of Ofoegbu (1999)

Ofoegbu (1999) presents results of finite-element analyses of the emplacement-drift area for the potential repository. This repository-scale analysis focuses on assessment of drift stability as indicated by spatial variation of rock-mass quality (Q) and accumulation of inelastic (plastic) strain. The models are two-dimensional with 100 drifts at a center-to-center spacing of 28 m [92 ft] (based on older drift design). Each drift is modeled as a 5 × 5-m [16 × 16-ft] square so that interdrift pillar width is 23 m [75 ft]. An initial heat conduction analysis using a time-decaying volumetric heat source applied uniformly within the perimeter of each drift provides the temperature history for a period of 150 years. The temperature history serves as

input for the mechanical analyses. Two mechanical analyses are presented that represent cases with stiff drift support and degraded drift support.

Analysis results show accumulation of the inelastic strain and Q values. No stress results are presented by Ofoegbu (1999), although this was not the primary focus of the analysis. For the case of stiff drift support, greatest inelastic strain occurs at the midpoint of the interdrift pillars with secondary highs at the roof and floor of each drift opening. Ofoegbu observes higher strains generally correlate with higher Q values and infers this to be a reflection of the greater rock-mass stiffness. For the case with drift-support degradation, Ofoegbu finds inelastic strain is greater throughout the model domain and is particularly prevalent in the floor and roof areas of the drift openings. Unlike the stiff support case, the degraded drift case shows increased strain in areas of lower Q values. Ofoegbu interprets this result as reflecting stress changes induced by the rapid removal of the drift support in the simulation. This complete loss of confinement causes greater strain in the areas with lower Q values.

3.5 Summary of Ofoegbu (2000)

Ofoegbu (2000) analyzes finite-element simulations that address changes in rock-mass hydrological properties in response to thermal loading at the potential repository. Unlike Ofoegbu (1999), this analysis is drift-scale. The drift is represented by a 5.5-m [18-ft] diameter circle, and the geometry is based on the current design with a drift spacing of 81 m [266 ft]. As with Ofoegbu (1999), the analyses consist of sequentially coupled heat conduction and static stress analyses. The heat-conduction step uses a time-decaying volumetric heat source with an initial strength of 1.266 kW/m [0.366 BTU/s·ft] decaying to 0.0166 kW/m [4.80×10^{-3} BTU/s·ft] at 10,000 years.

The mechanical analysis employs three steps: (i) establish static equilibrium, (ii) removal of material to simulate drift excavation, and (iii) application of temperature history from heat conduction analysis. Simulations were performed for a 150-year period. Ofoegbu (2000) analyzes two cases that represent a high rock-mass quality (RMQ5) and a low rock-mass quality (RMQ1). For elastic-plastic analyses, the rock-mass dilation angle (ψ) was set to 50 percent of the rock-mass friction angle (ϕ = 27.5 or 34.4°). Poisson's ratio is set to 0.21, Young's Modulus to 7.8 or 32.6 GPa [1.13×10^6 or 4.73×10^6 psi], and specific heat capacity and thermal expansivity were defined with a temperature dependence. Additional material parameters employed by Ofoegbu (2000) are unconfined compressive strength (reduced 50 percent of the intact-rock value) = 84 MPa [12,182 psi] and cohesion = 2.82 or 5.08 MPa [409 or 737 psi]. Although some models use a constant cohesion, others use cohesion degradation. The degradation is defined by constant cohesion for t <50 years, cohesion reduction by 50 percent of the initial value for the period 50 <t <100, and then constant cohesion at 50 percent of initial value for the remainder of the simulation.

Distributions of horizontal and vertical stresses (Figure 3-2) from linear elastic analyses are presented (Ofoegbu, 2000). Results show increases in horizontal stress (at t = 150 years) almost everywhere around the drifts except for small areas near the drift sidewall. Horizontal stress distribution is shown to be relatively insensitive to rock quality, although the better rock (RMQ5) develops larger stress magnitude. Vertical stresses generally increase immediately around the drift openings, but may increase or decrease slightly {less than ± 5 MPa [725 psi]} in the pillar region. The majority of results presented in Ofoegbu is elastic-plastic analyses that focus on assessment of permeability changes as reflected by the fracture-permeability change

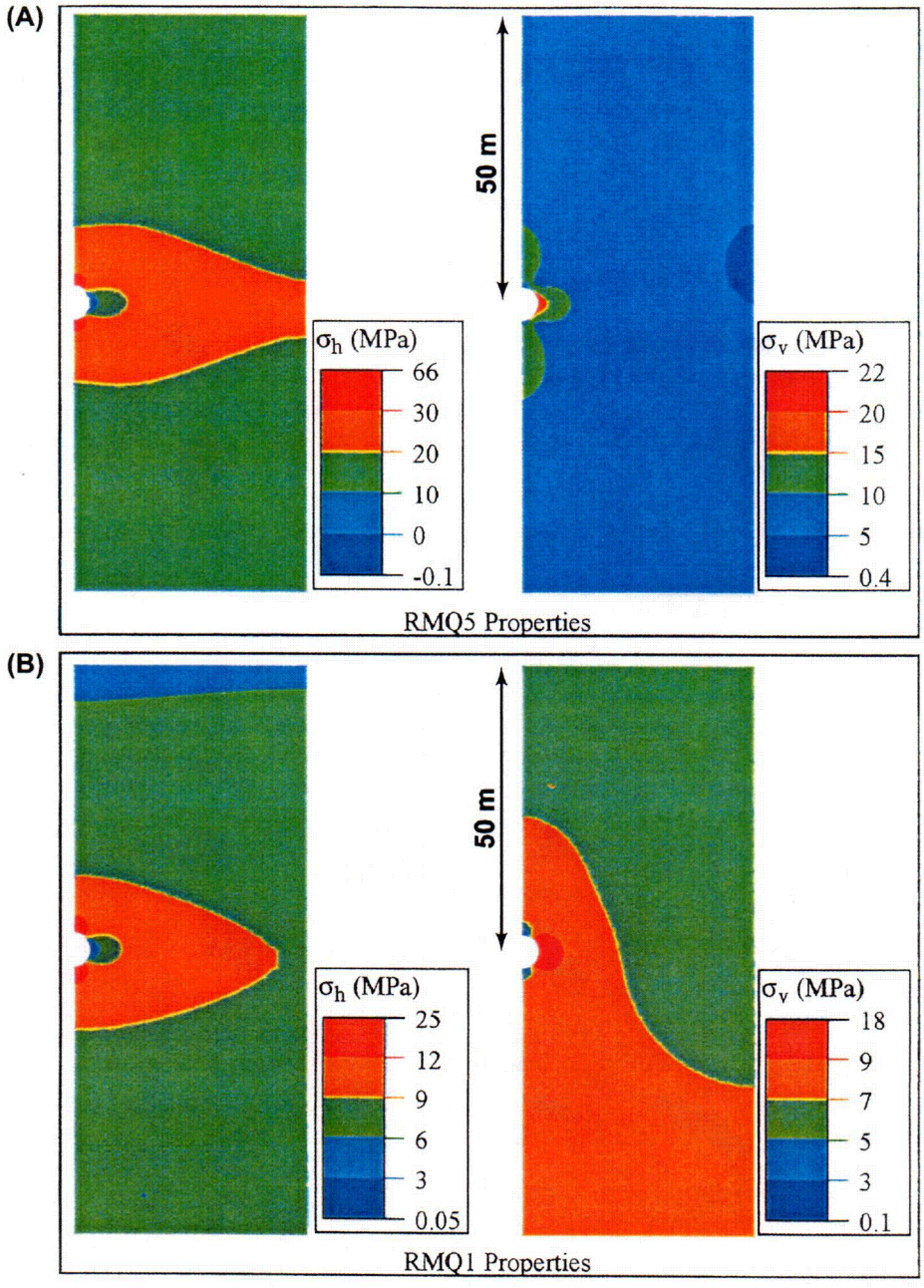

Figure 3-2. Distributions of vertical and horizontal stresses at 150 years following waste emplacement drift-scale thermomechanical analyses for (A) good rock (RMQ5) and (B) poor rock (RMQ1) (from Ofoegbu, 2000).

C02

ratio (R_k) for the different cases (Figures 3-3 and 3-4). The estimate of R_k is based on an inferred relationship between inelastic volumetric strain (ε^N) and the change in fracture porosity ($\Delta\varphi_f$). Ofoegbu states the inelastic volumetric strain, easily extracted from the elastic-plastic models, can be used as a direct measure of thermal alteration or increase in fracture porosity (i.e., the strain reflects fracture slip that, in turn, results in overall dilation of the rock mass). Results (Figures 3-3 and 3-4) suggest most thermal alteration is restricted to regions either near the drift opening or at the middle of the interdrift pillars.

3.6 Summary of Barr (2000)

Barr (2000) focuses on the potential interactions of a hypothetical dike and a repository drift and presents two conceptual models for dike/drift interaction:

(1) The drift represents an insignificant heterogeneity such that the dike propagation is essentially unaffected.

(2) The dike strongly interacts with a stress-altered region that surrounds the repository.

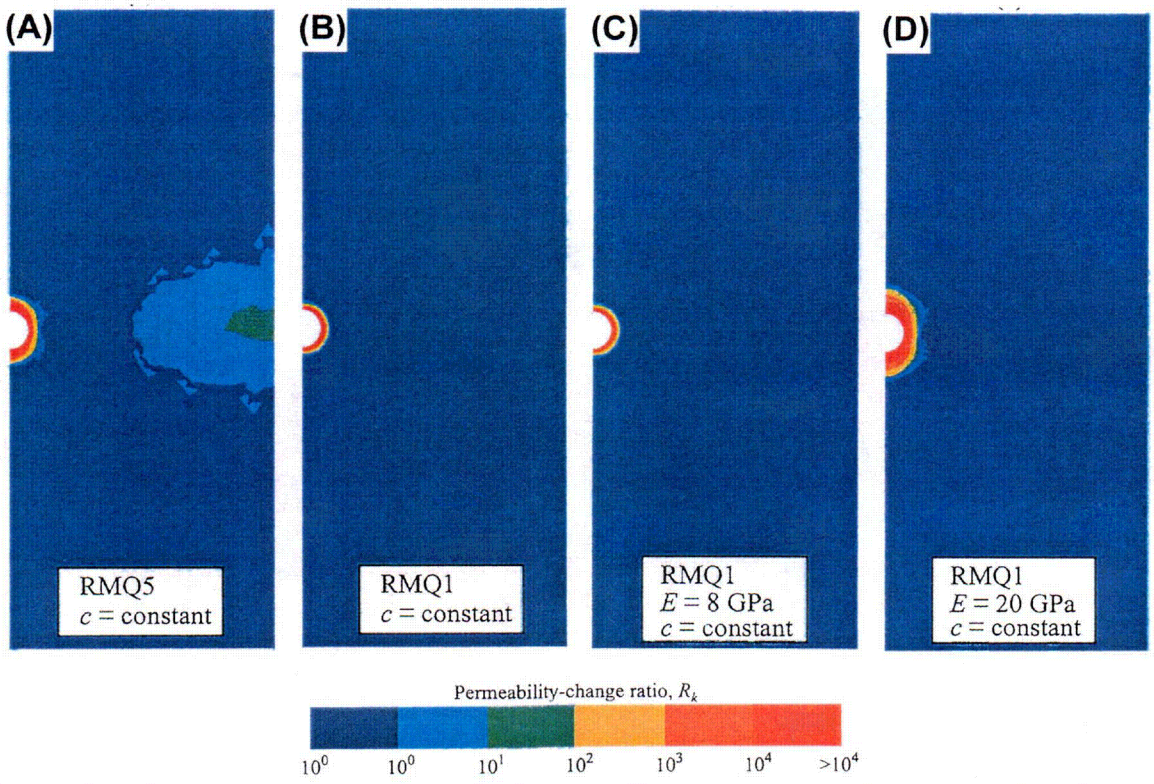

Figure 3-3. Fracture-permeability change ratio (R_k) associated with inelastic response at 150 years after waste emplacement (modified from Ofoegbu, 2000). Effects of rock-mass quality are shown for (A) good rock and (B) poor rock. Effects of rock-mass stiffness are shown for (C) weak rock and (D) strong rock.

C03

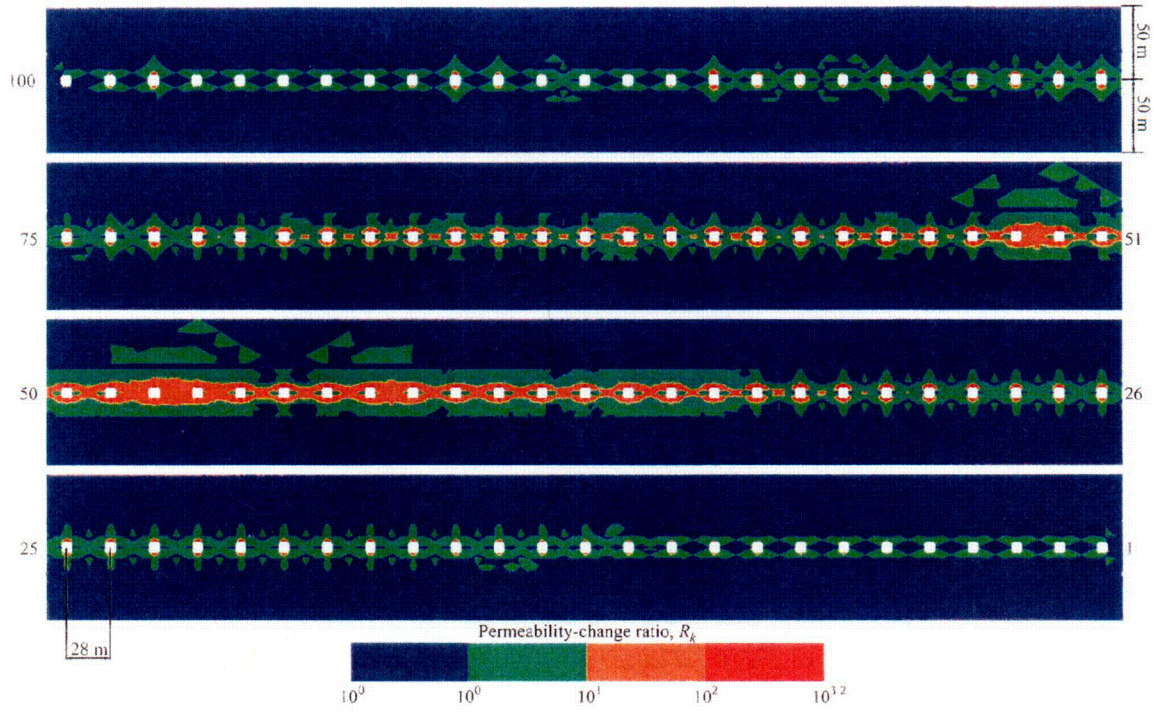

Figure 3-4. Fracture-permeability change ratio (R_k) for repository-scale model associated with inelastic response at 150 years following waste emplacement (from Ofoegbu, 2000). White squares represent individual emplacement drifts with 81 m [266 ft] center-to-center spacing.

Barr (2000) states the second scenario is the physically more complete conceptual model without providing any clear supporting documentation. This choice influences the conclusions in the report. The altered zone in the second scenario is a temporally variable region that results from the superposition of the *in-situ* stress state and the effects of tunnel excavation and heat generation from waste emplacement. In discussing the thermomechanical evolution of the repository, Barr summarizes information from earlier works (e.g., Mack, et al., 1989; Hardy and Bauer,1992, 1991) and concludes the horizontal stresses surrounding the potential repository will increase from the initial levels of 3–6 MPa [435–870 psi] to 15–20 MPa [2,175–2,901 psi]. This magnitude change causes the vertical stress to become the minimum principal stress for the time period of ~10–2,000 years after waste emplacement.

As previously discussed, the Hardy and Bauer (1992, 1991) results are inconclusive and contain numerous inconsistencies. In addition, Barr (2000) incorrectly cites Mack, et al. (1989) in support of thermal stress alteration around the repository. As discussed earlier, Mack, et al. document changes in stress magnitude and direction for excavation of the emplacement tunnels. They do not, however, explicitly address stress modification because of thermal effects of waste emplacement. All results that incorporate thermal effects are presented as behavior (closing, opening, and sliding) of the vertical joints. The joint strains clearly indicate changes in the stress state are occurring, however, Mack, et al. do not report the magnitude or orientations of the principal stresses.

C04

3.7 Summary of Ofoegbu, et al. (2001)

Ofoegbu, et al. (2001) discuss the thermal and geomechanical effects on percolation flux through the unsaturated zone at the potential repository. Aspects of fracture-aperture change because of thermal loading are reiterated from Ofoegbu (2000). Ofoegbu, et al. (2001) emphasize thermal-mechanical alteration will be laterally discontinuous with localization near emplacement drifts and at the centers of interdrift pillars. They also conclude the changes in fracture aperture within these zones, relative to magnitude and style (opening, closing, and sliding), are a function of multiple inputs including the rock mass quality and the rheological response (elastic versus inelastic). The second point is worthy of further consideration because most research on thermal effects on the stress state at Yucca Mountain assumes elastic behavior without consideration of the effects of inelastic deformation.

3.8 Summary of Ofoegbu (2001)

Ofoegbu (2001) also synthesizes results of finite-element analyses (Ofoegbu, 2000) that focus on changes in rock-mass hydrological properties in response to thermal loading at the potential repository. Earlier analyses are extended to address the potential for rock failure under the conditions of a thermally altered stress state. Linear elastic analyses for high stiffness (RMQ5) and low stiffness rock (RMQ1) indicate failure is possible in the drift roof and the sidewall areas because stress increases would exceed rock strength. Results for the midpillar areas, however, are dependent on rock quality. Stress increases would approach failure values for the high stiffness rock. In contrast, stresses in the midpillar areas appear to decrease for the low stiffness rock (RMQ1), suggesting failure in shear is less likely.

3.9 Summary of Detournay, et al. (2003)

Detournay, et al. (2003) focus on evaluating the technical basis used to analyze potential consequences of igneous events that impact the potential repository. Although the majority of this report does not address thermal stress, the topic is broached several times, because the overall thermomechanical framework of the repository volume influences processes such as dike propagation direction and velocity. In particular, Detournay, et al. speculate large thermal stresses would reduce the size of the tip cavity ahead of an advancing magma front. The result, in their opinion, is a greater likelihood for a violent eruption of magma into the potential repository tunnels. The possible conversion of a dike into a subhorizontal sill is mentioned, however, Detournay, et al. consider the thermal stress effects to be time-limited and prefer an approach that assumes all dikes maintain a near vertical propagation path. Thermal analyses by Ofoegbu (2000) demonstrate that high temperatures {≥120 °C [≥248 °F]} are restricted to a region with < 10 m [~ 33 ft] of the emplacement drifts (Figure 3-5). Fedors, et al. (2003) confirm the time-limited nature of the thermal pulse and, in the absence of backfill, show drift-wall temperatures drop below approximately 130 °C [~266 °F] within approximately 100–200 years.

3.10 Limitations of Previous Work with Regard to Dike Propagation

Although some previous studies indicate modification of principal stresses can occur, these studies do not provide sufficient information to assess the effects of material nonhomogeneity on the tendency for this alteration of the stress tensor. In fact, the stress histories in Ofoegbu (2001) suggest the tendency for principal stress directions to change likely decreases with rock-

mass stiffness. Also, these studies presume a perfect lateral constraint that may not be justified considering the variable surface topography of the Yucca Mountain region.

Previous thermal analyses, with the exception of the HEFF models of Mack, et al. (1989), employed zero-displacement conditions along the vertical boundaries. Ofoegbu (2000, 1999) addresses this condition and shows the stress state that develops is unaffected by the choice of boundary condition. As Figures 3-2 and 3-5 show, the dominant stress and temperature changes are restricted to the region around the emplacement drifts. Hardy and Bauer (1992, 1991), however, do not discuss this condition, and it is unclear from their reports how the zero-displacement condition influences the analysis results.

The final drift layout and waste emplacement design for the potential repository are not yet established, and many previous studies employed geometries, heat loads, or both that are inconsistent with the currently expected configuration (Board, et al., 2002; DOE, 2002). Also, the potential effects of preclosure ventilation were not addressed.

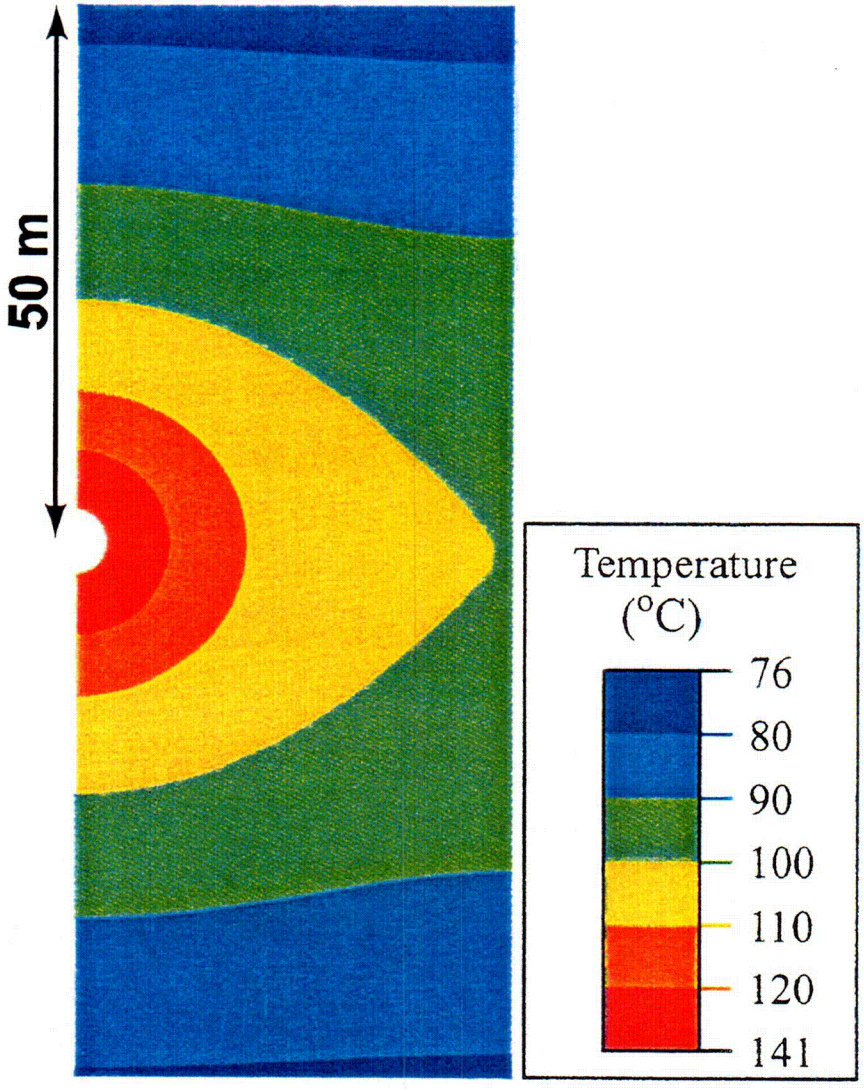

Figure 3-5. Temperature distribution for drift-scale thermomechanical model 150 years after waste emplacement (from Ofoegbu, 2000). NOTE: Information is provided in °C, for conversion, use 1.8 × °C + 32 = °F.

C05

4 ANALYTICAL APPROACH

Although a simple elastic analysis is insufficient for this problem, beginning at this level leads to a more tractable problem. As such, the key relationships that relate thermal stress and strain are first summarized. This summary is followed by a description of cases where closed-form analytical solutions exist (always with an emphasis on the inherent assumptions and limitations). Finally, an alternative is offered that is a more realistic representation of the geology of Yucca Mountain and is also simple enough to allow an analytical evaluation. Based on the results, suggestions are offered on how best to evaluate previous research results and conclusions and also where future analyses should be focused.

4.1 Thermal Stress Versus Strain

For an isotropic, homogeneous, and elastic material, the total strain (ε_{ij}) is given by

$$\varepsilon_{ij} = \varepsilon_{ij}^{E} + \varepsilon_{ij}^{T} \tag{4-1}$$

where ε_{ij}^{E} is the elastic strain, and ε_{ij}^{T} is the thermal strain (e.g., Jaeger and Cook, 1979; Turcotte and Schubert, 1982; Ranalli, 1987). For linear elastic materials, ε_{ij}^{E} is given by

$$\varepsilon_{ij}^{E} = \frac{1+\nu}{E}\sigma_{ij} - \frac{\nu}{E}\sigma_{kk}\delta_{ij} \tag{4-2}$$

where E is Young's Modulus (Pa), ν is Poisson's Ratio, and δ_{ij} is the Kronecker delta. The thermal strain (ε_{ij}^{T}) is given by

$$\varepsilon_{ij}^{T} = \alpha_{L}\Delta T\delta_{ij} \tag{4-3}$$

where α_L is the coefficient of linear thermal expansivity (10^{-5} K^{-1}) and ΔT (K) is the change in temperature. Substituting Eqs. (4-2) and (4-3) into Eq. (4-1), gives an expression for the total strain

$$\varepsilon_{ij} = \frac{1+\nu}{E}\sigma_{ij} - \frac{\nu}{E}\sigma_{kk}\delta_{ij} + \alpha_{L}\Delta T\delta_{ij} \tag{4-4}$$

As principal strains, Eq. (4-4) expands to

$$\begin{aligned}
\varepsilon_1 &= \frac{1+\nu}{E}\sigma_1 - \frac{\nu}{E}(\sigma_1+\sigma_2+\sigma_3) + \alpha_L\Delta T \\
\varepsilon_2 &= \frac{1+\nu}{E}\sigma_2 - \frac{\nu}{E}(\sigma_1+\sigma_2+\sigma_3) + \alpha_L\Delta T \\
\varepsilon_3 &= \frac{1+\nu}{E}\sigma_3 - \frac{\nu}{E}(\sigma_1+\sigma_2+\sigma_3) + \alpha_L\Delta T
\end{aligned} \tag{4-5}$$

From linear elasticity (Turcotte and Schubert, 1982), the total stress (Pa) (σ_{ij}) can be written as the sum of the elastic and thermal stress components:

$$\sigma_{ij} = \sigma_{ij}^{E} + \sigma_{ij}^{T} \tag{4-6}$$

which can be expanded for a linear elastic material to

$$\sigma_{ij} = \lambda \varepsilon_{kk} \delta_{ij} + 2\mu\varepsilon_{ij} - \alpha_L (3\lambda + 2\mu)\Delta T \delta_{ij} \tag{4-7}$$

where $\lambda_{(Pa)} = \frac{E\nu}{(1+\nu)(1-2\nu)}$ and $\mu_{(Pa)} = \frac{E}{2(1+\nu)}$

As principal stresses, Eq. (4-7) gives

$$\begin{aligned}
\sigma_1 &= \lambda(\varepsilon_1 + \varepsilon_2 + \varepsilon_3) + 2\mu\varepsilon_1 - \alpha_L(3\lambda + 2\mu)\Delta T \\
\sigma_2 &= \lambda(\varepsilon_1 + \varepsilon_2 + \varepsilon_3) + 2\mu\varepsilon_2 - \alpha_L(3\lambda + 2\mu)\Delta T \\
\sigma_3 &= \lambda(\varepsilon_1 + \varepsilon_2 + \varepsilon_3) + 2\mu\varepsilon_3 - \alpha_L(3\lambda + 2\mu)\Delta T
\end{aligned} \tag{4-8}$$

These equations are derived for the sign convention where negative stresses are compressional, and positive strains are extensional.

4.2 Completely Constrained System

A system fully constrained in all directions with a uniform temperature change and homogeneous material properties provides a useful end-member behavior, although it is unrealistic from a geologic standpoint. For this case, a thermal load cannot be relieved via any thermal strain (i.e., $\varepsilon_1^T = \varepsilon_2^T = \varepsilon_3^T = 0$), and, therefore, the maximum increase in thermal stress will occur, given by

$$\sigma_1^T = \sigma_2^T = \sigma_3^T = -\alpha_L(3\lambda + 2\mu)\Delta T \tag{4-9}$$

Thermal loading modifies the stress state from the *in-situ* values, but only for absolute magnitudes. The principal stress ratios and directions will not change.

4.3 Completely Unconstrained System

As with the fully constrained system, a completely unconstrained system also is physically and geologically unrealistic. It does, however, provide a useful end-member behavior because the thermal load can be accommodated by strain in the body. This system then provides an upper bound for thermal strain given by

$$\varepsilon_{max}^T = \varepsilon_1^T = \varepsilon_2^T = \varepsilon_3^T = \alpha_L \Delta T \tag{4-10}$$

The net result is a stress state unaffected by the temperature change.

4.4 Horizontally Constrained but Vertically Unconstrained System

The configuration with a nonuniform temperature field has been most often applied to the problem of thermal stress analysis of the potential repository at Yucca Mountain. This is a reasonable first-level assumption, because shallow subsurface rocks (assuming a flat surface topography) are under greater horizontal constraint than vertical constraint because the ground surface is free to displace upward. Mathematically, this system is defined as $\varepsilon_H^T = \varepsilon_h^T = 0$. Substitution of this boundary condition into Eq. (4-5) yields a description of the thermal strain:

$$\begin{aligned} \varepsilon_V^T &= -\frac{\nu}{E}(\sigma_H + \sigma_h) + \alpha_L \Delta T \\ \varepsilon_H^T &= \varepsilon_h^T = 0 \end{aligned} \tag{4-11}$$

This system produces the maximum increase in horizontal stress magnitude and quickly results in both horizontal stresses exceeding the vertical stress (i.e., σ_v becomes σ_3) when applied to the Yucca Mountain *in-situ* stress state.

4.5 System with Differing Horizontal and Vertical Stiffness

A more general case is now developed that is intermediate to the first two systems, but is more geologically realistic than the third system. Rather than assuming the rock volume is either fully constrained or completely unconstrained in a given orientation, an attempt is made to quantify the level of stiffness from the recently completed fracture characterization studies. For this initial analysis, only the potential strain accommodated via closure of preexisting fractures is considered. The stress/strain equations are developed in a general form such that the magnitude of joint-closure strain (ε_{ij}^J) available to accommodate the thermal load is specified. For $\varepsilon_{ij}^J = 0$, no thermal strain is absorbed by joint closure, and the resulting thermal stress increase is at maximum (reverts to the fully constrained system). At the other extreme, a rock with sufficient fractures may act as effectively unconstrained with the result that no thermal stress is produced. Recognizing that neither extreme is reasonable, the goal is to assess situations that are intermediate and geologically realistic.

For this case, the magnitude of thermal strain is reduced to

$$\varepsilon_{ij}^T = \alpha_L \Delta T \delta_{ij} - \varepsilon_{ij}^J \tag{4-12}$$

and, therefore, a revised estimate of the total thermal strain is given by

$$\varepsilon_{ij}^T = \frac{1+\nu}{E}\sigma_{ij} - \frac{\nu}{E}\sigma_{kk}\delta_{ij} + \alpha_L \Delta T \delta_{ij} - \varepsilon_{ij}^J \tag{4-13}$$

By quantifying joint strains, these relationships can be used to assess how joints of a given orientation affect the thermal stress field.

4.6 Joint Closure Strain and Thermal Stress

To simplify the analysis, only the subset of total strain taken up by joint closure is considered. Because deformation that takes place via other mechanisms (e.g., slip on existing fractures or formation of new fractures) is not explicitly considered, the strain estimate is a lower bound on the potential strain accommodation during thermal loading.

An estimate of the primary fracture orientations and their respective intensities and current apertures is needed to estimate the potential joint closure strain. Because it is highly unlikely the fractures will close completely, given the presence of irregular surfaces caused by asperities (Bandis, et al., 1983; U.S. National Committee for Rock Mechanics, 1996), the fraction of measured aperture that can be closed (i.e., effective aperture) is estimated. The fracture intensity multiplied by the effective aperture for the length of the available rock provides the magnitude of the joint closure strain. These quantifications of joint strain can be used to evaluate how joint orientation tends to affect the modification of the thermal stress field.

In the following sections, the available fracture data for the Yucca Mountain area are summarized, estimates of effective aperture and the corresponding magnitudes of joint closure strain are discussed, and these are applied to evaluation of the stress-state modification caused by thermal loading.

5 YUCCA MOUNTAIN FRACTURE DATA

5.1 Overview

This chapter discusses and synthesizes the available fracture data for the Yucca Mountain region. Fracture data collected in support of characterization analyses of Yucca Mountain are numerous and varied. Data have been collected on surface exposures, in exploratory boreholes, and in tunnels and alcoves of the Exploratory Studies Facility and Enhanced Characterization of the Repository Block Cross Drift using a variety of techniques that include detailed line surveys and full-periphery geologic mapping. A complete synthesis/evaluation of all fracture data is beyond the scope of this analysis, so this report is restricted to the data collected in the potential repository host horizons as evaluated in the Exploratory Studies Facility and Enhanced Characterization of the Repository Block. The primary data sources are Brechtel, et al. (1995); Barr, et al. (1996); Albin, et al. (1997); Kicker, et al. (1997); Mongano, et al. (1999); and numerous digital data sets (listed in Table 5-1). Summaries of fracture data also are available in synthesized form from Sweetkind and Williams-Stroud (1996), CRWMS M&O (2000b), and Nieder-Westermann (2000). Synthesis and calculations performed for this report are documented in Center for Nuclear Waste Regulatory Analyses (CNWRA) Scientific Notebook 606E.

Fracture data from the Exploratory Studies Facility and Enhanced Characterization of the Repository Block were collected primarily in the four potential repository host horizons in the Miocene Topopah Springs Tuff:

- Upper lithophysal zone—Tptpul
- Middle nonlithophysal zone—Tptpmn
- Lower lithophysal zone—Tptpll
- Lower nonlithophysal zone—Tptpln

The north-south-trending Exploratory Studies Facility main drift exposes only Tptpmn, whereas the generally northeast-southwest-trending Enhanced Characterization of the Repository Block Cross Drift provides data for all repository host horizons. Because lithologic character (i.e., degree of welding and presence/absence of lithophysal cavities) was expected to be a significant control on fracturing, the analyses were divided by the stratigraphic unit. Fracture orientations were classified into sets on the basis of observation of multiple modes using different statistical software—*CLUSTRAN* for the Exploratory Studies Facility main drift (Albin, et al., 1997) and *DIPS* for the Enhanced Characterization of the Repository Block (Mongano, et al. 1999). Different tracelength lower cutoffs were used at different times during the history of data collection. For example, an initial cutoff of 30 cm [11.8 in] was employed from stations 28+00 through 37+80 in the Exploratory Studies Facility main drift. This cutoff was increased to 1 m [3.28 ft] for stations 37+80 throush 55+00 {except for 50-m [164-ft]segments between stations 45+00 through 45+50 and 50+00 through 50+50 where the cutoff reverted to 30 cm [11.8 in]}.

Because the majority of the potential repository is currently planned to occupy the lower lithophysal (~72 percent) and middle nonlithophysal (~20 percent) units (Board, et al., 2002; DOE, 2002), this analysis is restricted to those two intervals.

Table 5-1. Document Tracking Numbers for Fracture Data Collected in the Exploratory Studies Facility and the Enhanced Characterization of the Repository Block Cross Drift by Either Detailed Line Survey or Full-periphery Geologic Mapping. Complete Citations Are Provided in the Source Data Section.	
DTN*	**Survey Location**
GS960708314224.010	Main Drift, ESF†—Stations 40+00 through 45+00
GS960908314224.014	Main Drift, ESF—Stations 50+00 through 55+00
GS970208314224.003	South Ramp, ESF—Stations 60+00 through 65+00
GS970808314224.008	South Ramp, ESF—Stations 65+00 through 70+00
GS970808314224.010	South Ramp, ESF—Stations 70+00 through 75+00
GS970808314224.012	South Ramp, ESF—Stations 75+00 through 78+77
GS971108314224.020	North Ramp, ESF—Stations 0+60 through 4+00
GS971108314224.021	North Ramp, ESF—Stations 4+00 through 8+00
GS971108314224.022	North Ramp, ESF—Stations 8+00 through 10+00
GS971108314224.023	North Ramp, ESF—Stations 10+00 through 18+00
GS971108314224.024	North Ramp, ESF—Stations 18+00 through 26+00
GS971108314224.025	North Ramp, ESF—Stations 26+00 through 30+00
GS971108314224.026	Main Drift, ESF—Stations 45+00 through 50+00
GS971108314224.028	South Ramp, ESF—Stations 55+00.18 through 59+99.95
GS990408314224.001	ECRB‡ Cross Drift—Stations 00+00.89 to 14+95.18
GS990408314224.002	ECRB Cross Drift—Stations 15+00.85 to 26+63.8
GS000608314224.004	Main Drift, ESF—Stations 35+00 through 40+00

*DTN—Document Tracking Numbers
†ESF—Exploratory Studies Facility
‡ECRB—Enhanced Characterization of the Repository Block

5.2 Fracture Data—Middle Nonlithophysal Unit in Exploratory Studies Facility

Albin, et al. (1997) defined five fracture sets (sets 1–4 plus random) for the entire middle nonlithophysal unit based on measurements in the Exploratory Studies Facility main drift:

- Set 1: ~120°/80°—dominant set, found everywhere
- Set 2: ~220°/80°
- Set 3: ~310°/30°—absent from stations 42+00 through 50+00
- Set 4: ~270-330°/40-60°—only found between stations 28+00 through 37+00
- Random–especially prevalent from stations 28+00 through 42+00

The Exploratory Studies Facility main drift trends approximately 183°, and, as such, the sampling is biased against all fractures with strikes within ~15–20° of 183° (or 003°). Albin, et al. (1997) group their data into four structural domains (domain 1 = stations 28+00 through 37+00, domain 2 = stations 37+00 through 42+00, domain 3 = stations 42+00 through 51+50, also referred to as the intensely fractured zone, domain 4 = stations 51+50 through 55+00). The structural domains are defined by the presence or absence of fracture sets, changes in fracture distribution and density, or changes in the relative number of fractures per set.

The detailed line survey fracture data for the Tptpmn interval in the Exploratory Studies Facility were compiled into a single Microsoft® Excel spreadsheet (details provided in CNWRA Scientific Notebook 606E). The fracture intensity for each domain (Table 5-2) was calculated using the median fracture spacing after application of a correction for tunnel orientation (Terzaghi, 1965). Intensity also was determined for fractures from sets 1 to 4 (as determined by Albin, et al.,1997) within each domain. The most prominent set (set 1) has median intensities of 2.58, 2.75, 8.87, and 3.01 m^{-1} [0.79, 0.84, 2.70, 0.92 ft^{-1}] for domains 1 to 4, which mimics the result for all fractures. The other steeply dipping fracture set (set 2) has median intensities of 2.42, 1.84, 1.32, and 1.19 m^{-1} [0.74, 0.56, 0.40, 0.36 ft^{-1}] for domains 1 to 4. The shallow fractures (set 3) have median intensities of 1.39, 1.88, 1.35, and 3.69 m^{-1} [0.42, 0.57, 0.41, 1.12 ft^{-1}] for domains 1 to 4. Estimates of average fracture aperture are quite variable, mostly with respect to fracture set and, to a lesser degree, domain (Table 5-2). The mean maximum aperture based on all fractures is similar for domains 1, 2, and 3 {0.3 to 0.5 mm [0.01 to 0.02 in]}, but is more than twice as high for domain 4 {1.37 mm [0.05 in]}. Set 1 fractures are narrow in domain 1 {0.18 mm [0.007 in]}, have an intermediate aperture in domains 2 and 3 {0.47 and 0.39 mm [0.019 and 0.015 in]}, and are most open in domain 4 {1.17 mm [0.046 in]}. Set 2 fractures have apertures 2–3 times those of set 1 for each domain. Set 3 fractures, in contrast, are widest in domain 1 and nearly closed in the other domains.

As noted previously, portions of the main drift detailed line survey data (primarily stations 28+00 through 37+80) were collected with a lower tracelength cutoff of 30 cm [11.8 in] rather than the subsequent cutoff of 1 m [3.28 ft]. This difference in sampling technique primarily affects domain 1 (i.e., stations 28+00 through 37+00). Of the 2,774 fractures recorded for this interval, 1,022 (37 percent) had total tracelengths of <1 m [3.28 ft]. Partitioning of the domain 1 data into

Table 5-2. Summary of Median Fracture Intensity (m^{-1})* and Mean Maximum Aperture (mm)† for the Middle Nonlithophysal Interval of the Topopah Spring Tuff in the Exploratory Studies Facility Main Drift

Category‡	Domain 1§		Domain 2‖		Domain 3¶		Domain 4#	
	Intensity	Aperture	Intensity	Aperture	Intensity	Aperture	Intensity	Aperture
All	NA	0.33	NA	0.48	NA	0.49	NA	1.37
Set 1	2.58	0.18	2.75	0.47	8.87	0.39	3.01	1.17
Set 2	2.42	0.63	1.84	1.01	1.32	0.94	1.19	2.28
Set 3	1.39	0.88	1.88	0.05	1.35	0.18	3.69	0
Set 4	0.19	0.54	NA	NA	NA	NA	NA	NA
Random	NA	0.27	NA	0.25	NA	0.75	NA	1.19

*NOTE: Information presented in m^{-1}; for conversion to ft^{-1}, use 1 m^{-1} = 0.3048 ft^{-1}.
†NOTE: Information presented in mm; for conversion to in, use 1 mm = 0.0394 in.
‡NOTE: Intensity does not apply to either the All or Random fracture groups because intensity measurements are based on true fracture spacing (i.e., corrected for orientation sampling bias for each set orientation). Set 4 fractures are only present in domain 1. Set selection criteria (Albin, et al., 1997) are:
§Domain 1: set 1 = strike of 082 through 132° (or 262 through 312°) and dips >70°; set 2 = strike of 015 through 045° (or 195 through 245°) and dips >70°; set 3 = strike of 102 through 170° (or 282 through 350°) and dips <40°; set 4 = strike of 100 through 140° (or 280 through 320°) and dips 40 through 60°; and random = all others.
‖Domain 2: set 1 = strike of 100 through 140° (or 280 through 320°) and dips >70°; set 2 = strike of 020 through 062° (or 200 through 242°) and dips >70°; set 3 = strike of 110 through 170° (or 290 through 350°) and dips <40°; and random = all others.
¶Domain 3: set 1 = strike of 100 through 145° (or 280 through 325°) and dips >70°; set 2 = strike of 020 through 070° (or 200 through 250°) and dips >70°; set 3 = strike of 115 through 165° (or 295 through 345°) and dips <40°; and random = all others.
Domain 4: set 1 = strike of 120 through 150° (or 300 through 330°) and dips >70°; set 2 = strike of 035 through 085° (or 215 through 265°) and dips >70°; set 3 = strike of 125 through 175° (or 305 through 355°) and dips <35°; and random = all others.

subsets based on tracelength {<1m [3.28 ft] and ≥1 m [3.28 ft]} reveals several trends (Table 5-3). For the short tracelength subset, 41 percent of the fractures fall into the random category compared with 34 percent in set 1. In contrast, the long tracelength subset has 29 percent random and 46 percent in set 1. For all but the set 4 fractures, the median fracture intensity is greater for the smaller tracelength subset for a given fracture set {1.90 versus 1.62 m^{-1} [0.58 versus 0.49 ft^{-1}] for set 1, 1.88 vs. 1.09 m^{-1} [0.57 versus 0.33 ft^{-1}] for set 2, 0.90 versus 0.76 m^{-1} [0.27 versus 0.23 ft^{-1}] for set 3, and 0.06 versus 0.16 m^{-1} [0.02 versus 0.05 ft^{-1}] for set 4}. The short tracelength subset shows consistently smaller mean maximum aperture values {e.g., 0.22 versus 0.40 mm [0.0087 versus 0.016 in] for the entire domain, 0.13 versus 0.20 mm [0.0051 versus 0.0079 in] for set 1, 0.30 versus 0.88 mm [0.012 versus 0.035 in] for set 2, 0.75 versus 0.95 mm [0.030 vs. 0.037 in] for set 3, and 0.09 versus 0.61 mm [0.0035 versus 0.024 in] for set 4}.

Table 5-3. Summary of Number/Percentage, Median Fracture Intensity (m^{-1})*, and Mean Maximum Aperture (mm)† for the Tptpmn Interval in the Exploratory Studies Facility Main Drift for Domain 1. Data Are Partitioned by Tracelength {<1 m [3.28 ft] Versus ≥1 m [3.28 ft]}.						
Category	Tracelength <1 m [3.28 ft]			Tracelength ≥1 m [3.28 ft]		
	Number/%	Intensity	Aperture	Number / %	Intensity	Aperture
All‡	1022/37	NA	0.22	1752 / 63	NA	0.4
Set 1	344/34	1.9	0.13	814 / 46	1.62	0.2
Set 2	198/19	1.88	0.3	257 / 15	1.09	0.88
Set 3	55/5	0.9	0.75	107 / 6	0.76	0.95
Set 4	11/1	0.06	0.09	74 / 4	0.16	0.61
Random	414/41	NA	0.19	500 / 29	NA	0.33
*NOTE: Information presented in m^{-1}; for conversion to ft^{-1}, use 1 m^{-1} = 0.3048 ft^{-1}. †NOTE: Information presented in mm; for converstion to in, use 1 mm = 0.0394 in. ‡Intensity does not apply to the All category because intensity measurements are based on true fracture spacing.						

5.3 Fracture Data—Middle Nonlithophysal Unit in Enhanced Characterization of the Repository Block

Mongano, et al. (1999) summarize the fracture data collected in the Enhanced Characterization of the Repository Block Cross Drift, and they recognize the presence of three fracture sets in the middle nonlithophysal interval (total of 930 fractures measured). Two sets are steeply dipping (set 1 = 122°/84° and set 2 = 195°/85°) and the third is subhorizontal (306°/09°). Mongano, et al. suggest their sets 1, 2, and 3 correspond to the Exploratory Studies Facility sets 1, 2, and 3 [as determined by Albin, et al. (1997)], although the average orientations do differ.

Mongano, et al. (1999) report *CLUSTRAN* analyses that give three sets for the 930 fractures (~63 percent set 1 fractures, ~31 percent set 2 fractures, and ~6 percent set 3 fractures), which requires broad windows for sets 1 and 2 to catch outliers (i.e., avoid a random category). The issue is complicated because Mongano, et al. never explicitly list the window criteria (i.e., the range for strike azimuths or dip angles). In a subsequent summary report, Nieder-Westermann (2000) presents selection criteria for Tptpmn that result in 50 percent of the fractures (461 of 930) being assigned to the random category. With the Nieder-Westermann selection criteria, there are 32 percent set 1 fractures, 13 percent set 2 fractures, and 6 percent set 3 fractures. According to Nieder-Westermann, the average orientations for joint sets 1 through 3 are 131°/84°, 209°/83°, and 329°/09°.

Given the various reports, it is difficult to generalize the results of fracture intensity, maximum aperture, or tracelength as a function of fracture set because it is unclear whose set criteria are more valid. As a compromise, results using both the Mongano, et al. (1999) and the Nieder-Westermann (2000) criteria (Tables 5-4 and 5-5) are compared. The mean maximum aperture is 1.69 mm [0.0665 in] for the entire Tptpmn interval in the Enhanced Characterization of the Repository Block.

Table 5-4. Summary of the Detailed Line Survey Fracture Data for Tptpmn Interval in the Enhanced Characterization of the Repository Block with Set Selection Based on Mongano, et al.* Criteria. A Total of 930 Discontinuities Were Recorded and All Were Partitioned into One of the Three Sets.†

Category	Number/%	Intensity	Aperture
All‡	930/100	NA	1.69 [0.0665 in]
Set 1	584/63	1.66 [0.506 ft^{-1}]	0.81 [0.032 in]
Set 2	293/32	1.81 [0.552 ft^{-1}]	3.72 [0.146 in]
Set 3	53/6	1.48 [0.451 ft^{-1}]	0.25 [0.0098 in]

*Mongano, G.S., W.L. Singleton, T.C. Moyer, S.C. Beason, G.L.W. Eatman, A.L. Albin, and R.C. Lung. "Geology of the ECRB Cross Drift–Exploratory Studies Facility, Yucca Mountain Project, Yucca Mountain, Nevada." SPG42GM3. Denver, Colorado: U.S. Geological Survey. 1999. (Estimated from their figures because criteria are not explicitly stated in the report).
†Median Fracture Intensity Is in Units of m^{-1} [ft^{-1}], While Mean Maximum Aperture Is in Units of mm [in].
‡Intensity does not apply to the All category. Set selection criteria are (i) set 1 = strike of 069 to 159° (or 248 to 338°) and dips >30°, (ii) set 2 = strike of 339 to 068° (or 160 to 248°) and dips >30°, and (iii) set 3 = all dips ≤30°.

Table 5-5. Summary of the Detailed Line Survey Fracture Data for Tptpmn Interval in the Enhanced Characterization of the Repository Block with Set Selection Based on Nieder-Westermann* Criteria. A Total of 930 Discontinuities Were Recorded, of Which 50 Percent Fall into the Random Category.†

Category	Number/%	Intensity	Aperture
All‡	930/100	NA	1.69 [0.0665 in]
Set 1	296/32	1.43 [0.436 ft^{-1}]	0.99 [0.0390 in]
Set 2	120/13	1.37 [0.418 ft^{-1}]	6.19 [0.244 in]
Set 3	53/6	1.46 [0.445 ft^{-1}]	0.25 [0.0098 in]
Random	461/50	2.37 [0.722 ft^{-1}]	1.15 [0.0453 in]

*Nieder-Westermann, G.H. "Fracture Geometry Analysis for the Stratigraphic Units of the Repository Host Horizon." ANL–EBS–GE–000006. Rev. 00. Las Vegas, Nevada: CRWMS M&O. 2000.
†Median Fracture Intensity Is in Units of m^{-1} [ft^{-1}], While Mean Maximum Aperture Is in Units of mm [in].
‡Intensity does not apply to the All category. Set selection criteria are (i) set 1 = strike of 114 through 148° (or 294 through 328°) and dips ≥70°, (ii) set 2 = strike of 014 through 044° (or 194 through 224°) and dips ≥70°, (iii) set 3 = all dips ≤30°; and (iv) random = all others.

Comparison of the data demonstrates median intensity for both sets 1 and 2 are reduced by using the Nieder-Westermann (2000) criteria. The decrease is most significant for the set 2 fractures (nearly 54-percent reduction). Mean maximum aperture with the Nieder-Westermann criteria displays a slight increase for set 1 (~10 percent), whereas the aperture value for set 2 increases by 40 percent. Although the original Mongano, et al. (1999) report never explicitly presents a summary of mean spacing or tracelength data, Board (2003) provides a table (Table 2, p. 3-7) that is attributed to Mongano, et al. (1999). According to Board (2003), the mean spacing for sets 1 through 3 are 0.5, 1.48, and 4.2 m [1.64, 4.86, and 13.8 ft]. These values are uncorrected for the scanline-orientation sampling bias and correspond to mean intensities of 2.0, 0.68, and 0.24 m^{-1} [0.61, 0.21, and 0.073 ft^{-1}].

The corresponding mean intensity values for corrected spacings calculated from the spreadsheet of the detailed line survey data set using the Mongano, et al. (1999) criteria (same as applied for Table 5-4) are 1.15, 1.14, and 1.01 m^{-1} [0.35, 0.35, and 0.31 ft^{-1}] for sets 1 through 3.

5.4 Fracture Data—Lower Lithophysal Unit

The Exploratory Studies Facility tunnel traverses only a small portion of the Tptpll interval (from stations 57+29 through 58+78 in the south ramp) and, therefore, only encounters a small number of discontinuities (n = 38). The overall mean maximum aperture is 4.21 mm [0.166 in] for the Tptpll interval in the Exploratory Studies Facility. Of the 38 fractures, 23 (61 percent) are assigned to set 1 yielding a median intensity (based on true spacing) of 0.61 m^{-1} [0.19 ft^{-1}] and a mean maximum aperture of 5.22 mm [0.206 in]. Two fractures fall into set 2 (5 percent) yielding a (statistically insignificant) median intensity of 0.74 m^{-1} [0.23 ft^{-1}] and a mean maximum aperture of 2.50 mm [0.0984 in]. None of the measured fractures fall into set 3 (the gently dipping fractures). The remaining random fractures (n = 13 or 34 percent) have a median intensity of 0.44 m^{-1} [0.13 ft^{-1}] and a mean maximum aperture of 2.69 mm [0.106 in].

Sampling the Tptpll interval was somewhat better in the Enhanced Characterization of the Repository Block where the unit is present from stations 14+44 through 23+26. Fracture data for the Tptpll horizon in the Enhanced Characterization of the Repository Block (Tables 5-6 and 5-7) also are analyzed using the fracture set selection criteria of Mongano, et al. (1999) and Nieder-Westermann (2000). Mongano, et al. (1999) recognize four different fracture sets in the Tptpll interval with *CLUSTRAN* mean orientations of 157°/80° (set 1), 032°/84° (set 2), 340°/06° (set 3), and 097°/84° and 070°/85° (set 4). As with the Tptpmn interval, Mongano, et al. do not state explicitly the windows for their criteria, so these were estimated from the data plots (Mongano, et al., 1999, Figures 10 and 11). Based on the Mongano, et al. criteria, 198 (73 percent) of the 300 discontinuities were assigned to set 1, 8 (3 percent) were assigned to set 2, 20 (7 percent) were assigned to set 3, and the remaining 54 (18 percent) assigned to set 4. Nieder-Westermann (2000) recognizes three fracture sets plus a random category for the Tptpll interval, however, the criteria are not identical to those used for the Tptpmn interval (and different from those of Mongano, et al., 1999). The Nieder-Westermann (2000) criteria result in 86 (29 percent) of the 300 discontinuities in set 1 (average orientation 145°/82°), 65 (22 percent) in set 2 (average orientation 180°/79°), 19 (6 percent) in set 3 (average orientation 315°/05°), and the remaining 130 (44 percent) assigned to the random category.

Table 5-6. Summary of the Detailed Line Survey Fracture Data for Lower Lithophysal Interval in the Enhanced Characterization of the Repository Block with Set Selection Based on Mongano, et al.* Criteria.†

Category	Number/%	Intensity	Aperture
All‡	300/100	NA	3.12 [0.123 in]
Set 1	218/73	0.64 [0.20 ft^{-1}]	3.54 [0.139 in]
Set 2	8/3	0.08 [0.024 ft^{-1}]	5.75 [0.226 in]
Set 3	20/7	1.52 [0.46 ft^{-1}]	0.45 [0.0177 in]
Set 4	54/18	0.22 [0.067 ft^{-1}]	2.04 [0.0803 in]

*Mongano, G.S., W.L. Singleton, T.C. Moyer, S.C. Beason, G.L.W. Eatman, A.L. Albin, and R.C. Lung. "Geology of the ECRB Cross Drift—Exploratory Studies Facility, Yucca Mountain Project, Yucca Mountain, Nevada." SPG42GM3. Denver, Colorado: U.S. Geological Survey. 1999. (Estimated from their figures because criteria are not explicitly stated in the report).
†Median Fracture Intensity Is in Units of m^{-1} [ft^{-1}], While Mean Maximum Aperture Is in Units of mm [in].
‡Intensity does not apply to the All category. Set selection criteria are (i) set 1 = strike of 118 through 210° (or 301 through 020°) and dips >40°, (ii) set 2 = strike of 021 through 050° (or 190 through 230°) and dips >40°, (iii) set 3 = all dips ≤40°, and (iv) set 4 = strike of 051 through 117° (or 231 through 300°) and dips >40°.

Table 5-7. Summary of the Detailed Line Survey Fracture Data for Tptpll Interval in the Enhanced Characterization of the Repository Block with Set Selection Based on Nieder-Westermann* Criteria. A Total of 300 Discontinuities Were Recorded, of Which 43 Percent Fall into the Random Category.†

Category	Number/%	Intensity	Aperture
All‡	300/100	NA	3.12 [0.123 in]
Set 1	86/29	0.52 [0.16 ft^{-1}]	2.24 [0.0882 in]
Set 2	65/22	0.26 [0.079 ft^{-1}]	3.57 [0.141 in]
Set 3	19/6	2.02 [0.62 ft^{-1}]	0.47 [0.0185 in]
Random	130/43	0.48 [0.15 ft^{-1}]	3.87 [0.152 in]

*Nieder-Westermann, G.H. "Fracture Geometry Analysis for the Stratigraphic Units of the Repository Host Horizon." ANL–EBS–GE–000006. Rev. 00. Las Vegas, Nevada: CRWMS M&O. 2000.
†Median Fracture Intensity Is in Units of m^{-1} [ft^{-1}], While Mean Maximum Aperture Is in Units of mm [in].
‡Intensity does not apply to the All category. Set selection criteria are (i) set 1 = strike of 129 through 161° (or 311 through 339°) and dips ≥70°, (ii) set 2 = strike of 345 through 015° (or 165 through 195°) and dips ≥70°, (iii) set 3 = all dips ≤30°, and (iv) random = all others.

As Tables 5-6 and 5-7 illustrate, the lack of a random category in the Mongano, et al. (1999) selection criteria leads to a significantly greater number of fractures (218 of 300) being assigned to set 1 compared with the Nieder-Westermann (2000) criteria. Also, set 2 fractures are eight times more prevalent with the Nieder-Westermann criteria.

In addition to the fracture orientation and estimates of intensity and aperture, some joint closure models (e.g., Bandis, et al., 1983; Barton, et al., 1985) require additional variables (e.g., joint roughness coefficient), empirically derived constants, or both. Where available, estimates for these parameters are used for the repository host horizon. Where unavailable, values from the literature are used (e.g., Hsiung, et al., 1994). A synopsis of the key fracture parameters is provided in Table 5-8.

Table 5-8. Summary of Fracture Parameters for Tptpmn and Tptpll Intervals in the Enhanced Characterization of the Repository Block					
		Mongano, et al.*		Nieder-Westermann†	
Fracture Parameter		Tptpmn	Tptpll	Tptpmn	Tptpll
Intensity‡ (m^{-1})	Set 1	1.66	0.61	1.4	0.5
	Set 2	1.81	0.09	0.84	0.21
	Set 3	1.48	1.52	1.48	0.15
Aperture§ (mm)	Set 1	0.81	3.73	0.99	2.24
	Set 2	3.72	5.67	6.19	3.57
	Set 3	0.25	0.45	0.25	0.47
Joint Roughness Coefficient	Set 1	9.62	11.86	9.75	11.1
	Set 2	9.52	16.22	9.51	12.26
	Set 3	14.11	16	14.11	16.42
Median Total Tracelength‖ (m)	Set 1	2.13	1.7	2.25	1.65
	Set 2	1.75	2.50	1.7	1.7
	Set 3	3.45	3.81	3.45	3.42

*Mongano, G.S., W.L. Singleton, T.C. Moyer, S.C. Beason, G.L.W. Eatman, A.L. Albin, and R.C. Lung. "Geology of the ECRB Cross Drift—Exploratory Studies Facility, Yucca Mountain Project, Yucca Mountain, Nevada." SPG42GM3. Denver, Colorado: U.S. Geological Survey. 1999.
†Nieder-Westermann, G.H. "Fracture Geometry Analysis for the Stratigraphic Units of the Repository Host Horizon." ANL–EBS–GE–000006. Rev. 00. Las Vegas, Nevada: CRWMS M&O. 2000.
‡NOTE: Information presented in m^{-1}; for conversion to ft^{-1}, use 1 m^{-1} = 0.3048 ft^{-1}.
§NOTE: Information presented in mm; for conversion to in, use 1 mm =0.0394 in.
‖NOTE: Information presented in m; for conversion to ft, use 1 m = 3.281 ft.

The detailed line survey data record a fracture roughness measurement that employs the U.S. Bureau of Reclamation roughness coefficient scale, which varies from R1 (very rough) to R6 (very smooth). Sweetkind and Williams-Stroud (1996, p. 31) provide a table that gives a general correlation between the Bureau of Reclamation's coefficient and the joint roughness coefficient. Although an exact match is not provided (e.g., R1 >20, R2 = 16–20, R3 = 10–16, R4 = 6–10, R5 = 2–6, and R6 = 0–2), each detailed line survey roughness coefficient is converted into an equivalent joint roughness coefficient by assigning joint roughness coefficient values that were at or near the midway point of each range (i.e., R1 = 22, R2 = 18, R3 = 13, R4 = 8, R5 = 4, and R6 = 1). As a general rule, the subhorizontal (set 3) fractures display higher joint roughness coefficient values than do the more steeply dipping fractures.

5.5 Fracture Data Summary

Because a range of fracture orientations is given by previous workers, the average of the results is treated as an initial estimate for each fracture set for use in the subsequent analyses (Table 5-9). The three fracture sets determined for Tptpmn are nearly orthogonal, whereas those for Tptpll are not [particularly those reported by Nieder-Westermann (2000)]. Calculating the best fit (Fisher vector and Bingham axial distributions) for the Tptpmn sets [Figure 5-1(A)] gives averages of 124°/83° (set 1, 9.5° cone at 95-percent confidence), 208°/83° (set 2, 19.5° cone at 95-percent confidence), and 313°/16° (set 3, 19.1° cone at 95-percent confidence). Calculating the vector mean for the Tptpll sets [Figure 5-1(B)] gives averages of 151°/81° (set 1, 26.5° cone at 95-percent confidence), 016°/82° (set 2, no confidence cone because of poor two-point spread), and 333°/06° (set 3, 5.6° cone at 95-percent confidence).

Fracture intensity, aperture, joint roughness coefficient, and tracelength are summarized in Table 5-8 for the Tptpmn and Tptpll intervals and further subdivided into fracture sets using the set-selection criteria of Mongano, et al. (1999) and Nieder-Westermann (2000). Fracture intensity generally is higher for the middle nonlithophysal interval, compared with the lower lithophysal interval. The data reflect a dominance of long fractures {lower tracelength cutoff of 1 m [3.28 ft]}, however, and the intensity in the lower lithophysal interval would be higher if the smaller fractures were included. Measured fracture apertures are typically smaller for the Tptpmn compared with the Tptpll interval, with the set 2 fractures in each interval having the largest values. Likewise, joint roughness coefficients are greater for the lower lithophysal interval regardless of fracture set. Finally, median tracelengths do not show a strong variation with respect to presence or absence of lithophysae, however, the set 3 fractures (subhorizontal) are typically longer.

Table 5-9. Summary of Fracture Set Orientations

Fracture Set	Tptpmn	Tptpll
1	124°/83°	151°/81°
2	208°/83°	016°/82°
3	313°/16°	333°/06°

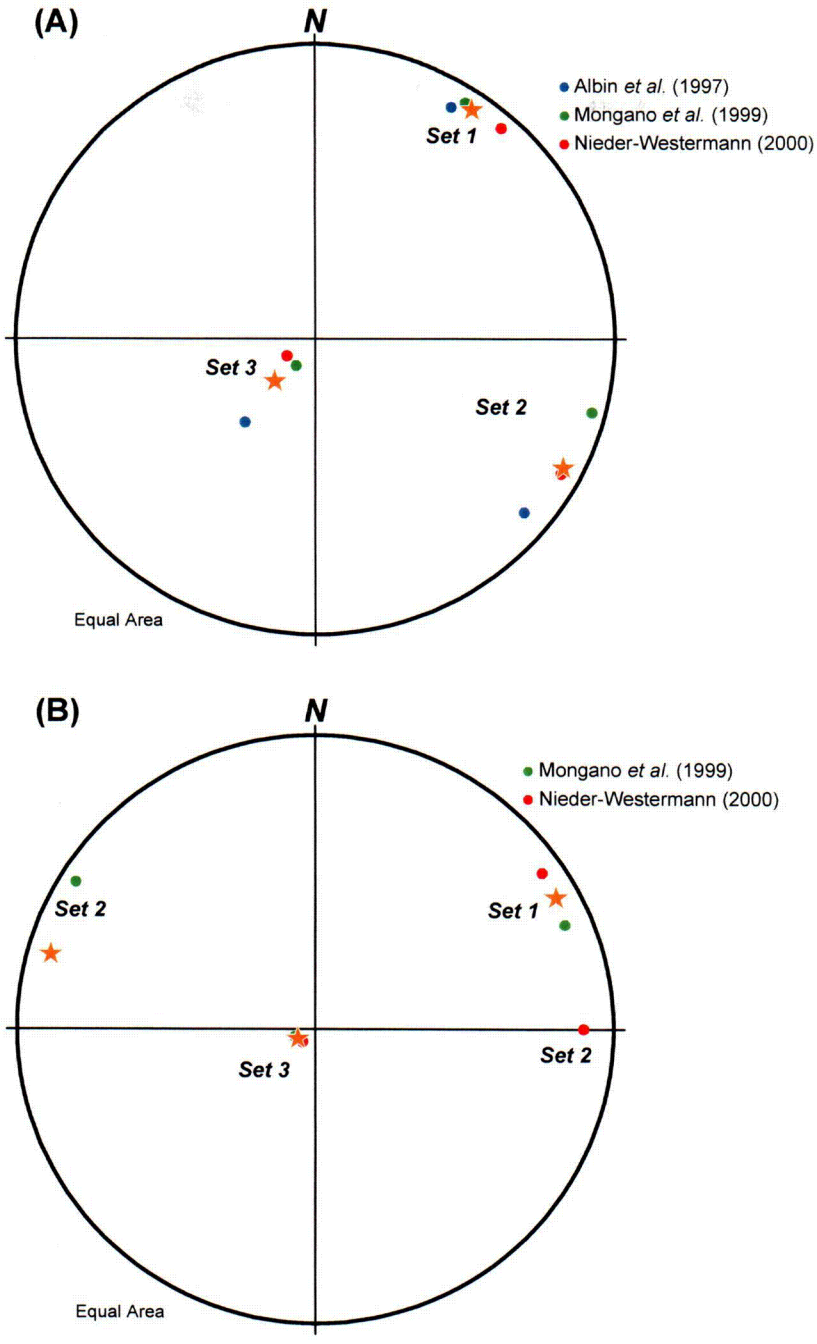

Figure 5-1. Equal-area stereonet plots of poles to fracture sets for (A) Tptpmn and (B) Tptpll. The average fracture set pole is shown as an orange star. See document text for further details.

C06

6 JOINT CLOSURE STRAIN

6.1 General Approach

The amount of shortening that can be accommodated via joint closure can be bounded at the upper end by the initial joint aperture (i.e., 100-percent shortening would completely close the joint). This is clearly an upper-bound closure because joint surface topography (i.e., roughness and asperities) prevents all but the smoothest of surfaces from closing completely. Other estimates can be obtained from the literature. Bandis, et al. (1983) and Barton, et al. (1985) present empirically derived equations for determining joint closure as a function of normal stress, material parameters (e.g., joint roughness coefficient, joint compressive strength and initial joint aperture), or both. Hsiung, et al. (1994) analyzed natural fractures in the Apache Leap Tuff and determined an average aperture change of approximately 50 percent is typical for these rocks.

Bandis, et al. (1983) derived an empirical relationship for maximum joint closure (V_m) as a function of initial aperture thickness (a_j), joint compressive strength (JCS), and joint roughness coefficient (JRC):

$$V_m = A + B \cdot \mathrm{JRC} + C \cdot \left(\frac{\mathrm{JCS}}{a_j} \right)^D \tag{6-1}$$

where *A, B, C,* and *D* are constants derived from the regression analyses of multiple loading and unloading cycles. This relationship is considered suitable for unfilled, interlocked joints where JRC = 5 through 15, JCS = 22 through 182 MPa [3,191 through 26,397 psi], a_j = 0.10 through 0.60 mm [0.0039 through 0.024 in], and the initial normal stress (σ_{ni}) ≤1 kPa [0.145 psi]. Values of the constants for three (or more) cycles as given by Bandis, et al. (1983) are *A* = -0.1032, *B* = -0.0074, *C* = 1.1350 and *D* = -0.2510. As a check on the data, the initial joint aperture can be calculated from

$$a_j = \frac{\mathrm{JRC}}{5} \left(0.2 \cdot \frac{\sigma_c}{\mathrm{JCS}} - 0.1 \right) \tag{6-2}$$

where σ_c is the uniaxial (unconfined) compressive strength.

Building on earlier work, Barton, et al. (1985) present a joint closure model that predicts the change in joint aperture (ΔV_j) in terms of the normal stress (σ_n):

$$\Delta V_j = \frac{a \cdot \sigma_n}{1 + b \cdot \sigma_n} \tag{6-3}$$

where $a = \frac{1}{K_{ni}}$, and $\frac{a}{b} = V_m$. The initial joint normal stiffness (K_{ni}) is given by

$$K_{ni} = -7.15 + 1.75 \cdot \mathrm{JRC} + 0.02\left(\frac{\mathrm{JCS}}{a_j}\right) \tag{6-4}$$

Barton, et al. (1985) point out normal stiffness values are not constant, but vary as a function of the normal stress. As such, the value of K_{ni} needs to be determined for each increment using

$$K_n = K_{ni}\left[1 - \frac{\sigma_n}{V_m \cdot K_{ni} + \sigma_n}\right]^{-2} \tag{6-5}$$

Using the values *A*, *B*, *C*, and *D* from Bandis, et al. (1983), Eq. (6-1) can be used to estimate the maximum joint closure. Alternatively, Eqs. (6-3) and (6-4) can be used to determine the change in joint normal aperture. Finally, Hsiung, et al. (1994) fit Eq. (5-3) to normal stress versus normal displacement data from experiments on the Apache Leap Tuff and determined values of pairs of constants *a* and *b* for five loading/unloading cycles. The mean values for the fifth cycle from their 27 tests were *a* = 0.0557 ± 0.0343, and *b* = 0.2836 ± 0.1047. Using these values, Eq. (6-3) can be solved for joint aperture change as a function of normal stress. It should be noted the Barton, et al. (1985) relationship explicitly does not include a measure of initial fracture aperture. Ofoegbu (2000) also noted initial fracture aperture may be substantially different (i.e., smaller) than the aperture measured under zero stress as measured at the surface of an outcrop or excavation [based on data from Snow (1968)].

6.2 Joint Closure Strain Results

Based on the previous discussion, a spreadsheet was established to estimate the change in joint aperture using the four different formulations. The upper bound is given by complete joint closure. Results show the lower bound is the 50-percent shortening (i.e., closure of joint to one-half the initial aperture) determined by Hsiung, et al. (1994) for the Apache Leap Tuff. Intermediate values of aperture change are given by Eqs. (6-1) and (6-5).

Joint closure strains are calculated for the middle nonlithophysal and lower lithophysal intervals for each of the three fracture sets using the Mongano, et al. (1999) and the Nieder-Westermann (2000) selection criteria. To estimate the joint closure strains, the measured fracture intensities are used to determine the number of fractures present for a target length. The subhorizontal fractures (set 3) will accommodate subvertical normal strain, and, as such, the target length for set 3 fractures is the average unit thickness {~33.5 m [110 ft] for Tptpmn and ~86.5 m [284 ft] for Tptpll}. The subvertical fractures (sets 1 and 2) will accommodate the subhorizontal normal strain. The target lengths for the subvertical fractures (sets 1 and 2) were determined from the current potential repository geometry (i.e., emplacements drifts oriented 072°) and the strike-normal for the fracture set (Figure 6-1).

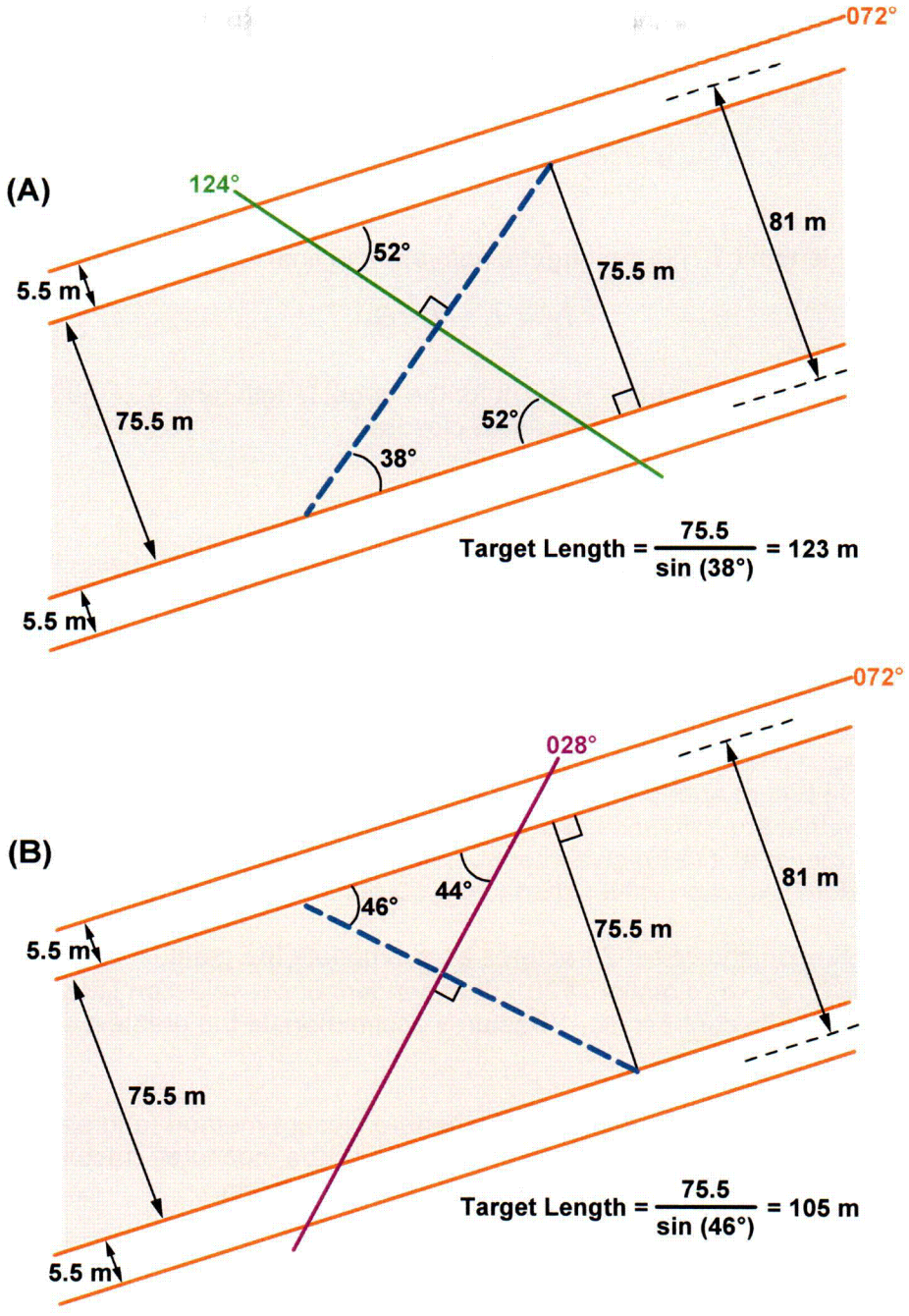

Figure 6-1. Map-view illustration of geometry for potential repository (emplacement drift walls in orange with interdrift area in gray) and near-vertical fractures for (A) set 1 (green line) and (B) set 2 (purple line). Orientations and dimensions are shown for reference with blue dashed line representing target length over which joint closure strain is calculated. Recall the *in-situ* stress state is characterized by the maximum horizontal stress ($\sigma_H = \sigma_2$) trending 030° with the minimum horizontal stress ($\sigma_h = \sigma_3$) trending 120°. See document text for further details. NOTE: Information provided in meters; for conversion, use 1 m = 3.28 ft.

C07

The target lengths for sets 1 and 2 fractures are 123 and 105 m [404 ft and 345 ft]. The joint closure strain is then calculated as an elongation from

$$\varepsilon = \frac{l_f - l_i}{l_i} \tag{6-6}$$

where the initial length (l_i) is the target length and the final length (l_f) is given by

$$l_f = l_i - n \cdot a_f \tag{6-7}$$

where n is the number of fractures present for the target length, and a_f is the new aperture (i.e., the initial aperture minus the calculated closure).

6.3 Joint Closure Strain Summary

Joint closure strains are calculated for the Tptpmn and Tptpll intervals using the fracture intensity and aperture estimates of Mongano, et al. (1999) and Nieder-Westermann (2000) and the four different aperture closure formulations (Table 6-1). This results in 16 combinations of joint closure strains, 8 each for the Tptpmn and Tptpll intervals.

As previously discussed, the maximum aperture reduction method yields the largest strain estimates because it assumes complete closure of the fractures from the initial aperture values. The 50-percent aperture reduction method provides a reasonable lower bound with strain estimates that are half those of the first method. The empirical relations of Bandis, et al. (1983) and Barton, et al. (1985) give intermediate estimates, although both are closer to the maximum aperture reduction values than to the 50-percent aperture reduction case.

Qualitative evaluation shows set 2 fractures accommodate the greatest shortening for the Tptpmn interval (*in-situ* σ_h direction, 120°), independent of set-selection criteria or aperture closure formulation. In contrast, set 1 fractures accommodate the greatest shortening in Tptpll (*in-situ* σ_H direction, 030°).

It is important to note that regardless of the aperture closure method (and also independent of stratigraphic interval and fracture-set selection criteria), the measured fracture data result in a significant potential for horizontal thermal strain accommodation.

Table 6-1. Summary of Joint Strain* Estimates for Tptpmn and Tptpll Intervals					
Aperture Closure Method		Mongano, et al.†		Nieder-Westermann ‡	
		Tptpmn	Tptpll	Tptpmn	Tptpll
Maximum Aperture Reduction	Set 1	-1.34×10^{-3}	-2.75×10^{-3}	-1.47×10^{-3}	-1.16×10^{-3}
	Set 2	-6.73×10^{-3}	-5.10×10^{-4}	-5.20×10^{-3}	-7.50×10^{-4}
	Set 3	-3.70×10^{-4}	-6.84×10^{-4}	-3.70×10^{-4}	-7.05×10^{-5}
50-Percent Aperture Reduction	Set 1	-6.72×10^{-4}	-1.14×10^{-3}	-7.33×10^{-4}	-5.82×10^{-4}
	Set 2	-3.37×10^{-3}	-2.55×10^{-4}	-2.60×10^{-3}	-3.75×10^{-4}
	Set 3	-1.85×10^{-4}	-3.42×10^{-4}	-1.85×10^{-4}	-3.53×10^{-5}
Bandis, et al.§	Set 1	-1.20×10^{-3}	-1.97×10^{-3}	-1.31×10^{-3}	-9.46×10^{-4}
	Set 2	-6.33×10^{-3}	-4.61×10^{-4}	-4.96×10^{-3}	-6.47×10^{-4}
	Set 3	-3.98×10^{-4}	-4.18×10^{-4}	-3.98×10^{-4}	-4.40×10^{-5}
Barton, et al.¶	Set 1	-1.00×10^{-3}	-2.15×10^{-3}	-1.16×10^{-3}	-1.06×10^{-3}
	Set 2	-6.36×10^{-3}	-4.92×10^{-4}	-5.03×10^{-3}	-7.06×10^{-4}
	Set 3	-6.36×10^{-5}	-3.69×10^{-4}	-6.36×10^{-5}	-3.94×10^{-5}

*Negative strain values indicate a contractional (i.e., shortening) strain. See main document text for further discussion.

†Mongano, G.S., W.L. Singleton, T.C. Moyer, S.C. Beason, G.L.W. Eatman, A.L. Albin, and R.C. Lung. "Geology of the ECRB Cross Drift—Exploratory Studies Facility, Yucca Mountain Project, Yucca Mountain, Nevada." SPG42GM3. Denver, Colorado: U.S. Geological Survey. 1999.

‡Nieder-Westermann, G.H. "Fracture Geometry Analysis for the Stratigraphic Units of the Repository Host Horizon." ANL–EBS–GE–000006. Rev. 00. Las Vegas, Nevada: CRWMS M&O. 2000.

§Bandis, S.C., A.C. Lumsden, and N.R. Barton. "Fundamentals of Rock Joint Deformation." *International Journal of Rock Mechanics and Mining Science.* Vol. 20, No. 6. pp. 249–268. 1983.

¶Barton, N., S. Bandis, and K. Bakhtar. "Strength, Deformation, and Conductivity Coupling of Rock Joints." *International Journal of Rock Mechanics and Mining Science.* Vol. 22, No. 3. pp. 121–140. 1985.

7 THERMAL STRESS RESULTS

7.1 Review of Assumptions

Several simplifying assumptions are employed in this evaluation. First, only the three principal (i.e., normal) stresses are considered, and each principal stress is assumed to act on one and only one joint set—that is, the joint set normal to that principal stress. Also, a principal stress that is compressional is assumed to act to close a joint, whereas a tensional stress will act to dilate a joint. Given the average fracture set orientations, a further simplifying assumption is made: (i) set 1 fractures with northwest-southeast strike will accommodate mainly northeast-southwest strain via closure (i.e., the *in-situ* maximum horizontal stress direction σ_H), (ii) set 2 fractures with northeast-southwest strike will accommodate mainly northwest-southeast strain via closure (i.e., the *in-situ* minimum horizontal stress direction σ_h), and (iii) the subhorizontal set 3 fractures will accommodate mainly vertical stress. Finally, the analysis assumes the system can be treated as a uniformly heated body (i.e., no temperature gradient in any direction).

7.2 General Approach

Joint closure strains for each of the 16 cases are used in the thermal stress spreadsheet to estimate a hypothetical stress history {cf. Eq. [4-14]}. Calculations assume an initial temperature of 20 °C [68 °F] with a 5 °C [41 °F] temperature step up to a maximum of 220 °C [428 °F], which corresponds to a temperature change from 0 to 200 °C [32 to 392 °F]. The upper temperature exceeds the current repository estimates but was chosen to maximize any stress increase. To simplify the analysis, it is assumed the temperature effect acts uniformly for the entire volume of interest (i.e., the entire target length) rather than a distribution that is high near the drift-wall contact and decays to lower temperatures further away.

A density of 2,210 kg/m^3 [0.0798 lbs/in^3] is assumed for all rock, and a depth of 323 m [1,060 ft] is selected for all calculations. These values provide a good fit to the *in-situ* stress magnitudes {i.e., σ_v = 7.0 MPa [1,015 psi], σ_H = 4.2 MPa [609 psi], σ_h = 3.5 MPa [508 psi]}. Other material parameters are Young's Modulus of 20 GPa [2.90 × 10^6 psi], coefficient of thermal expansion of 10^{-5} K^{-1} [-4.58×10^{-3} °F^{-1}], Poisson's Ratio of 0.21, and uniaxial compressive strength of 187 MPa [2.71 × 10^4 psi]. For failure envelope calculations, the good rock (RMQ5) was assigned an internal friction angle of 34.4° and cohesion of 5.08 MPa [737 psi], whereas the poor rock (RMQ1) has an internal friction angle of 27.2° and cohesion of 2.82 MPa [409 psi].

7.3 Stress-State Evaluation for Tptpmn and Tptpll

The effect of increasing temperature on the overall stress state (i.e., increase because of temperature change) is partially mitigated by allowing joint closure strains (up to the calculated magnitude) to accommodate thermal-stress induced strain [(cf. Eq. (4-14)]. For the extreme end member case of complete horizontal constraint with no vertical constraint subjected to uniform heating (Figure 7-1), results mimic earlier work in that a switch of principal stress axes occurs (i.e., minimum principal stress becomes vertical). It is worth noting, however, the analyses show the maximum principal stress for such a case should only reach levels of ~28 MPa [4,061 psi] for RMQ1 and ~45 MPa [6,527 psi] for RMQ5 before the differential

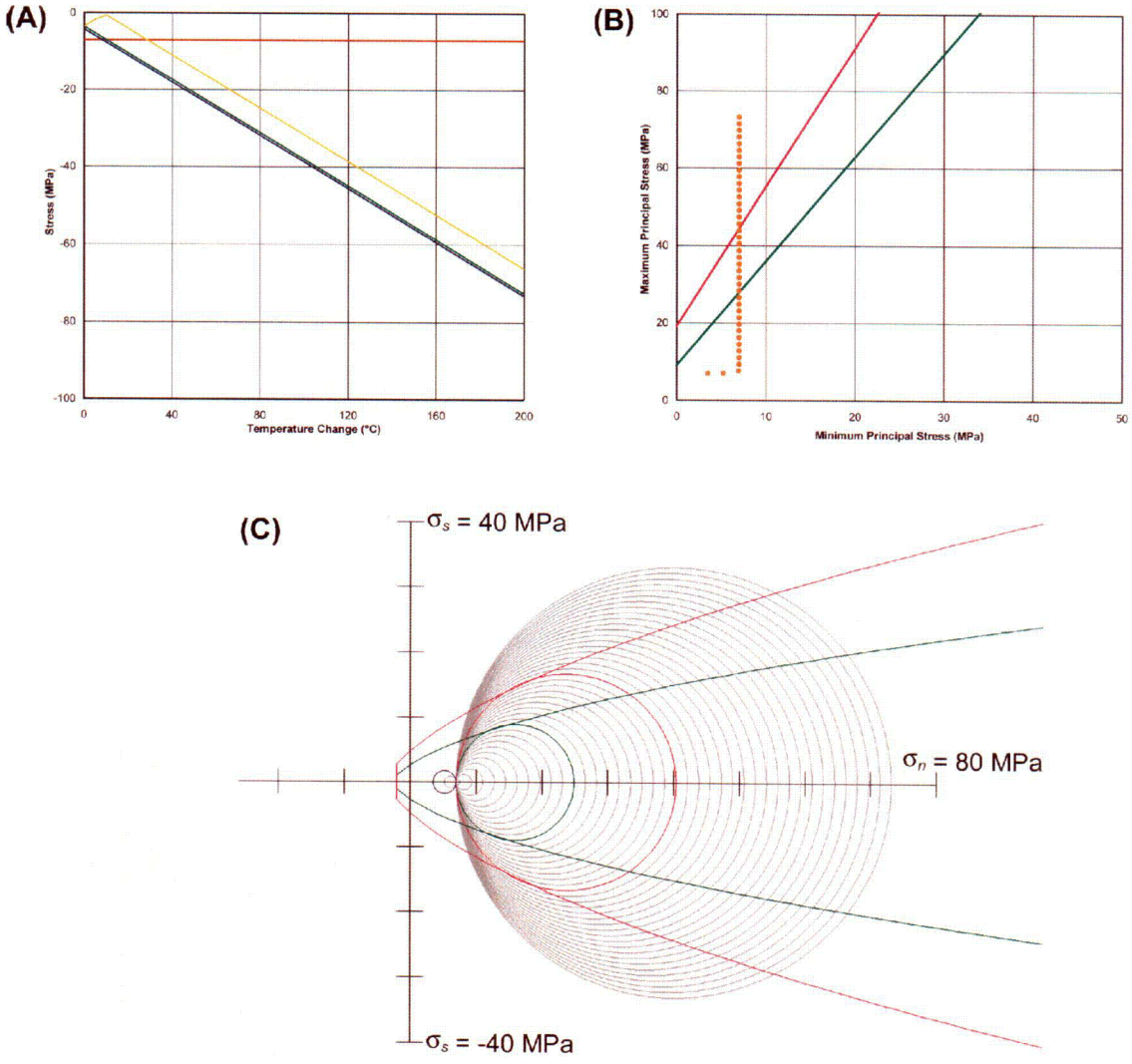

Figure 7-1. Summary of results for system that is horizontally constrained but vertically unconstrained. (A) Temperature versus stress-state plot showing stress magnitude (red = σ_v, blue = horizontal 030°, and green = horizontal 120°) plus maximum differential stress (yellow = $\sigma_1 - \sigma_3$). (B) Stress-state evolution (orange points) plotted in principal stress space (σ_1 versus σ_3) showing Coulomb failure envelopes for good rock (RMQ5 = pink) and poor rock (RMQ1 = green). (C) Stress-state evolution in Mohr space (σ_n versus σ_s) with superimposed Hoek-Brown failure envelopes (RMQ5 = pink and RMQ1 = green) showing *in-situ* stress state (blue) and stress states at failure. See document text for further discussion.

C08

stress exceeds the failure strength. Principal stress magnitudes >50 MPa [7,252 psi] {differential stress of ~43 MPa [6,237 psi]} are not attainable. This rationale is illustrated by means of failure envelopes and stress state plotted in two different stress spaces—σ_1 versus σ_3 (i.e., principal stress space) and σ_n versus σ_s (i.e., Mohr space).

Results demonstrate that none of the eight cases for the Tptpmn interval result in a switching of the principal stress axes. Figures 7-2 through 7-5 illustrate results for the Tptpmn interval using set-selection criteria and the maximum and 50-percent aperture reduction methods. Illustrations for the remaining four Tptpmn cases are provided in the Appendix (Figures 1 through 4). The vertical stress always remains the maximum principal stress (up to and beyond the point where the rocks would fail). Also, the minimum horizontal stress always remains oriented at 120° and does not increase in magnitude beyond its initial value of 3.5 MPa [508 psi]. The results appear relatively insensitive to the set selection criteria (compare Figures 7-2 with 7-3 and 7-4 with 7-5), although the intermediate principal stress (σ_2) begins increasing at a lower temperature {ΔT = 135 °C [275 °F] versus 150 °C [302 °F]}. As expected, the primary difference in results of the aperture reduction method is stress increases at lower temperature (because less strain is accommodated). For example, the maximum principal stress ($\sigma_1 = \sigma_v$) begins increasing in magnitude at ΔT = 20 °C [68 °F] for the 50-percent aperture reduction case versus ΔT = 40 °C [104 °F] for the maximum aperture reduction case (compare Figures 7-2 with 7-4 and 7-3 with 7-5).

The results for the Tptpll interval are somewhat less straightforward than those for the Tptpmn interval. For all but one of the eight cases, the vertical stress remains the maximum principal stress. The only case (Figure 7-6) where the vertical stress ceases to be σ_1 occurs for the Mongano, et al. (1999) set-selection criteria using the case of maximum joint closure strain (i.e., the upper bound case where the joint is assumed to close completely equals reduction to zero aperture). The initial minimum principal stress ($\sigma_3 = \sigma_h$ at 120°) begins to increase at ΔT = 55 °C [131 °F] and becomes larger than σ_v at ΔT = 65 °C [149 °F] (so the stress state becomes $\sigma_1 = \sigma_H$ at 120°, $\sigma_2 = \sigma_v$, and $\sigma_3 = \sigma_h$ at 030°). At ΔT = 70 °C [158 °F], the vertical stress begins increasing so the difference between σ_1 and σ_2 never exceeds 2.5 MPa [363 psi]. Rock failure is predicted at σ_1 = 21 MPa [3,046 psi] for RMQ1 and 36 MPa [5,221 psi] for RMQ5. The 50 percent aperture-closure case (Figure 7-7) for the Mongano, et al. (1999) set criteria comes close because the horizontal 120° stress (i.e., initial σ_3) increases to nearly the same magnitude as σ_v {difference of ~0.5 MPa [73 psi]}.

A switch in relative magnitude of the horizontal stress axes is common to all cases for the Tptpll interval (Figures 7-6 and 7-7 and appendix Figures 5 through 10). The minimum horizontal stress goes from 120° to 030°. This reflects the combination of relatively high intensity and large apertures for the set 1 fractures in this interval, which allows greater horizontal thermal strain accommodation in the 030° direction.

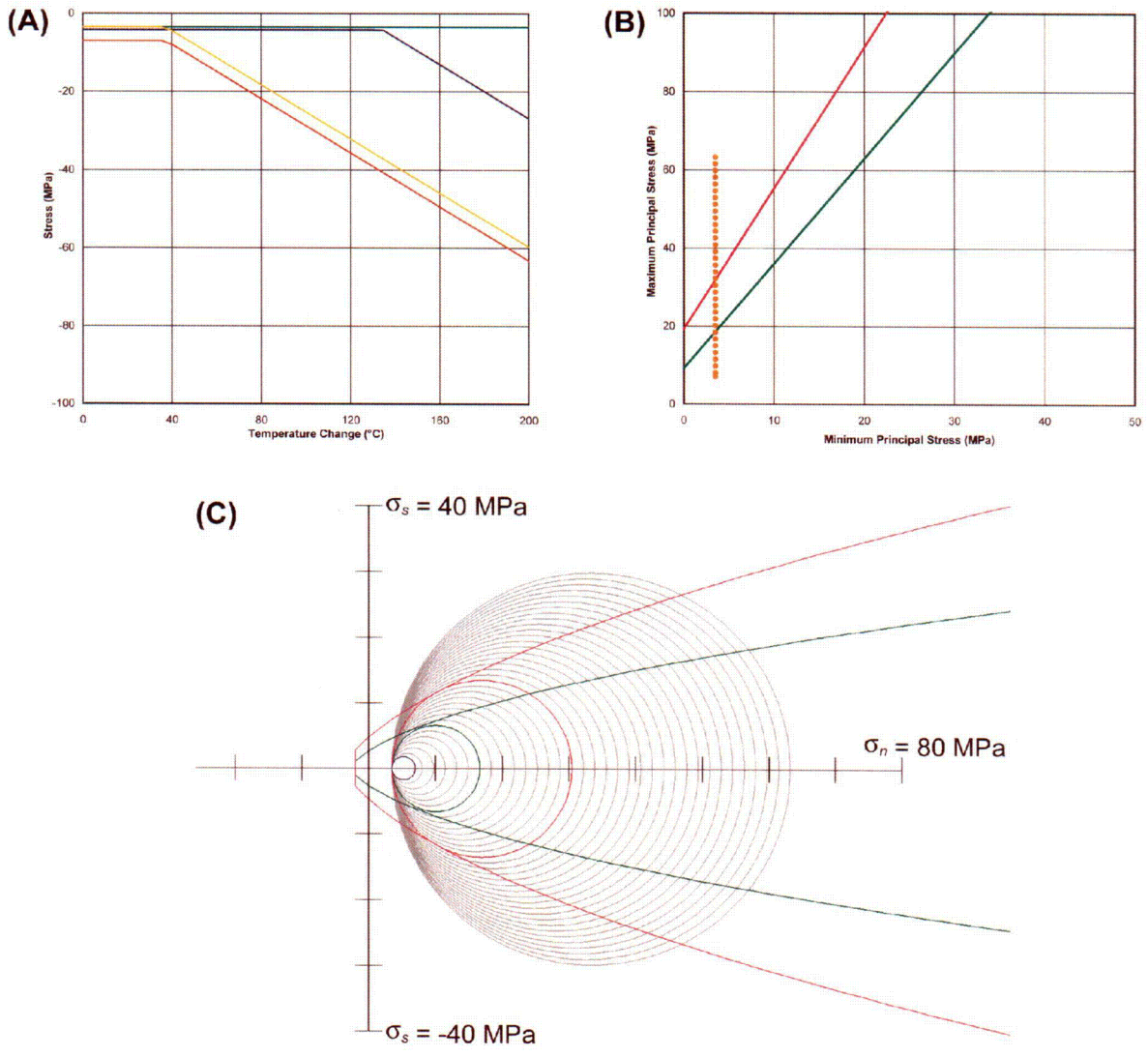

Figure 7-2. Summary of results for Tptpmn interval using Mongano, et al. (1999) set selection criteria and maximum aperture reduction method. (A) Temperature versus stress-state plot showing stress magnitude (red = σ_v, blue = horizontal 030°, and green = horizontal 120°) plus maximum differential stress (yellow = $\sigma_1 - \sigma_3$). (B) Stress-state evolution (orange points) plotted in principal stress space (σ_1 versus σ_3) showing Coulomb failure envelopes for good rock (RMQ5 = pink) and poor rock (RMQ1 = green). (C) Stress-state evolution in Mohr space (σ_n versus σ_s) with superimposed Hoek-Brown failure envelopes (RMQ5 = pink and RMQ1 = green) showing *in-situ* stress state (blue) and stress states at failure. See document text for further discussion.

C09

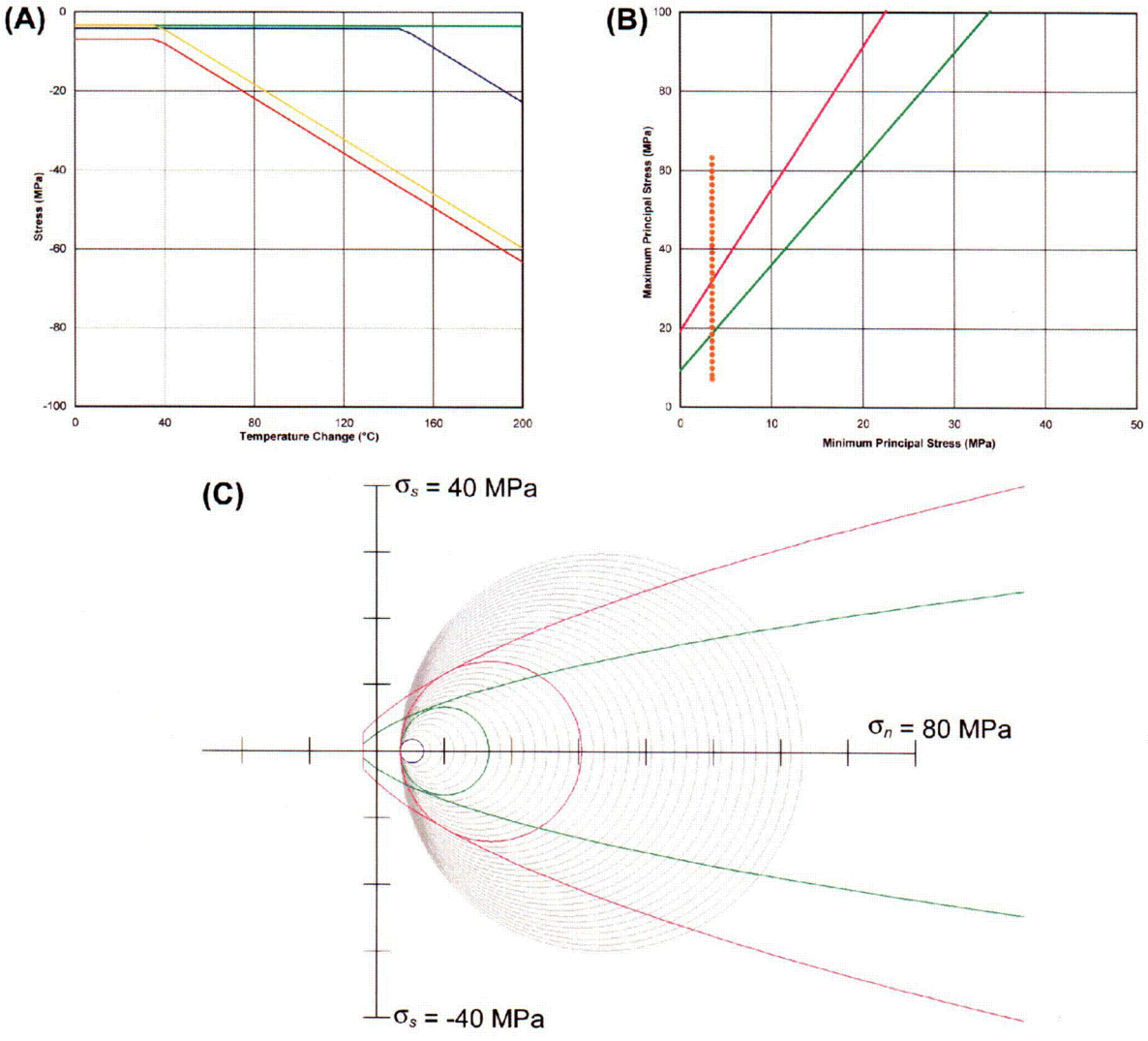

Figure 7-3. Summary of results for Tptpmn interval using Nieder-Westermann (2000) set selection criteria and maximum aperture reduction method. (A) Temperature versus stress-state plot showing stress magnitude (red = σ_v, blue = horizontal 030° and green = horizontal 120°) plus maximum differential stress (yellow = $\sigma_1 - \sigma_3$). (B) Stress-state evolution (orange points) plotted in principal stress space (σ_1 versus σ_3) showing Coulomb failure envelopes for good rock (RMQ5 = pink) and poor rock (RMQ1 = green). (C) Stress-state evolution in Mohr space (σ_n versus σ_s) with superimposed Hoek-Brown failure envelopes (RMQ5 = pink and RMQ1 = green) showing *in-situ* stress state (blue) and stress states at failure. See document text for further discussion.

C10

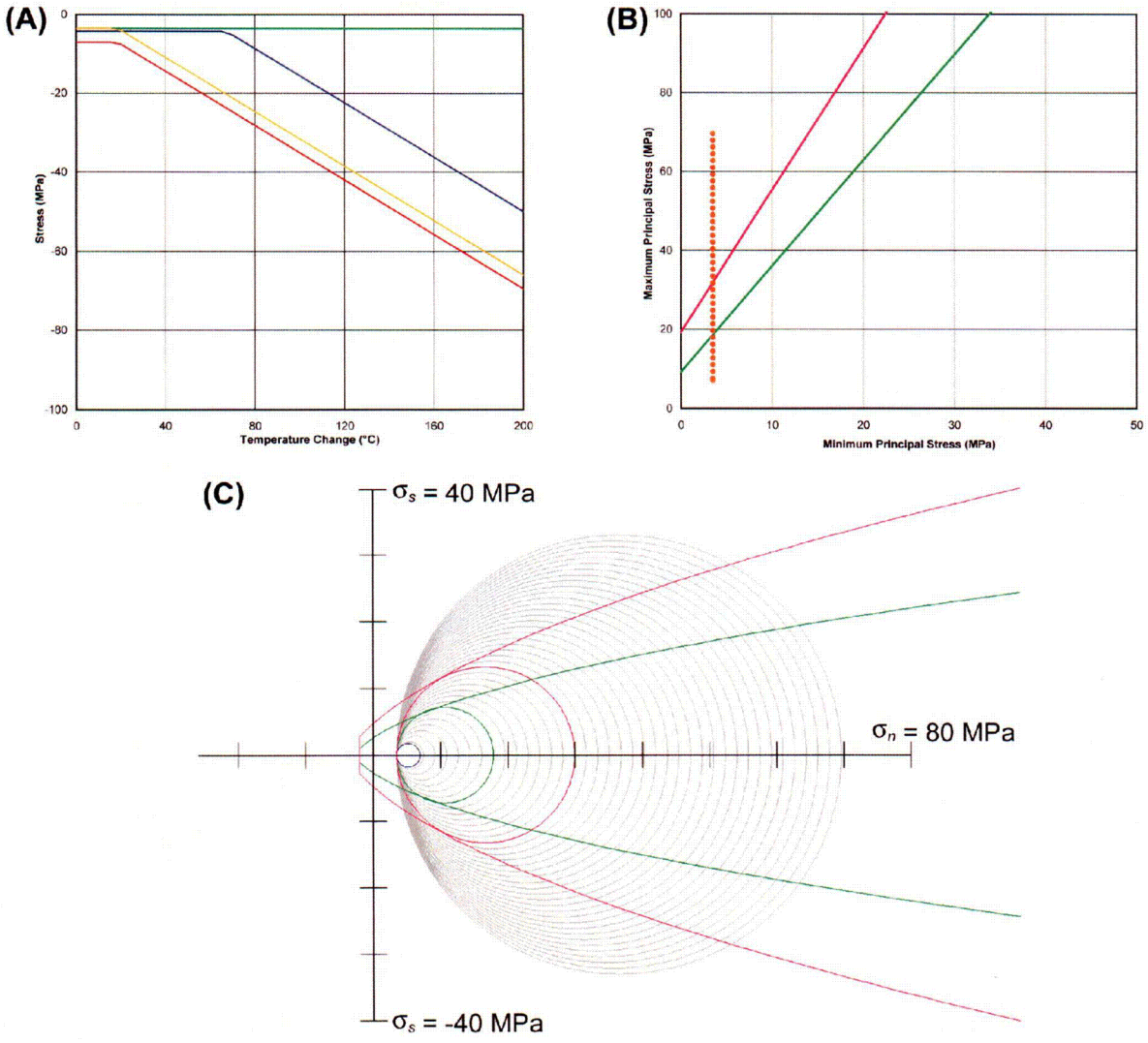

Figure 7-4. Summary of results for Tptpmn interval using Mongano, et al. (1999) set selection criteria and 50-percent aperture reduction method. (A) Temperature versus stress-state plot showing stress magnitude (red = σ_v, blue = horizontal 030° and green = horizontal 120°) plus maximum differential stress (yellow = $\sigma_1 - \sigma_3$). (B) Stress-state evolution (orange points) plotted in principal stress space (σ_1 versus σ_3) showing Coulomb failure envelopes for good rock (RMQ5 = pink) and poor rock (RMQ1 = green). (C) Stress-state evolution in Mohr space (σ_n versus σ_s) with superimposed Hoek-Brown failure envelopes (RMQ5 = pink and RMQ1 = green) showing *in-situ* stress state (blue) and stress states at failure. See document text for further discussion.

C11

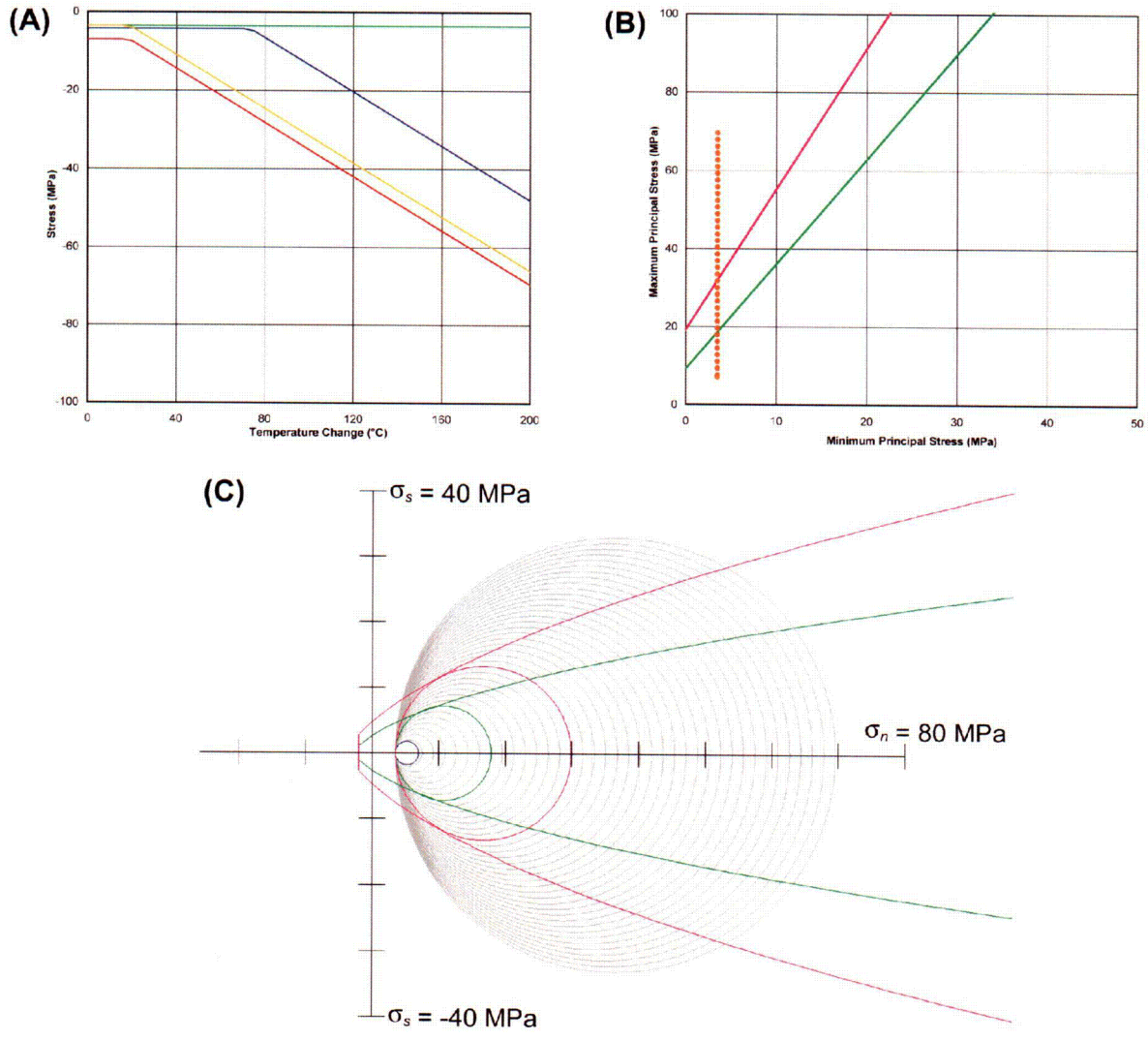

Figure 7-5. Summary of results for Tptpmn interval using Nieder-Westermann (2000) set selection criteria and 50-percent aperture reduction method. (A) Temperature versus stress-state plot showing stress magnitude (red = σ_v and blue = horizontal 030°, green = horizontal 120°) plus maximum differential stress (yellow = $\sigma_1 - \sigma_3$). (B) Stress-state evolution (orange points) plotted in principal stress space (σ_1 versus σ_3) showing Coulomb failure envelopes for good rock (RMQ5 = pink) and poor rock (RMQ1 = green). (C) Stress-state evolution in Mohr space (σ_n versus σ_s) with superimposed Hoek-Brown failure envelopes (RMQ5 = pink and RMQ1 = green) showing *in-situ* stress state (blue) and stress states at failure. See document text for further discussion.

C12

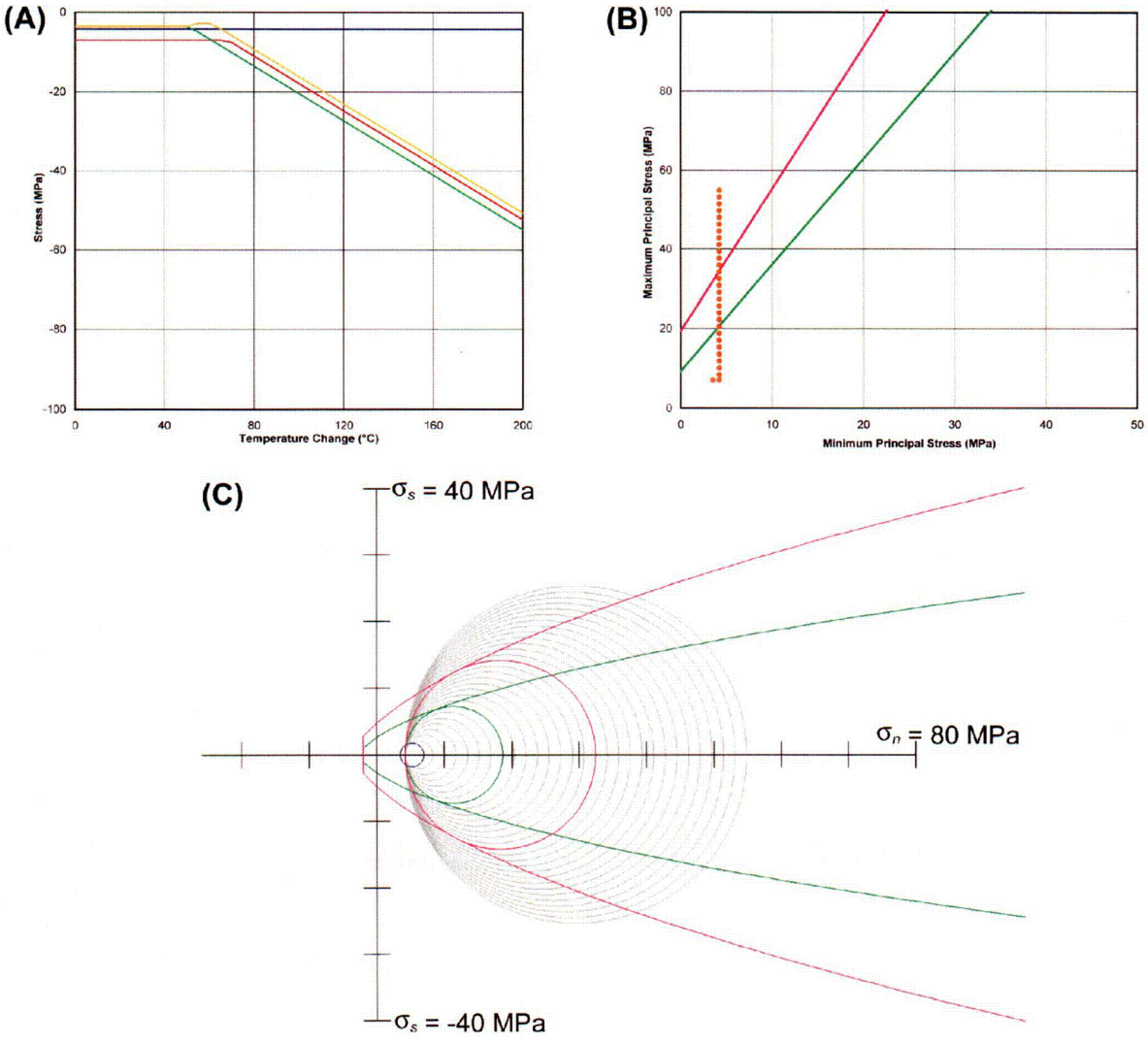

Figure 7-6. Summary of results for Tptpll interval using Mongano, et al. (1999) set selection criteria and maximum aperture reduction method. (A) Temperature versus stress-state plot showing stress magnitude (red = σ_v, blue = horizontal 030° and green = horizontal 120°) plus maximum differential stress (yellow = $\sigma_1 - \sigma_3$). (B) Stress-state evolution (orange points) plotted in principal stress space (σ_1 versus σ_3) showing Coulomb failure envelopes for good rock (RMQ5 = pink) and poor rock (RMQ1 = green). (C) Stress-state evolution in Mohr space (σ_n versus σ_s) with superimposed Hoek-Brown failure envelopes (RMQ5 = pink and RMQ1 = green) showing *in-situ* stress state (blue) and stress states at failure. See document text for further discussion.

C13

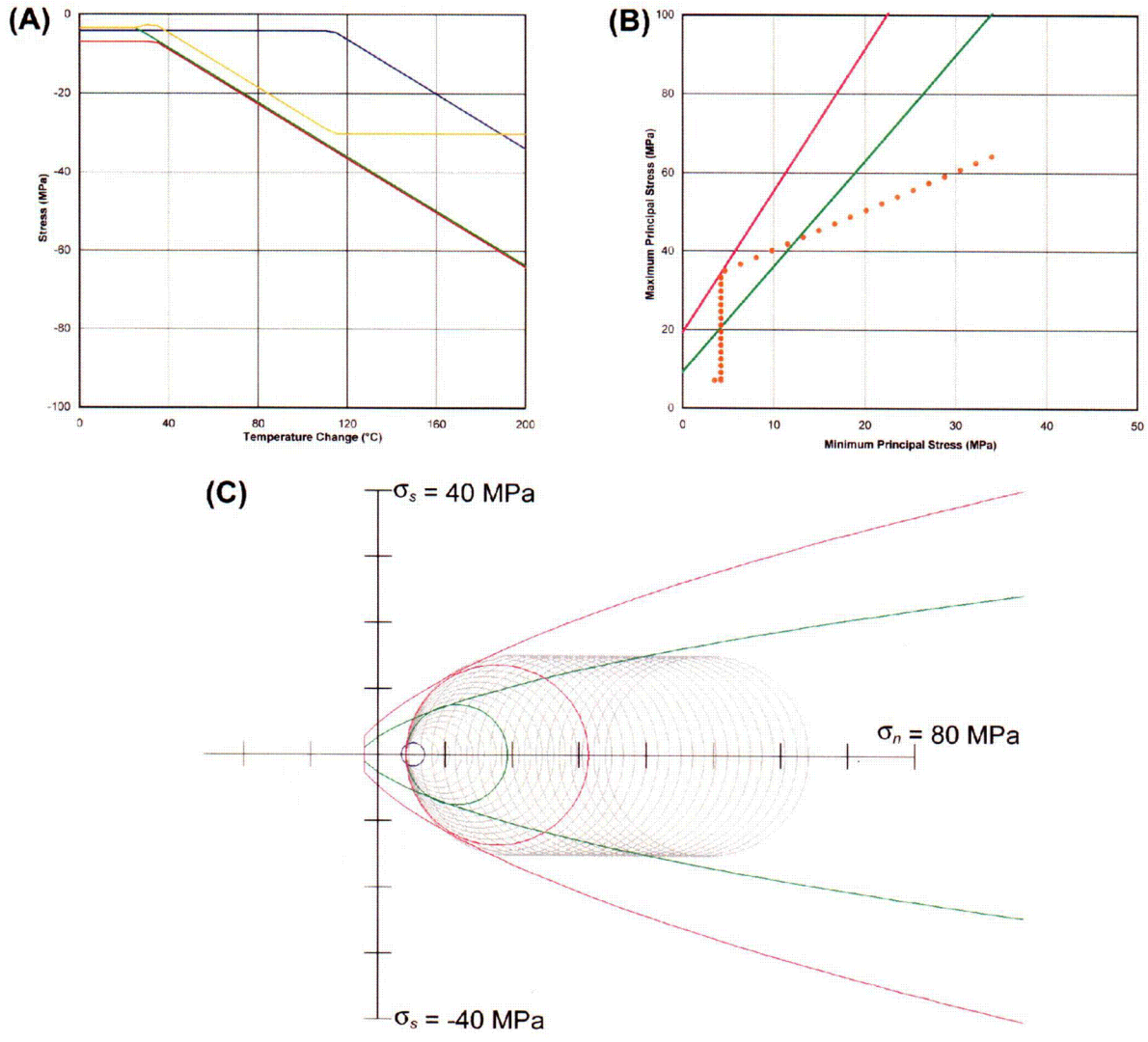

Figure 7-7. Summary of results for Tptpll interval using Mongano, et al. (1999) set selection criteria and 50-percent aperture reduction method. (A) Temperature versus stress-state plot showing stress magnitude (red = σ_v, blue = horizontal 030° and green = horizontal 120°) plus maximum differential stress (yellow = $\sigma_1 - \sigma_3$). (B) Stress-state evolution (orange points) plotted in principal stress space (σ_1 versus σ_3) showing Coulomb failure envelopes for good rock (RMQ5 = pink) and poor rock (RMQ1 = green). (C) Stress-state evolution in Mohr space (σ_n versus σ_s) with superimposed Hoek-Brown failure envelopes (RMQ5 = pink and RMQ1 = green) showing *in-situ* stress state (blue) and stress states at failure. See document text for further discussion.

C14

8 SUMMARY AND CONCLUSIONS

The potential for wide-spread alteration of the *in-situ* stress state at the potential high-level waste repository site at Yucca Mountain because of thermal effects of waste emplacement is reassessed. This reassessment involves

- Summarizing previous thermal stress studies, including methodology, assumptions, and primary conclusions
- Exploring aspects of the Yucca Mountain geology that have not been fully incorporated into previous analyses and examination of the potential effects on the thermal stress distribution
- Developing a simple, first-order calculation to assess the likelihood for thermal strain accommodation via fracture closure

Review of earlier work suggests repository-scale stress-state alteration is predicated on assumptions that do not reflect accurately the geology of Yucca Mountain. For these conditions, the increased thermal load from waste package heat generation leads to a significant increase in the horizontal stress magnitudes without a corresponding increase in the vertical stress. As such, the vertical stress quickly becomes the minimum principal stress.

Review of the existing fracture data for the potential repository host horizons shows two steeply dipping and nearly orthogonal fracture sets are present. Fractures in the two subvertical sets are oriented approximately perpendicular to the *in-situ* horizontal stresses, and, as such, they are suited to accommodate thermal strain. A third set of subhorizontal fractures also is present in the potential repository host horizon intervals. These joints are capable of accommodating vertical thermal strain. The additional compliance caused by the closure of such fractures likely will reduce the normally induced stress relative to values calculated using models that assume a linear elastic and isotropic medium.

Magnitude calculations for joint closure strain are based on fracture intensity and average aperture. An upper bound is given by assuming each fracture closes completely (100-percent shortening), whereas empirical data from the Apache Leap Tuff suggest a lower bound of approximately 50-percent aperture reduction. Two additional estimates of joint closure, based on empirically derived relationships published in the rock mechanics literature, are also employed.

These simple first-order calculations suggest widespread change in principal stresses is unlikely. The intensity and orientation of the natural fractures are such that the stress increases are more uniformly distributed so the vertical stress remains the maximum principal stress for almost all test cases.

In light of this analysis, it is likely thermally induced stresses would be much smaller than suggested by the DOE analyses, and there is a reduced potential for wide-spread realignment of principal stress orientations. Consequently, igneous dike propagation is unlikely to be affected by thermally induced, repository-scale, stress-state modification.

9 REFERENCES

Albin, A.L., W.L. Singleton, T.C. Moyer, A.C. Lee, R.C. Lung, G.L.W. Eatman, and D.L. Barr. "Geology of the Main Drift—Station 28+00 to 55+00, Exploratory Studies Facility, Yucca Mountain Project, Yucca Mountain, Nevada." DOE Report DTN GS970208314224.005, Milestone Report SPG42AM3. Denver, Colorado: Bureau of Reclamation and U.S. Geological Survey. 1997.

Bandis, S.C., A.C. Lumsden, and N.R. Barton. "Fundamentals of Rock Joint Deformation." *International Journal of Rock Mechanics and Mining Science*. Vol. 20, No. 6. pp. 249–268. 1983.

Barr, G.E. "Dike Propagation Near Drifts." ANL–WIS–MD–000015. Rev. 00. ICN1. Las Vegas, Nevada: CRWMS M&O. 2000.

Barr, D.L., T.C. Moyer, W.L. Singleton, A.L. Albin, R.C. Lung, A.C. Lee, S.C. Beason, and G.L.W. Eatman. "Geology of the North Ramp—Station 4+00 to 28+00, Exploratory Studies Facility, Yucca Mountain Project, Yucca Mountain, Nevada." DOE Report DTN GS960908314224.020. Denver, Colorado: Bureau of Reclamation and U.S. Geological Survey. 1996.

Barton, N., S. Bandis, and K. Bakhtar. "Strength, Deformation, and Conductivity Coupling of Rock Joints." *International Journal of Rock Mechanics and Mining Science*. Vol. 22, No. 3. pp. 121–140. 1985.

Board, M. "Resolution Strategy for Geomechanically-Related Repository Design and Thermal-Mechanical Effects (RDTME)." Las Vegas, Nevada: Bechtel SAIC Company, LLC. 2003.

Board, M., A. Linden, and M. Zhu. "Design Evolution Study—Underground Layout." TDR–MGR–MG–000003. Rev. 00. Las Vegas, Nevada: Bechtel SAIC Company, LLC. 2002.

Brechtel, C.E., M. Lin, E. Martin, and D.S. Kessel. "Geotechnical Characterization of the North Ramp of the Exploratory Studies Facility." SAND95–0488/1 and 2 (two volumes). Albuquerque, New Mexico: Sandia National Laboratories. 1995.

CRWMS M&O. "Site Recommendation Subsurface Layout." ANL–SFS–MG–000001. Rev. 00. Las Vegas, Nevada: CRWMS M&O. 2000a.

———. "Yucca Mountain Site Description." TDR–CRW–GS–000001. Rev. 01. ICN 01. Las Vegas, Nevada: CRWMS M&O. 2000b.

Detournay, E., L.G. Mastin, J.R.A. Pearson, A.M. Rubin, and F.J. Spera. "Final Report of the Igneous Consequences Peer Review Panel." Las Vegas, Nevada: Bechtel SAIC Company, LLC. 2003.

DOE. "Yucca Mountain Science and Engineering Report Revision 1." DOE/RW–0539–1. Washington, DC: DOE, Office of Civilian Radioactive Waste Management. 2002.

Elliott, D. "Deformation Paths in Structural Geology." *Geological Society of America Bulletin.* Vol. 83. pp. 2,621–2,638. 1972.

Fedors, R., G. Adams, C. Manepally, and S. Green. "Thermal Conductivity, Edge Cooling, and Drift Degradation—Abstracted Model Sensitivity Analyses for Yucca Mountain." San Antonio, Texas: CNWRA. 2003.

Groshong, R.H. "Low-Temperature Deformation Mechanisms and Their Interpretation." *Geological Society of America Bulletin.* Vol. 100. pp. 1,329–1,360. 1988.

Hardy, M.P. and S.J. Bauer. "Rock Mechanics Considerations in Designing a Nuclear Waste Repository in Hard Rock." Proceedings of the 33rd U.S. Symposium on Rock Mechanics, Santa Fe, New Mexico, June 3–5, 1992. J.R. Tillerson and W.R. Wawersik, eds. Rotterdam, The Netherlands: A.A. Balkema. pp. 1,041–1,050. 1992.

———. "Drift Design Methodology and Preliminary Application for the Yucca Mountain Site Characterization Project." SAND89–0837. Albuquerque, New Mexico: Sandia National Laboratories. 1991.

Hsiung, S.M., D.D. Kana, M.P. Ahola, A.H. Chowdhury, and A. Ghosh. NUREG/CR–6178, CNWRA 93-013, "Laboratory Characterization of Rock Joints." San Antonio, Texas: CNWRA. 1994.

Jaeger, J.C. and N.G.W. Cook. *Fundamentals of Rock Mechanics.* 3rd Edition. London, England: Chapman and Hall, Ltd. 1979.

Kicker, D.C., E.R. Martin, C.E. Brechtel, C.A. Stone, and D.S. Kessel. "Geotechnical Characterization for the Main Drift of the Exploratory Studies Facility." SAND95–2183. Albuquerque, New Mexico: Sandia National Laboratories. 1997.

Liu, L. and M.D. Zoback. "The Effect of Topography on the State of Stress in the Crust: Application to the Site of the Cajon Pass Scientific Drilling Project." *Journal of Geophysical Research.* Vol. 97. pp. 5,095–5,100. 1992.

MacDougall, H.R., L.W.Scully, and J.R. Tillerson. "Site Characterization Plan Conceptual Design Report." SAND84–2641. Albuquerque, New Mexico: Sandia National Laboratories. 1987.

Mack, M.G., T. Brandshaug, and B.H. Brady. NUREG/CR–5390, "Rock Mass Modification Around a Nuclear Waste Repository in Nevada." Washington, DC: NRC. 1989.

Mongano, G.S., W.L. Singleton, T.C. Moyer, S.C. Beason, G.L.W. Eatman, A.L. Albin, and R.C. Lung. "Geology of the ECRB Cross Drift—Exploratory Studies Facility, Yucca Mountain Project, Yucca Mountain, Nevada." SPG42GM3. Denver, Colorado: U.S. Geological Survey. 1999.

Nieder-Westermann, G.H. "Fracture Geometry Analysis for the Stratigraphic Units of the Repository Host Horizon." ANL–EBS–GE–000006. Rev. 00. Las Vegas, Nevada: CRWMS M&O. 2000.

NRC. NUREG–1762, "Integrated Issue Resolution Status Report." Washington, DC: NRC. 2002.

Ofoegbu, G.I. "Hydrological Implications of Thermally Induced Geomechanical Response at Yucca Mountain, Nevada." Rock Mechanics in the National Interest, Proceedings of the 38th U.S. Symposium on Rock Mechanics. Vol. 1. D. Elsworth, J.P. Tinucci, and K.A. Heasley, eds. Rotterdam, The Netherlands: A.A. Balkema. pp. 613–619. 2001.

———. "Thermal-Mechanical Effects on Long-Term Hydrological Properties at the Proposed Yucca Mountain Nuclear Waste Repository." CNWRA 2000-03. San Antonio, Texas: CNWRA. 2000.

———. "Variations in Drift Stability at the Proposed Yucca Mountain Repository." Rock Mechanics for Industry, Proceedings of the 37th U.S. Symposium on Rock Mechanics. Vol. 2. B. Amadei, R.L. Kranz, G.A. Scott, and P.H. Smeallie, eds. Rotterdam, The Netherlands: A.A. Balkema. pp. 767–773. 1999.

Ofoegbu, G.I., S. Painter, R. Chen, R.W. Fedors, and D.A. Ferrill. "Geomechanical and Thermal Effects on Moisture Flow at the Proposed Yucca Mountain Nuclear Waste Repository." *Nuclear Technology*. Vol. 134. pp. 241–262. 2001.

Pan, E., B. Amadei, and W.Z. Savage. "Gravitational and Tectonic Stresses in Anisotropic Rock with Irregular Topography." *International Journal of Rock Mechanics and Mining Sciences, Geomechanics Abstracts*. Vol. 32. pp. 201–214. 1995.

Peters, R.R. Thermal Response to Emplacement of Nuclear Waste in Long, Horizontal Boreholes." SAND82–2497. Albuquerque, New Mexico: Sandia National Laboratories. 1983.

Ranalli, G. *Rheology of the Earth: Deformation and Flow Processes in Geophysics and Geodynamics*. Boston, Massachusetts: Allen and Unwin, Inc. p. 366. 1987.

Snow, D.T. "Rock Fracture Spacings, Openings, and Porosities." Proceedings of the American Society of Civil Engineers. *Journal of the Soil Mechanics and Foundations Division*. Vol. 94 (SM1). pp. 73–91. 1968.

Stock, J.M. and J.H. Healy. "Stress Field at Yucca Mountain, Nevada." *Geologic and Hydrologic Investigations of a Potential Nuclear Waste Disposal Site at Yucca Mountain, Southern Nevada.* M.D. Carr and C.J. Yount, eds. U.S. Geological Survey Bulletin. Vol. 1790. pp. 87–93. 1988.

Sweetkind, D.S. and S.C. Williams-Stroud. "Characteristics of Fractures at Yucca Mountain, Nevada." Milestone Report 3GGF205M. Denver, Colorado: U.S. Geological Survey. 1996.

Swolfs, H.S. and W.Z. Savage. "Topographic Modification of *In-Situ* Stress in Extensional and Compressional Tectonic Environments." Proceedings of the International Symposium on Rock Stress and Rock Stress Measurement. Vol. 22. pp. 291–302. 1985.

Tan, C., R. Wang, Y. Sun, W. Lei, S. Wu, M. Yang, and W. Sun. "Numerical Modeling Estimation of the 'Tectonic Stress Plan' (TSP) Beneath Topography with Quasi-U-Shaped Valleys." *International Journal of Rock Mechanics and Mining Science.* Vol. 41. pp. 303–310. 2004.

Terzaghi, R.D. "Sources of Error in Joint Surveys." *Geotechnique.* Vol. 15. pp. 287–304. 1965.

Turcotte, D.L. and G. Schubert. *Geodynamics: Applications of Continuum Physics to Geological Problems.* New York City, New York: John Wiley and Sons, Inc. 1982.

Twiss, R.J. and E.M. Moores. *Structural Geology.* New York City, New York: W.H. Freeman and Company. 1992.

U.S. National Committee for Rock Mechanics. *Rock Fractures and Fluid Flow: Contemporary Understanding and Applications.* Washington, DC: National Academy Press. 1996.

10 SOURCE DATA, LISTED BY TRACKING NUMBER

GS971108314224.020. Revision 1 of Detailed Line Survey Data, Station 0+60 to Station 4+00, North Ramp Starter Tunnel, Exploratory Studies Facility. Submittal date: 12/03/1997.

GS971108314224.021. Revision 1 of Detailed Line Survey Data, Station 4+00 to Station 8+00, North Ramp, Exploratory Studies Facility. Submittal date: 12/03/1997.

GS971108314224.022. Revision 1 of Detailed Line Survey Data, Station 8+00 to Station 10+00, North Ramp, Exploratory Studies Facility. Submittal date: 12/03/1997.

GS971108314224.023. Revision 1 of Detailed Line Survey Data, Station 10+00 to Station 18+00, North Ramp, Exploratory Studies Facility. Submittal date: 12/03/1997.

GS971108314224.024. Revision 1 of Detailed Line Survey Data, Station 18+00 to Station 26+00, North Ramp, Exploratory Studies Facility. Submittal date: 12/03/1997.

GS971108314224.025. Revision 1 of Detailed Line Survey Data, Station 26+00 to Station 30+00, North Ramp and Main Drift, Exploratory Studies Facility. Submittal date: 12/03/1997.

GS960708314224.008. Provisional Results: Geotechnical Data for Station 30+00 to Station 35+00, Main Drift of the ESF. Submittal date: 08/05/1996. *Data have been submitted to the Technical Data Management System and are currently being processed.*

GS000608314224.004. Provisional Results: Geotechnical Data for Station 35+00 to 40+00, Main Drift of the ESF. 06/20/2000.

GS960708314224.010. Provisional Results: Geotechnical Data for Station 40+00 to Station 45+00, Main Drift of the ESF. Submittal date: 08/05/1996.

GS971108314224.026. Revision 1 of Detailed Line Survey Data, Station 45+00 to Station 50+00, Main Drift, Exploratory Studies Facility. Submittal date: 12/03/1997.

GS960908314224.014. Provisional Results: ESF Main Drift, Station 50+00 to 55+00. Submittal date: 09/09/1996.

GS971108314224.028. Revision 1 of Detailed Line Survey Data, Station 55+00.18 to Station 60+00. Submittal date: 12/03/1997.

GS970208314224.003. Geotechnical Data for Station 60+00 to Station 65+00, South Ramp of the ESF. Submittal date: 12/12/1997.

GS970808314224.008. Provisional Results: Geotechnical Data for Station 65+00 to Station 70+00, South Ramp of the ESF. Submittal date: 08/18/1997.

GS970808314224.010. Provisional Results: Geotechnical Data for Station 70+00 to Station 75+00, South Ramp of the ESF. Submittal date: 08/25/1997.

GS970808314224.012. Provisional Results: Geotechnical Data for Station 75+00 to Station 78+77, South Ramp of the ESF. Submittal date: Submittal date: 08/25/1997.

GS990408314224.001. Detailed Line Survey Data for Stations 00+00.89 to 14+95.18, ECRB Cross Drift. Submittal Date: 09/09/1999.

GS990408314224.002. Detailed Line Survey Data for Stations 15+00.85 to 26+63.8, ECRB Cross Drift. Submittal Date: 09/09/1999.

APPENDIX

ADDITIONAL STRESS-STATE RESULTS

This appendix contains the results of 10 additional analyses of stress-state evolution.

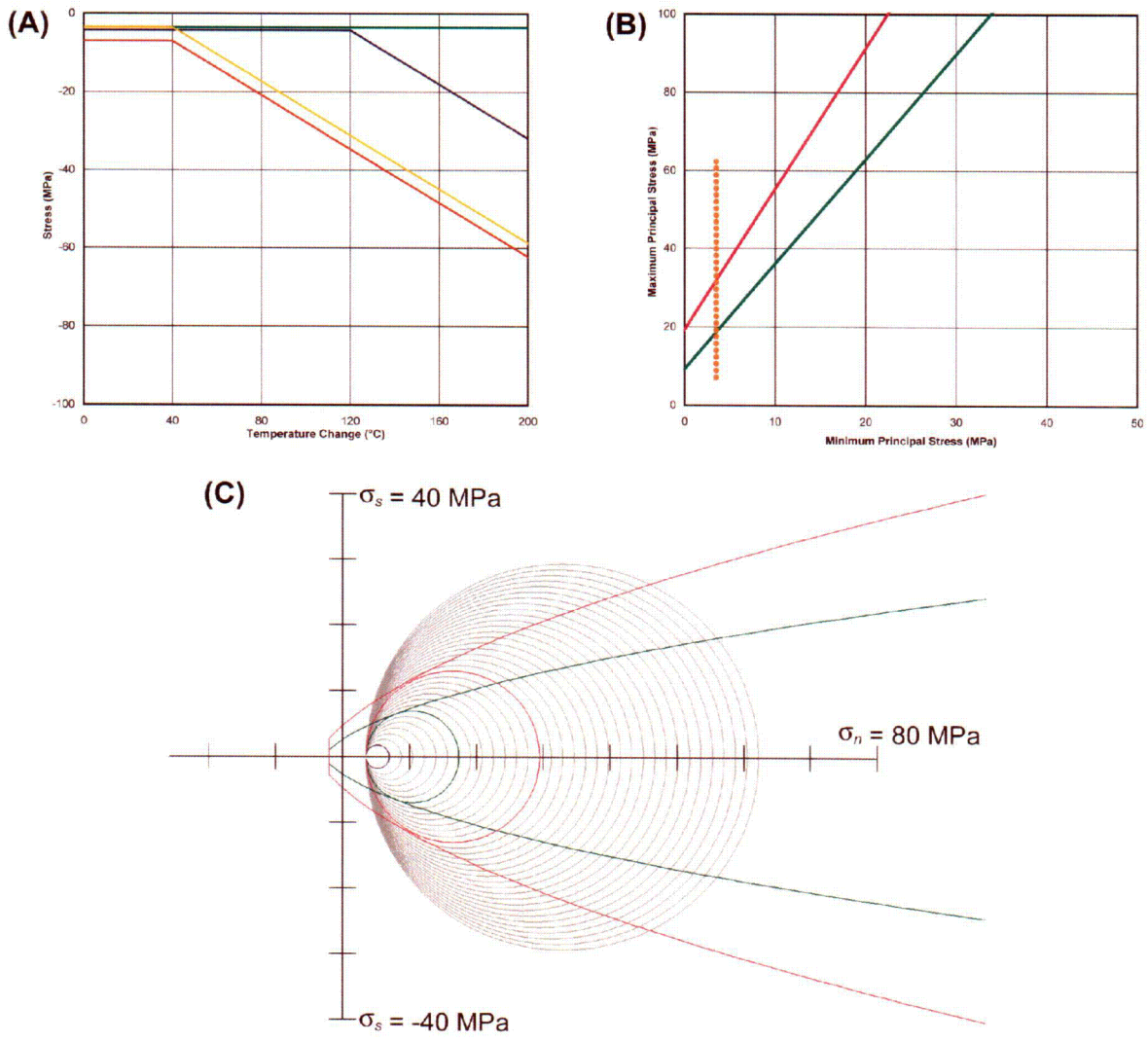

Figure 1. Summary of results for Tptpmn interval using Mongano, et al. (1999) set selection criteria and Bandis, et al. (1983) aperture reduction method. (A) Temperature versus stress-state plot showing stress magnitude (red = σ_v, blue = horizontal 030° and green = horizontal 120°) plus maximum differential stress (yellow = $\sigma_1 - \sigma_3$). (B) Stress-state evolution (orange points) plotted in principal stress space (σ_1 versus σ_3) showing Coulomb failure envelopes for good rock (RMQ5 = pink) and poor rock (RMQ1 = green). (C) Stress-state evolution in Mohr space (σ_n versus σ_s) with superimposed Hoek-Brown failure envelopes (RMQ5 = pink and RMQ1 = green) showing *in-situ* stress state (blue) and stress states at failure. See main document text for further discussion.

C15

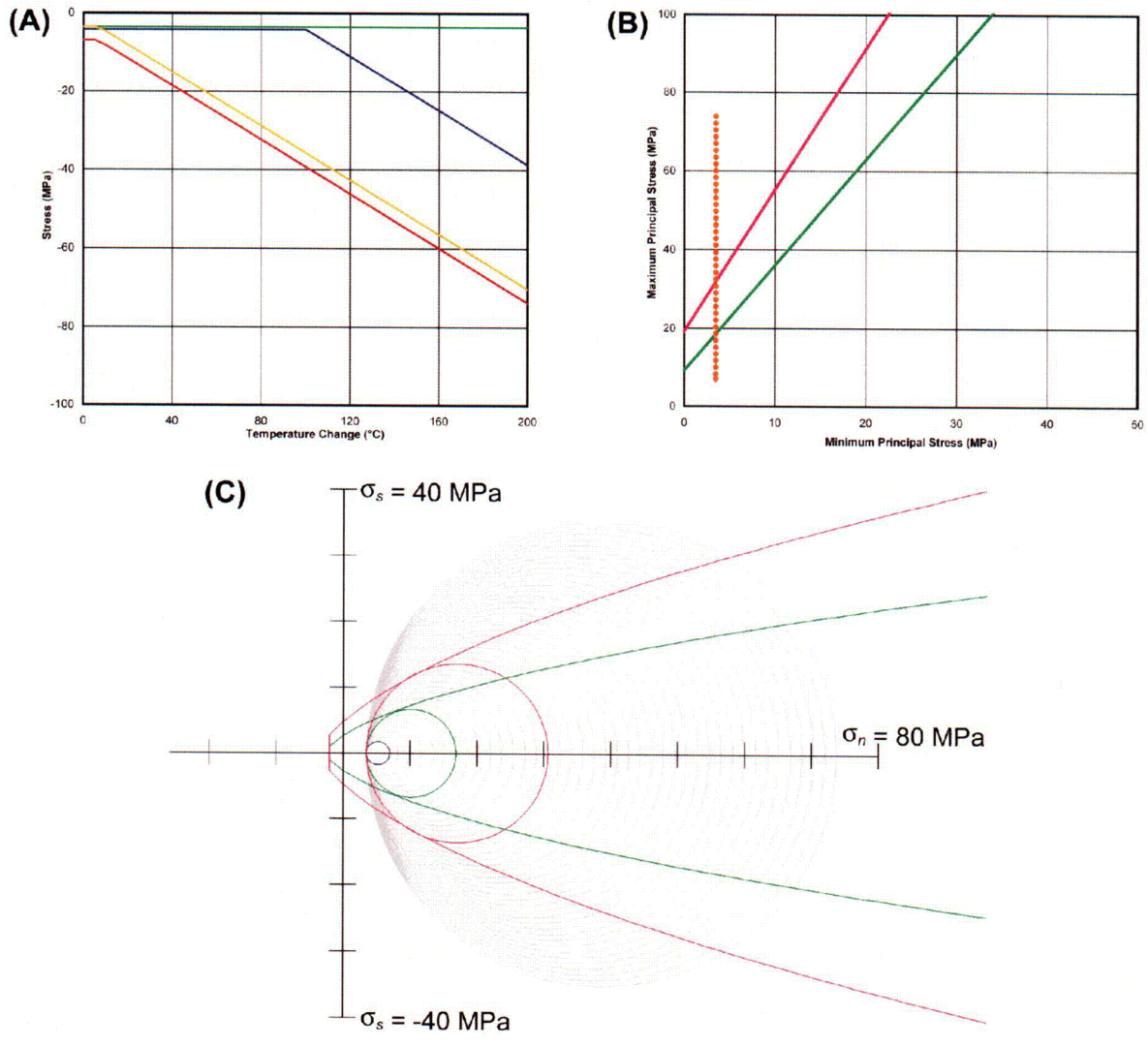

Figure 2. Summary of results for Tptpmn interval using Mongano, et al. (1999) set selection criteria and Barton, et al. (1985) aperture reduction method. (A) Temperature versus stress-state plot showing stress magnitude (red = σ_v, blue = horizontal 030° and green = horizontal 120°) plus maximum differential stress (yellow = $\sigma_1 - \sigma_3$). (B) Stress-state evolution (orange points) plotted in principal stress space (σ_1 versus σ_3) showing Coulomb failure envelopes for good rock (RMQ5 = pink) and poor rock (RMQ1 = green). (C) Stress-state evolution in Mohr space (σ_n versus σ_s) with superimposed Hoek-Brown failure envelopes (RMQ5 = pink and RMQ1 = green) showing *in-situ* stress state (blue) and stress states at failure. See main document text for further discussion.

C16

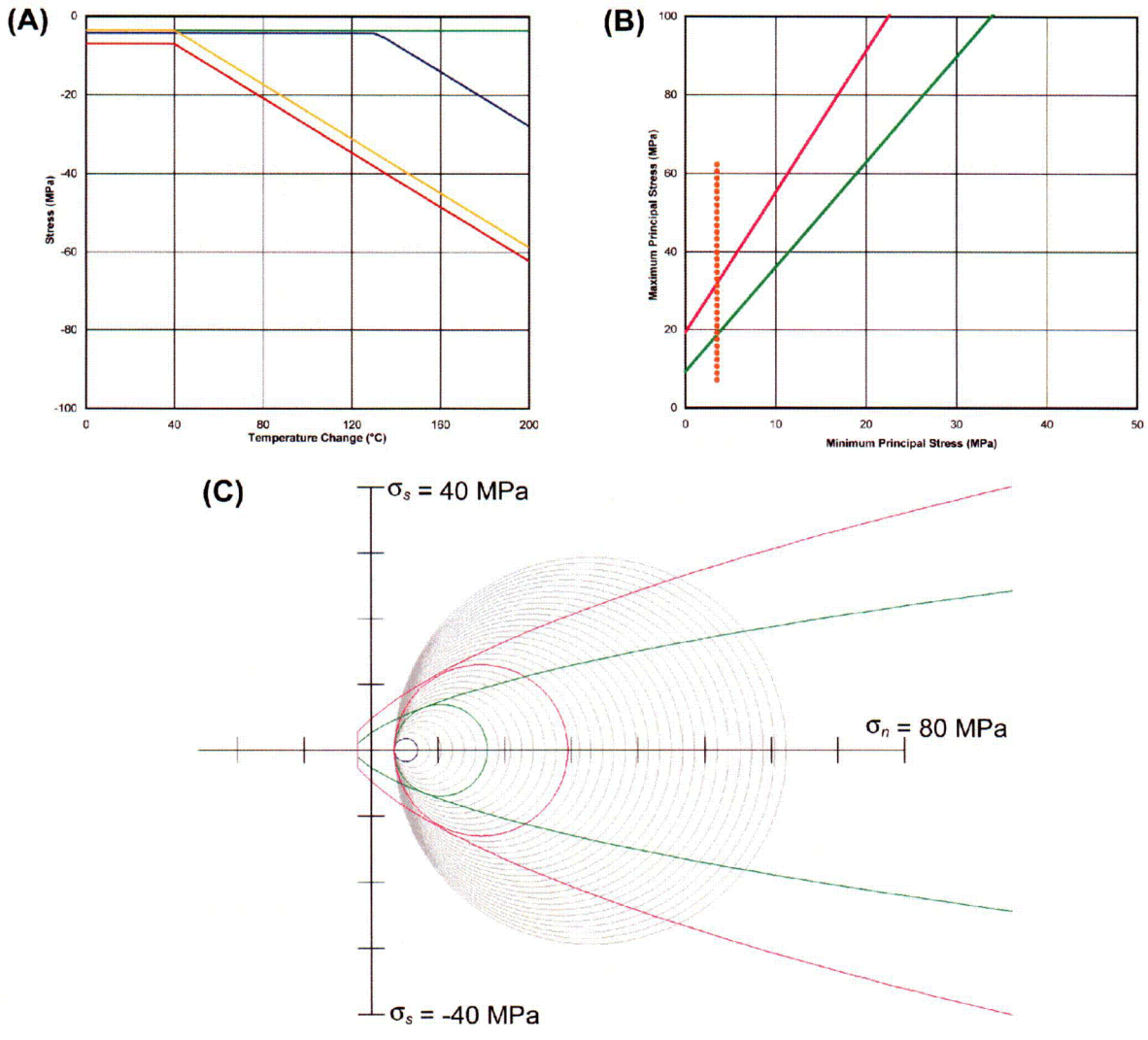

Figure 3. Summary of results for Tptpmn interval using Nieder-Westermann (2000) set selection criteria and Bandis, et al. (1983) aperture reduction method. (A) Temperature versus stress-state plot showing stress magnitude (red = σ_v, blue = horizontal 030° and green = horizontal 120°) plus maximum differential stress (yellow = $\sigma_1 - \sigma_3$). (B) Stress-state evolution (orange points) plotted in principal stress space (σ_1 versus σ_3) showing Coulomb failure envelopes for good rock (RMQ5 = pink) and poor rock (RMQ1 = green). (C) Stress-state evolution in Mohr space (σ_n versus σ_s) with superimposed Hoek-Brown failure envelopes (RMQ5 = pink and RMQ1 = green) showing *in-situ* stress state (blue) and stress states at failure. See main document text for further discussion.

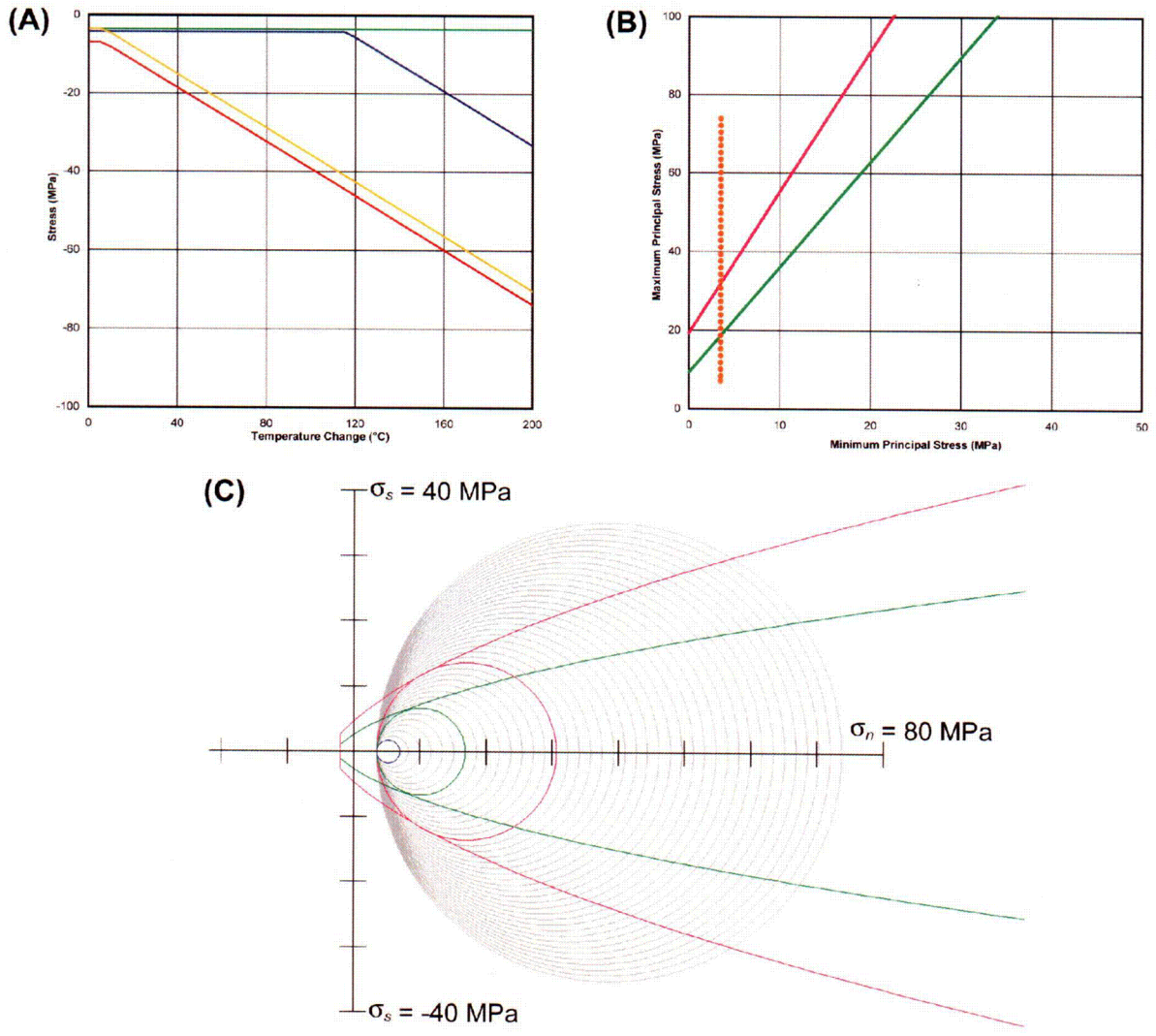

Figure 4. Summary of results for Tptpmn interval using Nieder-Westermann (2000) set selection criteria and Barton, et al. (1985) aperture reduction method. (A) Temperature versus stress-state plot showing stress magnitude (red = σ_v, blue = horizontal 030° and green = horizontal 120°) plus maximum differential stress (yellow = $\sigma_1 - \sigma_3$). (B) Stress-state evolution (orange points) plotted in principal stress space (σ_1 versus σ_3) showing Coulomb failure envelopes for good rock (RMQ5 = pink) and poor rock (RMQ1 = green). (C) Stress-state evolution in Mohr space (σ_n versus σ_s) with superimposed Hoek-Brown failure envelopes (RMQ5 = pink and RMQ1 = green) showing *in-situ* stress state (blue) and stress states at failure. See main document text for further discussion.

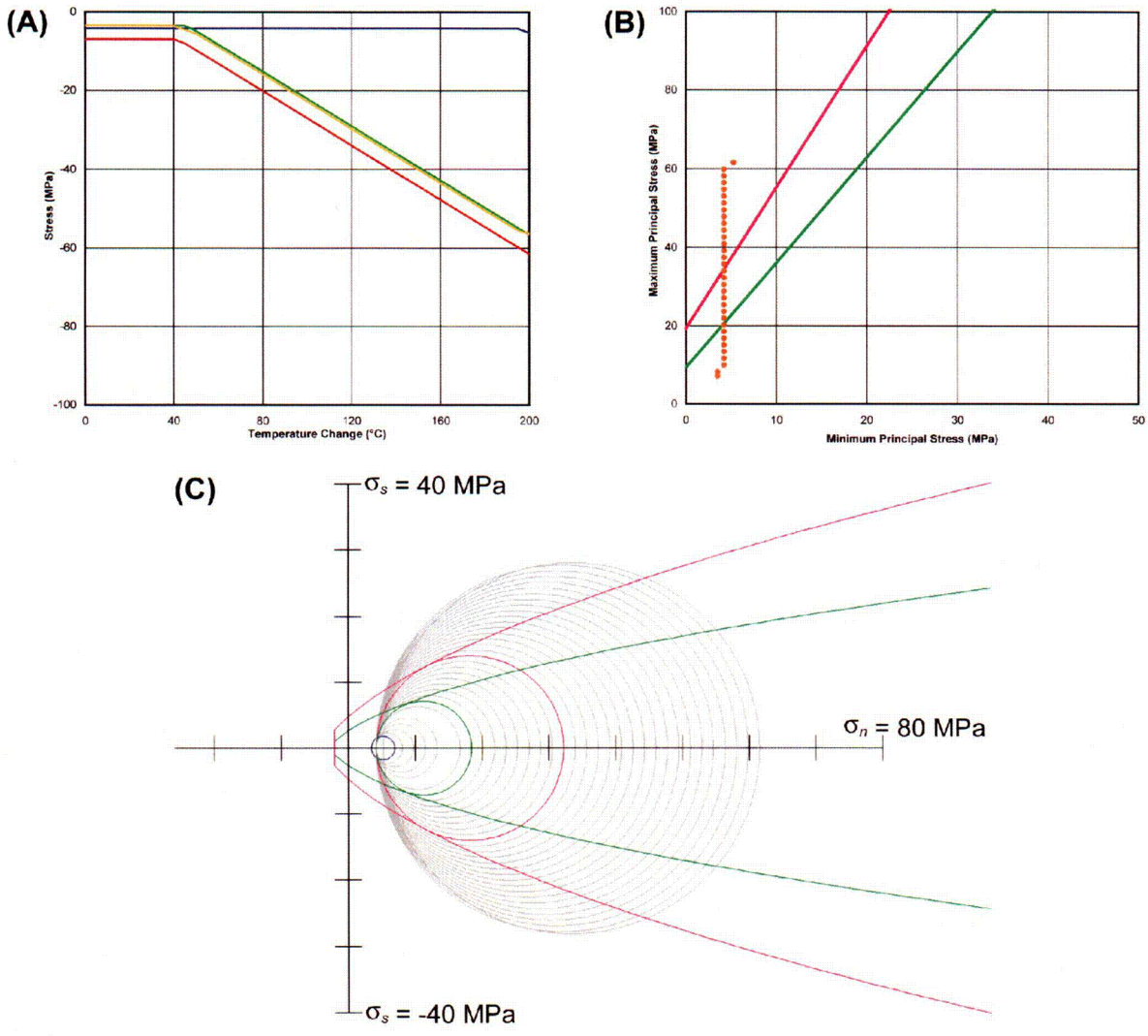

Figure 5. Summary of results for Tptpll interval using Mongano, et al. (1999) set selection criteria and Bandis, et al. (1983) aperture reduction method. (A) Temperature versus stress-state plot showing stress magnitude (red = σ_v, blue = horizontal 030° and green = horizontal 120°) plus maximum differential stress (yellow = $\sigma_1 - \sigma_3$). (B) Stress-state evolution (orange points) plotted in principal stress space (σ_1 versus σ_3) showing Coulomb failure envelopes for good rock (RMQ5 = pink) and poor rock (RMQ1 = green). (C) Stress-state evolution in Mohr space (σ_n versus σ_s) with superimposed Hoek-Brown failure envelopes (RMQ5 = pink and RMQ1 = green) showing *in-situ* stress state (blue) and stress states at failure. See main document text for further discussion.

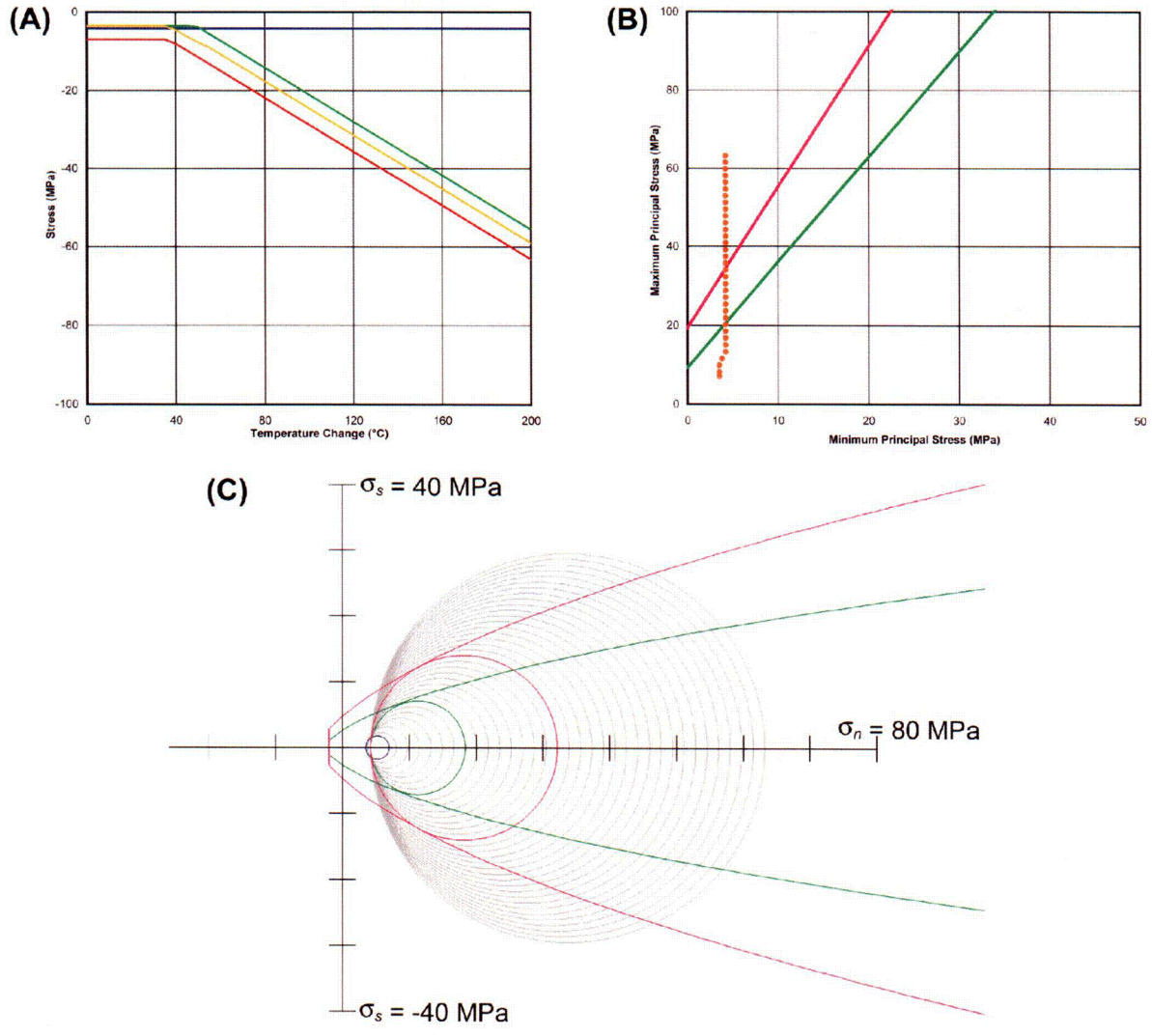

Figure 6. Summary of results for Tptpll interval using Mongano, et al. (1999) set selection criteria and Barton, et al. (1985) aperture reduction method. (A) Temperature versus stress-state plot showing stress magnitude (red = σ_v, blue = horizontal 030° and green = horizontal 120°) plus maximum differential stress (yellow = $\sigma_1 - \sigma_3$). (B) Stress-state evolution (orange points) plotted in principal stress space (σ_1 versus σ_3) showing Coulomb failure envelopes for good rock (RMQ5 = pink) and poor rock (RMQ1 = green). (C) Stress-state evolution in Mohr space (σ_n versus σ_s) with superimposed Hoek-Brown failure envelopes (RMQ5 = pink and RMQ1 = green) showing *in-situ* stress state (blue) and stress states at failure. See main document text for further discussion.

CZO

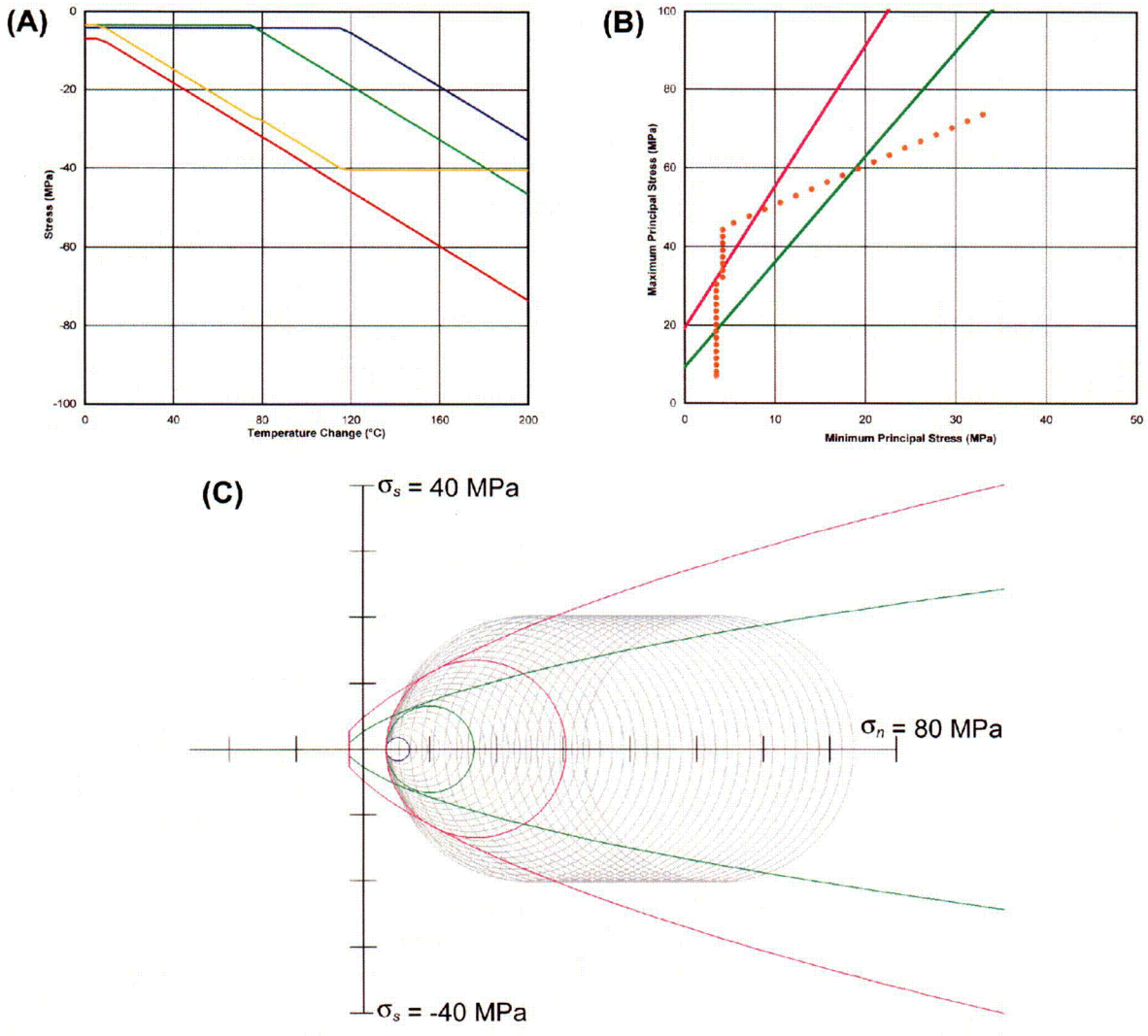

Figure 7. Summary of results for Tptpll interval using Nieder-Westermann (2000) set selection criteria and maximum aperture reduction method. (A) Temperature versus stress-state plot showing stress magnitude (red = σ_v, blue = horizontal 030° and green = horizontal 120°) plus maximum differential stress (yellow = $\sigma_1 - \sigma_3$). (B) Stress-state evolution (orange points) plotted in principal stress space (σ_1 versus σ_3) showing Coulomb failure envelopes for good rock (RMQ5 = pink) and poor rock (RMQ1 = green). (C) Stress-state evolution in Mohr space (σ_n versus σ_s) with superimposed Hoek-Brown failure envelopes (RMQ5 = pink and RMQ1 = green) showing *in-situ* stress state (blue) and stress states at failure. See main document text for further discussion.

CZ1

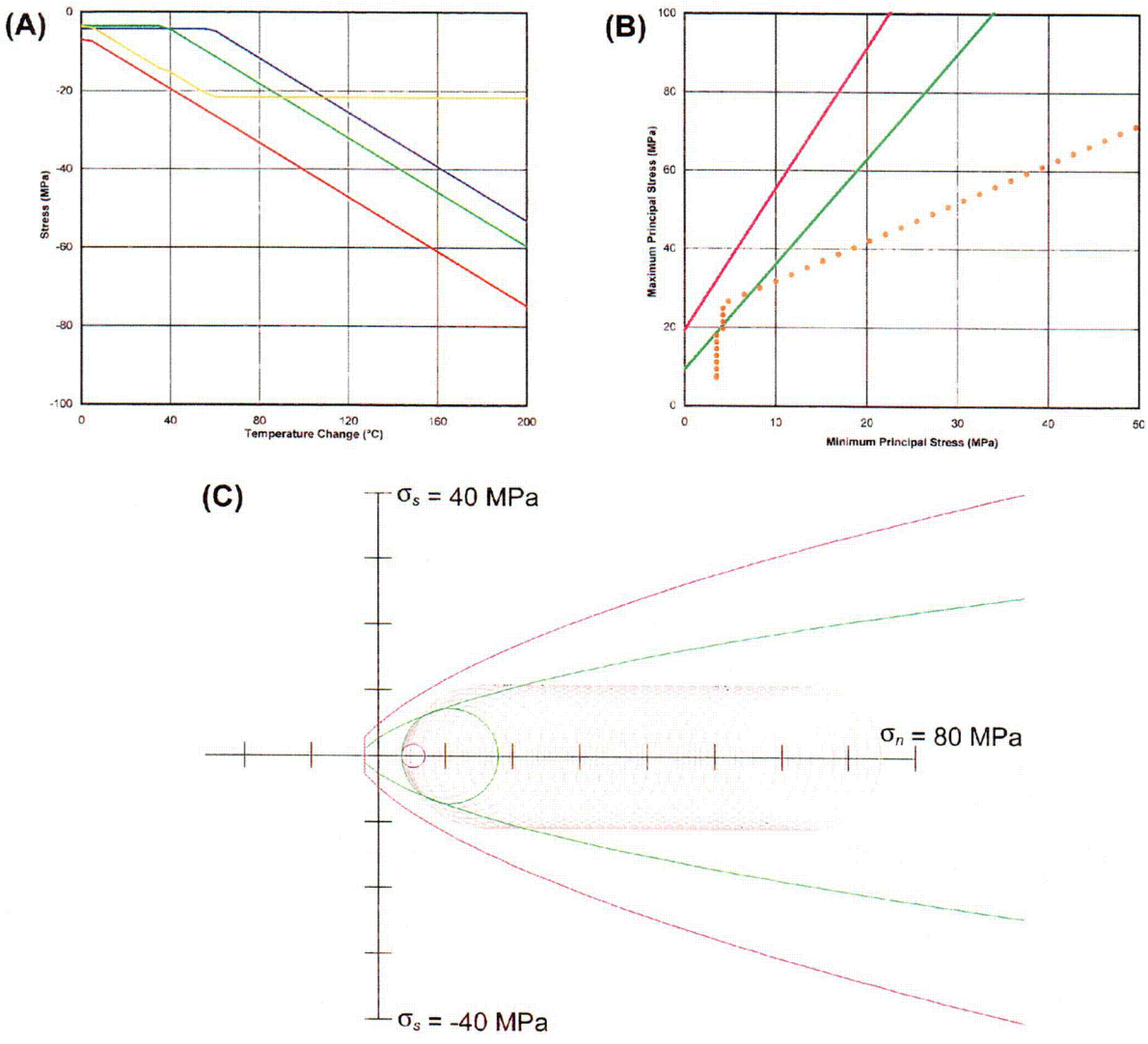

Figure 8. Summary of results for Tptpll interval using Nieder-Westermann (2000) set selection criteria and 50 percent aperture reduction method. (A) Temperature versus stress-state plot showing stress magnitude (red = σ_v, blue = horizontal 030° and green = horizontal 120°) plus maximum differential stress (yellow = $\sigma_1 - \sigma_3$). (B) Stress-state evolution (orange points) plotted in principal stress space (σ_1 versus σ_3) showing Coulomb failure envelopes for good rock (RMQ5 = pink) and poor rock (RMQ1 = green). (C) Stress-state evolution in Mohr space (σ_n versus σ_s) with superimposed Hoek-Brown failure envelopes (RMQ5 = pink and RMQ1 = green) showing *in-situ* stress state (blue) and stress states at failure. See main document text for further discussion.

C22

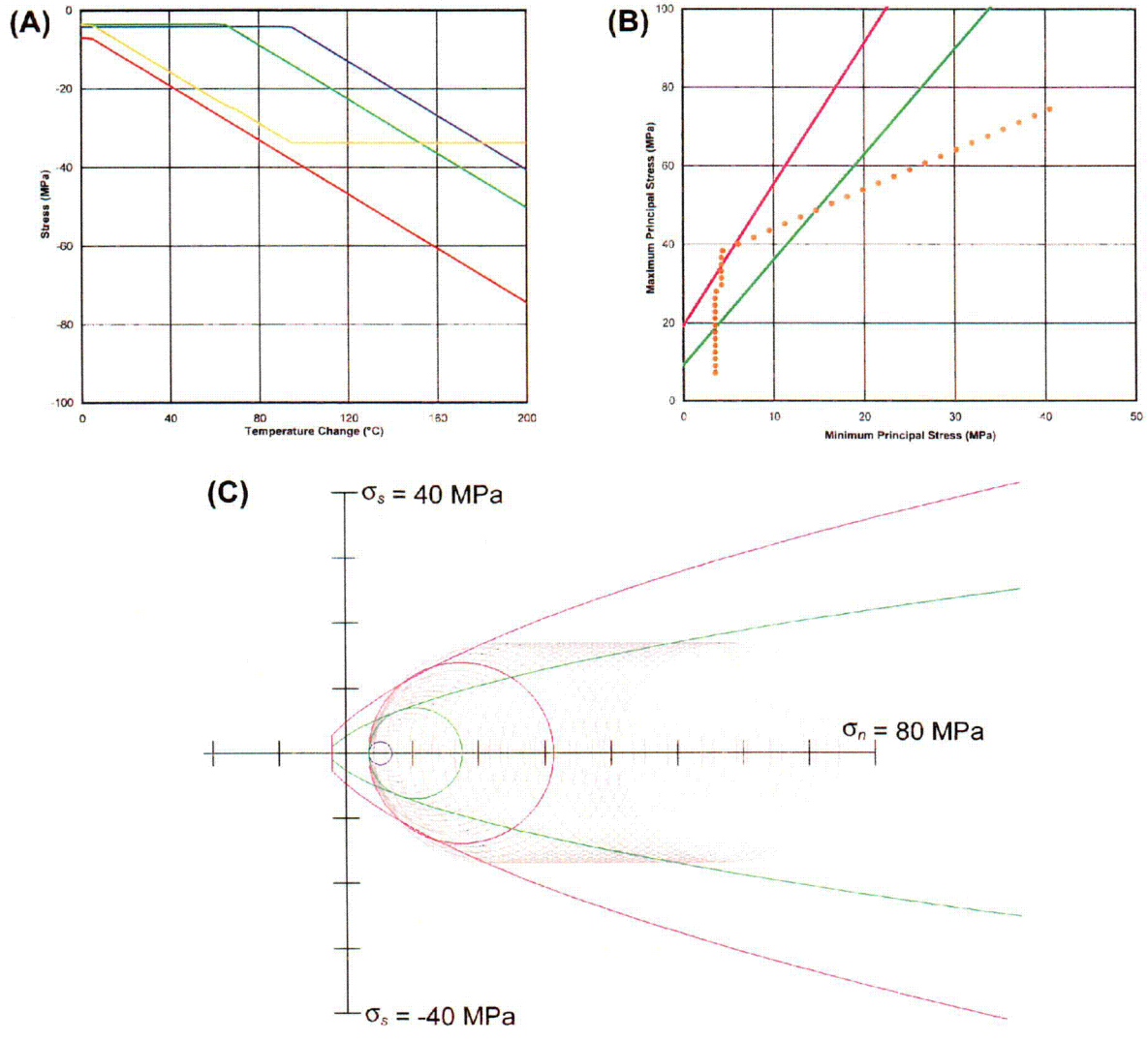

Figure 9. Summary of results for Tptpll interval using Nieder-Westermann (2000) set selection criteria and Bandis, et al. (1983) aperture reduction method. (A) Temperature versus stress-state plot showing stress magnitude (red = σ_v, blue = horizontal 030° and green = horizontal 120°) plus maximum differential stress (yellow = $\sigma_1 - \sigma_3$). (B) Stress-state evolution (orange points) plotted in principal stress space (σ_1 versus σ_3) showing Coulomb failure envelopes for good rock (RMQ5 = pink) and poor rock (RMQ1 = green). (C) Stress-state evolution in Mohr space (σ_n versus σ_s) with superimposed Hoek-Brown failure envelopes (RMQ5 = pink and RMQ1 = green) showing *in-situ* stress state (blue) and stress states at failure. See main document text for further discussion.

C23

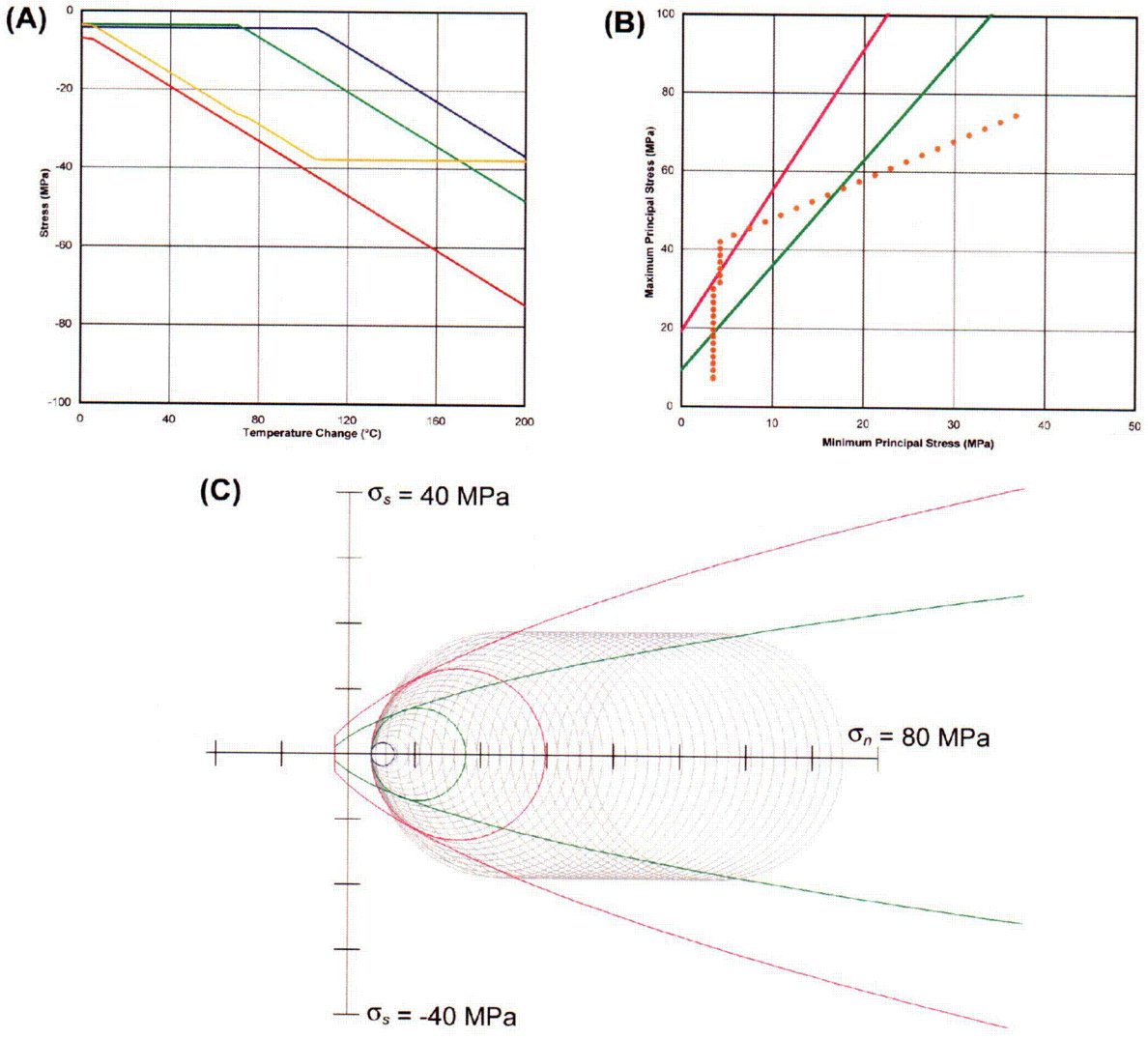

Figure 10. Summary of results for Tptpll interval using Nieder-Westermann (2000) set selection criteria and Barton, et al. (1985) aperture reduction method. (A) Temperature versus stress-state plot showing stress magnitude (red = σ_v, blue = horizontal 030° and green = horizontal 120°) plus maximum differential stress (yellow = $\sigma_1 - \sigma_3$). (B) Stress-state evolution (orange points) plotted in principal stress space (σ_1 versus σ_3) showing Coulomb failure envelopes for good rock (RMQ5 = pink) and poor rock (RMQ1 = green). (C) Stress-state evolution in Mohr space (σ_n versus σ_s) with superimposed Hoek-Brown failure envelopes (RMQ5 = pink and RMQ1 = green) showing *in-situ* stress state (blue) and stress states at failure. See main document text for further discussion.

C24

REFERENCES

Bandis, S.C., A.C. Lumsden, and N.R. Barton. "Fundamentals of Rock Joint Deformation." *International Journal of Rock Mechanics and Mining Science.* Vol. 20, No. 6. pp. 249–268. 1983.

Barton, N., S. Bandis, and K. Bakhtar. "Strength, Deformation, and Conductivity Coupling of Rock Joints." *International Journal of Rock Mechanics and Mining Science.* Vol. 22, No. 3. pp. 121–140. 1985.

Mongano, G.S., W.L. Singleton, T.C. Moyer, S.C. Beason, G.L.W. Eatman, A.L. Albin, and R.C. Lung. "Geology of the ECRB Cross Drift—Exploratory Studies Facility, Yucca Mountain Project, Yucca Mountain, Nevada." SPG42GM3. Denver, Colorado: U.S. Geological Survey. 1999.

Nieder-Westermann, G.H. "Fracture Geometry Analysis for the Stratigraphic Units of the Repository Host Horizon." ANL–EBS–GE–000006. Rev 00. Las Vegas, Nevada: CRWMS M&O. 2000.